Predictive model of impact-induced bonding in cold spray using the Material Point Method

by

Jiaju Tang

A thesis
presented to the University of Waterloo
in fulfillment of
the thesis requirement for the degree of
Master of Applied Science
in
Mechanical and Mechatronics Engineering

Waterloo, Ontario, Canada 2021

Examining Committee Membership

The following served on the Examining Committee for this thesis. The decision of the Examining Committee is by majority vote.

Supervisor(s):
Hamid Jahedmotlagh, Professor,
Department of Mechanical and Mechatronics Engineering,
University of Waterloo

Mohammadreza Hirmand, Adjunct Professor,
Department of Mechanical and Mechatronics Engineering,
University of Waterloo

Internal Member:
Kaan Inal, Associate Professor,
Department of Mechanical and Mechatronics Engineering,
University of Waterloo

Internal Member:
Jean-Pierre Hickey, Assistant Professor,
Department of Mechanical and Mechatronics Engineering,
University of Waterloo

Author's Declaration

I hereby declare that I am the sole author of this thesis. This is a true copy of the thesis, including any required final revisions, as accepted by my examiners.

I understand that my thesis may be made electronically available to the public.

Abstract

Cold spray technology has emerged in recent years as a promising method of powder deposition that is inherently different from other processes. Without melting of the particles prior to deposition, powders of a wide range of materials can be deposited onto a substrate primarily through their initial kinetic energy. By keeping particle temperatures below melting, coatings made from cold spray are able to elegantly avoid many temperature-related defects commonly seen in traditional coating methods. The amount of kinetic energy required for successful bonding has been experimentally shown to be defined by a critical velocity, which varies depending on the thermomechanical properties of the powder material. Due to the time duration across which bonding occurs, it is difficult to observe the precise bonding phenomena in experiments leading to an emphasis on numerical simulation. However, most numerical studies have been focused on using mesh-based FEMs and identify bonding during post-processing of results. As such, these models are incapable of properly predicting bonding or bond effects on material behavior.

In the current thesis, a bonding model is developed within a Material Point Method (MPM) framework that is able to directly model bonding effects on each body within the simulation. By using the MPM, it is possible to combine the advantages of Lagrangian and Eulerian FEMs while simultaneously minimizing their shortcomings in modeling the extreme strain and strain rate conditions seen in cold spray. This novel, direct bonding model introduces a time-discrete bond parameter whose evolution is based on adhesion energy, similar to the energy release rate seen in damage/fracture modeling. The overall code has been generalized to also provide initial consideration of multiparticle impacts, which is important for modeling the overall build-up and predicting the properties of coatings or structures.

With the current model, it is possible to produce accurate predictions of the critical velocity for a range of Al particle sizes. Through use of adhesion energy and regularization techniques, the bonding model is able perform independently of discretization level and accurately capture the material jetting behavior observed experimentally to be related to impact-induced bonding. A linear trend is predicted such that critical velocity decreases as particle diameter increases. Furthermore, the current model also predicts convergence of the percent bonded area with grid size refinement towards a value which aligns with theoretical works. This further suggests that the current model is also able to provide insight on the bond quality and mechanical properties of the final coating/component with sufficient discretization.

Acknowledgements

I would like to thank my supervisor Professor Hamid Jahed for his instruction and unwavering support during my time as his student. Furthermore, I would also like to pass my profound gratitude to my co-supervisor, Dr. Mohammadreza Hirmand, for his vast knowledge and insightful guidance throughout this entire experience. The present work would not have been possible without their tremendous support.

My sincere thanks also go to the committee members for their time and expertise in reviewing this thesis. Their comments and advice were invaluable for improving the final quality of my work.

Table of Contents

Examining Committee Membership ii

Author's Declaration iii

Abstract iv

Acknowledgements v

List of Figures ix

List of Tables xii

List of Abbreviations xiii

Chapter 1 Introduction 1

- 1.1 Thermal Spray Technology 1
- 1.2 Cold Spray Technology 2
- 1.3 Motivation, Objectives and Methodology 3
- 1.4 Thesis Outline 4

Chapter 2 Literature Survey 5

- 2.1 Cold Spray Applications 5
- 2.2 Cold Spray Bonding Theory 6
- 2.3 Modeling Techniques 9
  - 2.3.1 Lagrangian Methods 9
  - 2.3.2 Eulerian and Other Mesh-based Methods 10
  - 2.3.3 Particle-based Methods 12
- 2.4 Constitutive Models 13
  - 2.4.1 Johnson-Cook Strength Model 13
  - 2.4.2 Preston-Tonks-Wallace Strength Model 14
- 2.5 Bonding Models 16
  - 2.5.1 Cohesive Zone and Adhesion Models 16
  - 2.5.2 Adhesion Energy Definition and Bond Strength Prediction 17

Chapter 3 Material Point Method Formulation 19

- 3.1 Governing Equations 19
  - 3.1.1 Conservation of Mass 20
  - 3.1.2 Conservation of Momentum 20
  - 3.1.3 Conservation of Energy 21
- 3.2 Weak Formulation 22

3.3 MPM Description 23
3.4 Numerical Implementation 25
3.5 Numerical Considerations 31
  3.5.1 Strength Model 31
  3.5.2 Equation of State 32
  3.5.3 Adiabatic Heating 33
  3.5.4 Normal Vector Calculation 34
  3.5.5 Infinite/Semi-infinite Media 35
Chapter 4 Direct Bonding Model 37
4.1 Strain-based Bonding Model 37
  4.1.1 Model Formulation 37
  4.1.2 Calibration Tests and Results 40
  4.1.3 Discretization Sensitivity Issue 44
  4.1.4 Bond Initiation Site Issue 46
4.2 Convergence Test 47
  4.2.1 Convergence Test Motivation 47
  4.2.2 Convergence Test Set-up 47
  4.2.3 Convergence Test Results 48
  4.2.4 Strain Energy Density Convergence 49
4.3 Energy-based Bonding Model 50
  4.3.1 Motivation for Development 50
  4.3.2 Energy-Based Bonding Model Formulation 50
  4.3.3 Calibration Test Setup 52
Chapter 5 Final Model Results and Discussion 54
5.1 Simulation Results and Discussion 54
  5.1.1 Model Calibration Results from Logistic Regression 54
  5.1.2 Percent Bonded Contact Particle Classification Tolerance 58
  5.1.3 Discretization Sensitivity 64
  5.1.4 Time Step Scaling Factor 66
5.2 Calibrated Model Performance 67
  5.2.1 Predicted Material Behavior under Subcritical and Critical Velocity Impacts 67
  5.2.2 Critical Velocity Prediction 69

5.2.2 Two-Particle Impacts 73
5.2.3 Large-scale Particle Impacts 76
5.3 Comparison with Experimental and Other Numerical Results 78
5.3.1 Bond Initiation Site Analysis 78
5.3.2 Percent Bonded Area 79
Chapter 6 Conclusions and Future Work 81
6.1 Conclusions 81
6.2 Future Work 82
References 84

Appendix

Appendix A – Stress Update 92
Appendix B – Bonding Boundaries with All Grid Configurations 95

List of Figures

Figure 1.1 Schematic of a typical TS process [3]. 1

Figure 1.2 Schematic representation of the cold spray process [7]. 2

Figure 2.1: Schematic representation comparison of the stress-strain curves in normal strain-hardening (Isothermal) material, adiabatically softened material (Adiabatic) and in a material undergoing adiabatic shear localization (Localization) [8]. 7

Figure 2.2: Schematic representation of jetting in cold spray: Stage I. Impact induces a shock wave. Stage II. Shock detaches form the leading edge. Stage III. Jet forms on the basis of pressure releases. Note: the uniformity of the colors is not meant to suggest uniform pressure [16]. 7

Figure 2.3: Single particle impacts of Al on Al (a, b) and Au on Au (c, d) at velocities below (a, c) and above (b, d) their respective critical velocities. White arrows indicate the presence of material jetting, which is essentially in achieving adhesion [12]. 8

Figure 2.4: Lips around the perimeter of the contact interface which show the lips associated with material jetting in Au on Au impacts [12]. 8

Figure 2.5: 8-node hexahedron element with nodal parent coordinates [29]. 9

Figure 2.6: Contours of the (a) equivalent plastic strain and (b) temperature for Al/Al impact obtained using the Lagrangian method at 19 ns post-impact [30]. 10

Figure 2.7: Contour of equivalent plastic strain for Cu particle impacting a Cu substrate at 500 m/s [17]. 11

Figure 2.8: Contours of the (a) equivalent plastic strain and (b) temperature for Al/Al impact obtained using an ALE mesh [30]. 12

Figure 2.9: Interpolation technique used in the SPH method [38]. 13

Figure 3.1: 2D schematic representation of the initial system used to model a single-particle CS impact. Red lines indicate the computational grids while black dotes indicate material points. 19

Figure 3.2: Schematic representation of the MPM algorithm showing a) mapping of particle mass and momentum to nodes, b) calculation of new nodal forces and momentums etc., c) updating of particle velocity and position with nodal values, d) storage of all material properties in particles and resetting of grid [32]. 24

Figure 3.3: Flow chart of the MUSL MPM algorithm with contact considerations compared with traditional FEMs. 26

Figure 3.4: Contact detection schematic, showing the region of influence of a contact node [32]. 28

Figure 3.5: Multi-mesh method applied only at contact nodes introduced by Ma et al. [70]. 31

Figure 3.6: Schematic showing the improved accuracy of using the normal vector of the larger volume body r, particularly around edge nodes [75]. 34

Figure 3.7: Viscous damping boundary schematic, showing primary (z) and secondary wave (x and y) directions [77]. 36

Figure 4.1: Flow chart of the MUSL MPM algorithm with contact considerations, updated with blocks in green showing how the bonding considerations are included. 40

Figure 4.2: Plots of restitution ratio at 100 ns with respect to average surface bonding parameter for 14 μm (a) and 30 μm (b) diameter Al powder particles. Solid vertical and horizontal

lines represent the classification tolerances for average $Dbond$ and restitution ratio, respectively. Labeled points indicate tests results within the transition zone. 41
Figure 4.3: Typical sigmoid function graph centered at Z = 0 [80]. 42
Figure 4.4: Logistic regression plots showing the boundaries at which bonding occurs based on the previously identified tolerance values for the 14-μm (a) and 30-μm (b) diameter powder particles. The intersection of these boundaries (c) identifies the set of model parameters that would result in bond initiation for both-sized particles impacted at critical velocities. 44
Figure 4.5: Effective plastic strain distribution in the 14-μm particle using a) 1.0/0.35 and b) 0.5/0.175 grid configurations with no bonding model considerations shows that material jetting becomes apparent as the grid is refined. 45
Figure 4.6: a) Plot of predicted bonding boundaries for the 14-um diameter particle using a grid configuration of 1.0/0.35 and 0.7/0.25. Effective plastic strains determined using the same bonding model parameters labeled in a) are also shown using grid configurations of b) 1.0/0.35 and c) 0.7/0.25. 46
Figure 4.7: Contour plot of the effective plastic strain in the 14-μm diameter Al particle at 120ns post-impact. Circled regions show that bonding initiates in near the perimeter of the contact surface within the jetting region. 46
Figure 4.8: Plots of average effective plastic strain for the powder particle based on the PTW constitutive model without friction and bond effects considered. 48
Figure 4.9: Plots of average plastic strain energy density for the powder particle calculated using the PTW constitutive model with no friction or bond effects considered. 49
Figure 5.1: Bonding boundaries and intersections achieved with the adhesion energy-based bond model with a grid configuration of a) 1.5/0.35, b) 1.0/0.25 and c) 0.7/0.175. 55
Figure 5.2: a) Plot of all intersection points using the same axis dimensions as the tested domain and b) expanded view of intersection points, labelled with the associated grid configuration with which they were identified. 55
Figure 5.3: Energy-based bonding model simulation results with a 1.0/0.25 grid configuration showing the plots of restitution ratio vs. average bonding parameter (a, b) with solid black lines showing classification tolerances. Circled in red are test results which had to be incorrectly classified to achieve similar bonding boundaries. The bonding boundary intersection identified (c) for 14 μm and 30 μm diameter Al particles are also shown. 57
Figure 5.4: Energy-based bonding model simulation results with a 1.0/0.25 grid configuration showing the plots of restitution ratio vs. average bonding parameter (a,b) with solid black lines showing logistic regression tolerances that have been adjusted to expected values. The bonding boundaries predicted (c) show a clear difference between particle sizes and a lack of intersection. 58
Figure 5.5: a) Plot of all intersection points using the same axis dimensions as the tested domain and b) expanded view of intersection points, labelled with the associated grid configuration with which they were identified. 60
Figure 5.6: Energy-based pressure independent bonding model simulation results showing the plots of restitution ratio vs. PBCP and bonding boundary intersection for 14 μm and 30 μm

diameter Al particles determined with a) 1.5/0.35, b) 1.0/0.25 and c) 0.7/0.175 grid configurations. 63
Figure 5.7: Plots of bonding boundaries of the a) 14-μm particle and b) 30-μm diameter particle identified using all grid configurations........ 64
Figure 5.8: Contour plots of effective plastic strain using an a)1.0/0.25, b)1.0/0.2 and b) 0.7/0.25 grid configuration, explicitly comparing the effects of grid size and particle spacing on material behavior. 65
Figure 5.9: Bonded boundary curves achieved using a 0.7/0.175 grid configuration and time step scaling factors of 0.1, 0.2 and 0.4. Labeled is the intersection point of the bonding boundaries for the 14 and 30 μm particles with a 0.1 scaling factor. 66
Figure 5.10: Comparison of subcritical velocity material behavior from: a) simulations of a 45-μm particle sprayed at 550 m/s and b) experimental observations of a 45-μm particle sprayed at 550 m/s [12]. Also shown are critical velocity material behavior from c) simulations of a 38-μm particle sprayed at 780 m/s and d) experimental observations of a 38-μm particle sprayed at 780 m/s [12]........ 68
Figure 5.11: Plots of PBCP vs. initial particle velocity. Vertical lines label the critical velocity approximated by a linear size-to-velocity ratio and the horizontal line identifies the average PBCP of data points within a 2% error envelope. 70
Figure 5.12: Contour plot of effective plastic strain for a) the 14-μm and b) the 22-μm diameter particles impacted at 810 m/s. 71
Figure 5.13: Plots of overall particle restitution ratio vs. initial particle velocity superimposed with PBCP vs. initial velocity plots of for all tested particle sizes. Vertical green lines show an estimate of the predicted critical velocity for each particle size using the tolerances as indicated by the dashed horizontal lines. Vertical black lines indicate the predicted critical velocities assuming a purely linear relation between particle size and experimental critical velocity. 72
Figure 5.14: Plot of PBCP vs. initial velocity with vertical lines indicating the predicted critical velocities for particle sizes ranging from 14 to 30 μm diameter. 73
Figure 5.15: Contour plot of effective plastic strain from simulating multiparticle impacts at 30 ns increments, with an offset of a) 0-μm, b) 2.5-μm, c) 5-μm and d) 7.5-μm offset between the centres of two 14-μm diameter spherical Al powder particles. 75
Figure 5.16: Effective plastic strain in impacts with ten 14-um Al particles on an Al substrate demonstrating the ability of the model to simulate particle-particle interactions and cohesion. The labeled particle can be seen to have debonded due to the ejected material points from the previously bonded particles around it. 77
Figure 5.17: Plot of particle $Dbond(\boldsymbol{xp})$ values within a 14-μm diameter Al particle impacting on Al substrate at 30 ns post-impact using the a) strain-based and b) adhesion energy-based bonding models. Model parameters were chosen such that a similar total number of bonded particles was achieved. Only particles with $Dbond(\boldsymbol{xp}) > 0.7$ are shown with particle sizes also being proportional to $Dbond(\boldsymbol{xp})$ magnitude above 1. 79

List of Tables

Table 2.1: Al material properties and PTW parameters [38]. 16

Table 3.1: Average error from maximum absolute (MA) errors in yield stress for five flow stress models under various conditions [47]. 31

Table 4.1: Grid configurations used in convergence testing. 47

Table 4.2: All tested grid configurations for each particle size grouped by grid size and listing the approximate number of initial particles per grid. 52

Table 5.1: Average bond parameter and restitution ratio tolerances (average bond parameter/restitution ratio) used to generate the bonding boundary intersections shown in the previous figure, grouped together by grid size. 56

Table 5.2: Percent bonded area and restitution ratio tolerances (PBCP/restitution ratio) used to generate the bonding boundary intersections shown in the previous figure, grouped together by grid size. 60

Table 5.3: Approximate particle and cylinder substrate dimensions used to test model performance in predicting critical impact velocity. 69

Table 5.4: Table of predicted critical velocities for particles of various sizes, along with their associated PBCP and restitution velocity values. 73

Table 5.5: Predicted overall PBCP values of two-particle impact tests to be used as an indirect measure of bond quality. The average restitution velocity filtered to only consider material points with velocities ≤ 60 m/s for each powder particle are also listed as further insight on bonding result. 76

List of Abbreviations

ABP Average Bond Parameter

ALE Arbitrary Lagrangian-Eulerian

ASI Adiabatic Shear Instability

CEL Coupled Eulerian-Lagrangian

CS Cold Spray

CoR Coefficient of Restitution

FATSLAB Fatigue and Stress Analysis Laboratory

FEA Finite Element Analysis

FEM Finite Element Method

GIMP Generalized Interpolation Material Point

HVOF High Velocity Oxy-Fuel

JC Johnson-Cook

MVG Maximum Volume Gradient

MPM Material Point Method

MUSL Modified Update Stress Last

PBCP Percent Bonded Contact Particles

PDE Partial Differential Equation

PTW Preston-Tonks-Wallace

PTWA Plasma Transferred Wire Arc

SCG Steinberg-Cochran-Guinan

SPH Smoothed Particle Hydrodynamics

TS Thermal Spray

Chapter 1 Introduction

1.1 Thermal Spray Technology

Initially developed as a method to make lead plates for batteries by Oerlikon in 1882, it was not until Schoop and his associates from Switzerland first developed the equipment and techniques for producing dense coatings with thicknesses greater than 100 μm from molten and powder metals that is became widely popular [1]. Most notably, the process proved valuable in being able to provide protection for metal surfaces as well as restore wear defects of metal parts. With the onset of the World Wars, the popularity of thermal sprays (TS) soared as a method of rapid repair for tanks and other machinery in the field [2]. Nowadays, TS technology has expanded beyond simple metals and alloys to incorporate a large variety of material types such as polymers, ceramics, ceramic-metals and other combinations of materials. Figure 1.1 shows a schematic of a typical TS technique. With this, it became possible to coat parts and machinery with a thin layer of material to improve corrosion, wear and thermal resistance as well as increase lubricity became a possibility. This allowed the propagation of TS coatings into areas such as the aerospace and automotive industries where the drive to improve fuel efficiency led manufactures to use TS to make lighter parts without compromising thermomechanical performance.

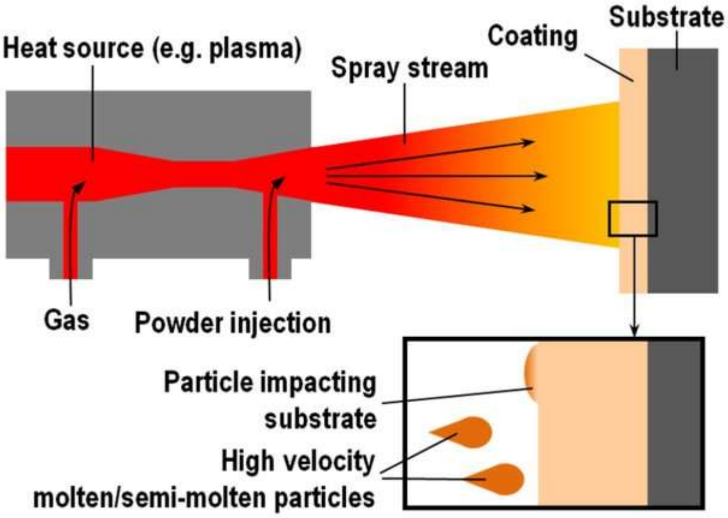

Figure 1.1 Schematic of a typical TS process [3].

Generally, the feedstock material is required to be projected through a nozzle and sprayed in a liquid or semi-liquid state. For traditional TS processes such as high-velocity oxy-fuel (HVOF), this requires high propellant temperatures which can reach values up to 3000°C [4]. Other electric-arc based processes such as plasma transferred wire arc (PTWA) can reach even higher temperatures over 10,000°C which make it particularly suitable for depositing materials such as ceramics and is commonly used by automobile manufacturers to coat lightweight cylinder bores [2]. Although effective, the coating formation at elevated temperatures can result in undesired thermal effects such as oxidation of the material as well as a loss of nanostructure in the coating [5]. Other undesirable effects such as phase changes, decomposition and preferential evaporation can also occur as a result of high processing temperatures [6].

1.2 Cold Spray Technology

Across the various TS techniques, there exists a relationship between processing temperature and spray velocity where higher temperatures require less particle velocity for successful coating formation. In recent years, cold spray (CS) has emerged as a promising powder deposition technology that lies essentially on the other end of the spectrum as plasma-based techniques. CS is a solid-state process where microparticles typically between 1 and 50 μm in size are accelerated to supersonic speeds through a de Laval nozzle by a stream of inert gas such as nitrogen or helium as shown in Figure 1.2. Throughout the process, temperatures are maintained well below melting. By doing so, not only are undesirable thermal effects elegantly avoided but dense coatings can be deposited with both high efficiency and rate. The resulting coatings can be extremely thick with 2.5 mm copper coatings having been deposited over stainless steel manifolds in rocket engines. Deposited coatings can not possess high strength, hardness and wear resistance by themselves, but also exhibit high bond strength with the substrate which improves the overall cyclic performance of the coated part [6].

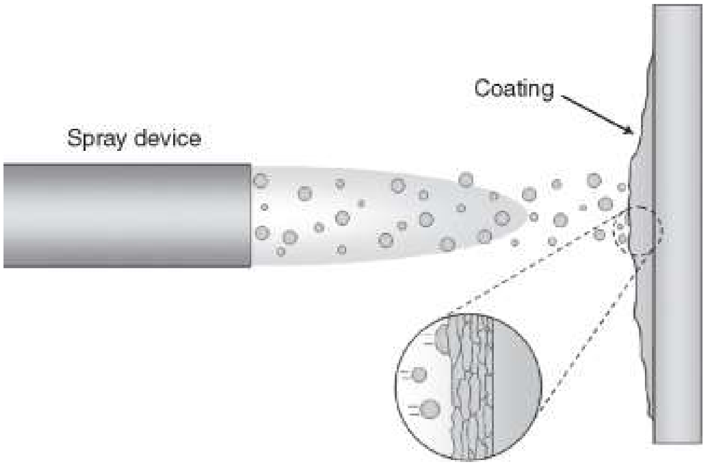

Figure 1.2 Schematic representation of the cold spray process [7].

Nevertheless, no process is perfect and CS still has several disadvantages. First and foremost, there exists a significant shot-peening effect in the coating due to the repeated high-velocity impacts of particles on the substrate. This results in a near-zero ductility in the CS coating in the as-sprayed condition which can be problematic in some applications. Furthermore, CS is only able to properly deposit materials or composites on substrates where both have a certain degree of ductility, as successful bonding in the process is reliant on severe plastic deformations. Consequently, the range of viable materials is limited in CS compared to conventional TS, as coatings deposited on ceramic substrates for example show only limited bond strength [6].

Rather than relying on thermal energy to cause bonding, cold spray uses kinetic energy and contact pressure to remove the oxidation layer on the substrate. This results in intimate metal to metal contact and subsequently under the high contact pressures, induces metallurgical bonding and mechanical interlocking [8]. However, in order to remove the oxide layer, the substrate and particle must undergo the aforementioned severe plastic deformations. The entire process occurs rapidly on the nanosecond scale as the powder particle velocity required to achieve bonding, or critical velocity, can be upwards of 800 m/s [9]. There also exists a maximum particle velocity above which erosion effects serve to prevent bonding [10], however identification of this velocity lies beyond the scope of the present research.

1.3 Motivation, Objectives and Methodology

In the formation of a CS coating for any application, it is essential to identify the critical velocity at which bonding occurs. However, this value is highly dependent on a number of variables such as particle/substrate material, particle size, impact temperature, oxide layer thickness and oxygen content [11, 12, 13, 14]. Nevertheless, as there is a distinct threshold velocity at which bonding occurs, this suggests that there must likewise be a distinct mechanism that causes bonding. Due to the speed and physical scale at which the impact and subsequent impact-induced bonding occurs, it is difficult to observe the threshold metric that must be attained to achieve bonding. As a result, the importance of accurate numerical modeling that is able to quantify bonding effects directly in a simulation is emphasized. Through this, bonding, bond strength and other mechanical properties may be accurately predicted through numerical simulations which specifically account for the extreme CS conditions.

Previous work has been done within the Fatigue and Stress Analysis Laboratory (FATSLAB) in developing the numerical modeling framework for a direct bonding model within a particle-based modeling framework. This work culminated in the development of a strain-like history variable conjugate to a rate-dependent evolution law that allows introduction of a bonding criterion for contacting surfaces. It was implemented within an in-house code based on the Material Point Method (MPM) [15]. This work was able to validate the modeling framework and establish a pathway for its calibration to the observed particle bonding behavior; however, it did not address the critical issues of mesh-dependence which undermines its accuracy in predicting critical components of the observed behavior such as bond initiation site and material jetting. Detailed discussions on the modeling technique will be presented in Chapter 2 and 3 while the existing bond model will be presented at the beginning of Chapter 4.

This thesis aims to further develop the existing bonding model developed within FATSLAB and address the issues of the previous model. Additional features will also be added to further improve the theoretical accuracy of the entire numerical model. Ultimately, the goal is to develop a continuum-based model from which values can be extracted to give proper predictions of bonding occurrence and bond quality for a given set of material and CS process parameters. Formally, the objectives of this thesis are as follows:

- Develop a finite element program based on a framework which is specifically tailored to the extreme strain and strain rate conditions of the CS process. This extends to the consideration of specific numerical components which include but are not limited to specific strength models, melt models and infinite media.

- Develop and implement a novel bonding model within this suitable numerical framework based on physical and theoretical knowledge, such that the effects of adhesion forces on material behavior are represented directly within a simulation.
- Extract information from the bonding model on bonding occurrence and bond quality in single and multiparticle impacts.
- Enable predictions of the necessary particle critical velocity for a given set of process and material parameters.

To demonstrate that the proposed bonding model and modeling framework satisfies the above-stated objectives, the following strategies will be employed:

- The bonding model must show similar performance irrespective of the level of system discretization. Consequently, the bonding model must be based on a value within the simulation which is insensitive to discretization level. To identify an appropriate measure to base the bonding model upon, convergence tests will first be conducted without bonding considerations.
- To evaluate that the proposed bonding model and the metric its based upon is reasonably insensitive to discretization, tests will be conducted with a range of discretization levels and their results compared. The bonding model must show similar performance to discretization level to ensure robustness of the numerical method.
- A measure will be identified and extracted from model calibration tests that can act as a reasonable measure of bond quality. This constitutes a first step towards future development in predictions of mechanical properties such as bond strength of the deposited coating.
- The ability of the final bonding model, calibrated for a specific material combination, to accurately predict material behavior and critical velocity of single-particle impacts will be tested for different particle sizes and compared with experimental results.
- The model will be generalized to handle multiparticle impacts and predict cohesion in addition to adhesion. This will allow for future large-scale simulations where the properties of an entire CS part/coating may be predicted.

1.4 Thesis Outline

Chapter 2 will present the theory behind bonding in CS, review basics of the most commonly used finite element methods, analyze their advantages and disadvantages then cover some existing models that have been developed for bonding. Fracture modeling is also briefly discussed due to its similarity to as essentially an equal but opposite phenomenon to bonding. Chapter 3 presents the Material Point Method (MPM) used to model the current process in detail and presents some additional numerical considerations to improve performance in conditions specific to CS. Chapter 4 describes the development process for the novel bonding model used to directly simulate bonding effects and the specific steps taken to address discretization sensitivity concerns. Chapter 5 shows the final bonding model performance within an MPM framework, discusses the single-particle and multiparticle impact results, and compares its performance with experimental observations and other numerical results. Chapter 6 concludes the thesis and briefly discusses future works.

Chapter 2 Literature Survey

Despite the importance of numerical modeling in high-velocity impact-induced bonding, most research into CS bonding mechanisms has been conducted using commercial finite element software [8, 16, 17]. In the following sections, a review of CS benefits in various applications is first performed. Then, an analysis of the predominant bonding mechanisms and theories for impact-induced bonding is conducted. Following, the basic techniques behind conventional FEA software is discussed and some notes of their shortcomings in simulating the extreme conditions observed in CS. Finally, a review of previous bonding models is presented, and a relation drawn to fracture modeling which already has a strong theoretical foundation.

2.1 Cold Spray Applications

As a solid-state powder deposition process, CS has been primarily applied as a coating method that serves to improve the mechanical properties of an existing part. A major application of CS coatings has been in improving the fatigue performance of existing parts. Ghelichi et al. [18] have shown that by coating an Al5052 specimen with a thick (> 2 mm) layer of Al7075 feedstock powder, fatigue strength is able to be significantly increased by up to 30%. The fatigue strength of the overall coated part appeared to follow the fatigue endurance of the stronger component as well as be influenced by the coating-substrate bond strength. A similar result was observed by Dayani et al. [19] with deposition of high-density Al7075 coatings on AZ31B substrate for the purposes of lightweighting. Higher fatigue strength in the coating resulted in an increase of 25% in sample fatigue strengths at 10 million cycles. In addition to the contributions of a more resistant coating, the work-hardening effect of CS impacts which acts similarly to pre-process grit-blasting and serve to induce residual stresses, increasing fatigue strength [20]. Final, residual stresses in CS coatings are certainly beneficial to fatigue performance but have also been shown by Marzbanrad et al. [21] to be detrimentally affected by carrier gas temperature which may serve to recover residual stresses and induce grain growth. Nevertheless, the residual stress state has been shown to be controllable by adjusting the heat input and heat transfer rate through changes to nozzle speed, powder feed rate and heat sinking/insulation of the substrate [22].

Despite the potential of Mg alloys for lightweighting given their low density and high specific strength, Mg is extremely prone to corrosion effects and thus have not seen much use in humid/aqueous environments. However, CS coatings have shown to be extremely effective in counteracting this. Diab et al. [23] compared AZ31B samples that were uncoated with those that were coated with pure Al using CS. In their accelerated salt spray corrosion test, the Al coated sample reduced average weight loss from 90% after 33 days to < 10% after 90 days. However, the corrosion fatigue strength showed no significant improvement as the lower fatigue strength of pure Al relative to AZ31B resulted in early fatigue cracking in the coating, allowing for penetration of the corrosive solution into the Mg substrate. In any case, the improved corrosion resistance under non-cyclic conditions is still beneficial and can be attributed to the strong bond strength and low porosity of the pure Al coating.

The addition of a CS interlayer to friction-stir butt welded joints has also shown potential for increasing tensile strength while simultaneously improving ductility [24]. Hou et. al [24] reported an increase of 25% in tensile strength and increase of ductility from 5.5% to 10.5% with the addition of an Ni interlayer to Al alloy friction-stir butt welding on Cu substrates. Post-processing techniques such as friction-stirring have been shown to increase density and hardness of CS coatings through refinement of precipitates and grains [25]. Meanwhile, post-annealing is capable of improving fracture strength and bond strength through formation of intermetallic layers in Al7075 deposition on AZ31B substrates [26]. The effects of post-spray heat treatment has also been shown by Tang et al. [27] to significantly increase hardness and abrasive wear resistance of Ti-WC particles sprayed onto stainless steel substrates with a Ti interlayer. This was shown to be as a result of a self-propagating high temperature synthesis reaction which formed TiC between the WC grains and Ti interlayer. Given these results, it is apparent that there exists a wide range of post-processing techniques which may be applied to alter CS coating properties and achieve the desired material properties.

From the above works, there are clearly several ways CS may be of benefit in various applications. It has been experimentally shown that basic coating qualities such as porosity and bond strength in addition to process parameters like gas temperature and nozzle speed are directly related to mechanical properties such as fatigue strength, corrosion resistance and residual stress. Post-processing techniques may also be applied to similarly change the phase composition and microstructure within the coating. With this knowledge, developing a numerical model capable of accurately predicting CS coating parameters is valuable to allow production of components with optimized mechanical properties. As an initial step towards this goal, the focus of the present work is to first develop a model capable of predicting bonding within an appropriate numerical framework. By extension, the effects of bond forces on material behavior will be directly included within the simulation, thus enabling the modeling of a full coating build-up process involving large numbers of particles.

2.2 Cold Spray Bonding Theory

The precise mechanisms behind bonding are difficult to identify through experiments due to the speed at which the process occurs. Classical works using mesh-based finite element simulations have suggested that bonding is due to material jetting resulting from adiabatic shear instability (ASI) [28, 8]. ASI is assumed to be achieved based on the reasoning that as impact velocity increases, so does the amount of adiabatic heating. Figure 2.1 provides a schematic representation of the difference between isothermal and adiabatic hardening/softening. In an ideal material with uniform stress, strain, temperature and microstructure distributions, the “Adiabatic” softening curve can continue indefinitely. However, in a real non-uniform material, shearing, heating and subsequent softening becomes highly localized leading to behavior like what is shown by the “Localization” curve. The significant amount of thermal softening results in a near-zero flow strength value enabling the large, localized shear deformations. These deformations manifest themselves as material jets near the perimeter of the contact interface which remove surface oxides and allows for intimate contact between bodies [8]. Under the high normal contact pressures from impact, metallurgical bonding and mechanical interlocking occur which are the physical mechanisms behind bonding.

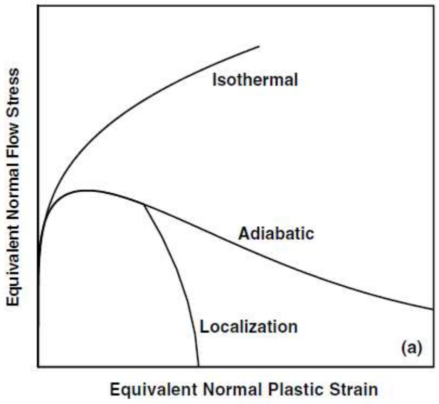

Figure 2.1: Schematic representation comparison of the stress-strain curves in normal strain-hardening (Isothermal) material, adiabatically softened material (Adiabatic) and in a material undergoing adiabatic shear localization (Localization) [8].

More recently, Hassani et al. [16] suggested ASI was not required for bonding but rather a hydrodynamic spall process is the cause behind jetting and subsequent bonding. Their finite element simulations were based on a Coupled Eulerian-Lagrangian (CEL) framework and showed that the material jetting which leads to bonding is attributed to the release of hydrodynamic pressure. This occurs as a free surface is formed between the compression waves of the Eulerian particle and Lagrangian substrate as shown in Figure 2.2. Nevertheless, both theories still point towards material jetting as being intricately linked with bonding phenomena. This knowledge in addition to the observed existence of a critical velocity, makes it reasonable to postulate that there exists a critical threshold level of material jetting that must be achieved to result in bonding.

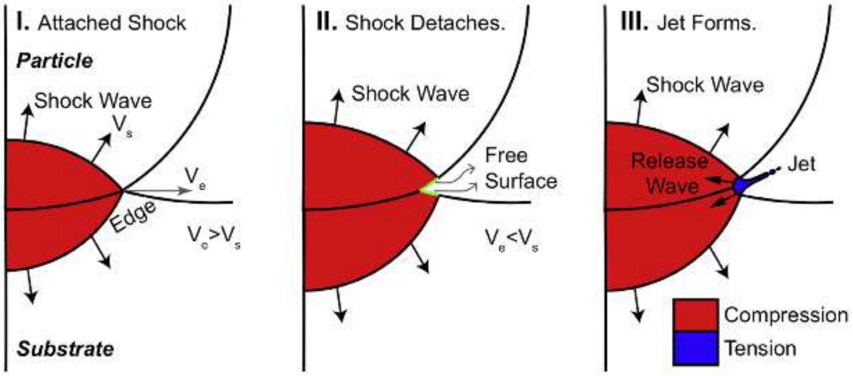

Figure 2.2: Schematic representation of jetting in cold spray: Stage I. Impact induces a shock wave. Stage II. Shock detaches form the leading edge. Stage III. Jet forms on the basis of pressure releases. Note: the uniformity of the colors is not meant to suggest uniform pressure [16].

With both ASI and hydrodynamic spall, it is critical to note that both theories merely serve to explain why material jetting occurs. It is undisputed in current literature that there is an important relationship between material jetting and bonding such that bonding is only observed when there is sufficient material jetting. Experimentally, Hassani et al. [12] have been able to observe the highspeed microparticle CS impacts of Al on Al and Au on Au. Figure 2.3 shows their observations of similarly sized particles impacted at a speed below and above the critical velocity. It can be seen that despite large plastic deformations in both particles impacted at the lower velocities, bonding only occurs once even larger deformations and more specifically, material jetting occurs. Material jetting can be seen in the images by the cloud of fragmented material near the perimeter of the contact interface as labelled by the white arrows. Subsequent analysis through scanning electron microscopy of the Au on Au impacts presented in Figure 2.4 shows the lips around the perimeter of the contact interface associated with material jetting.

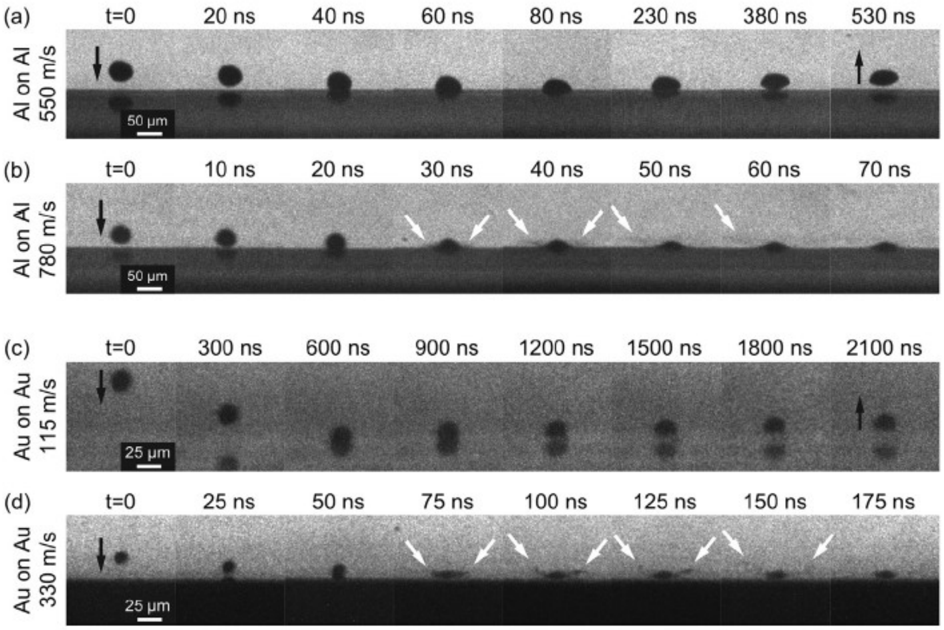

Figure 2.3: Single particle impacts of Al on Al (a, b) and Au on Au (c, d) at velocities below (a, c) and above (b, d) their respective critical velocities. White arrows indicate the presence of material jetting, which is essentially in achieving adhesion [12].

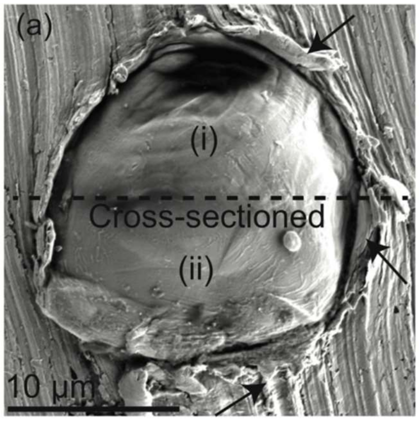

Figure 2.4: Lips around the perimeter of the contact interface which show the lips associated with material jetting in Au on Au impacts [12].

2.3 Modeling Techniques

Any solid mechanics finite element analysis (FEA) technique is essentially the breaking up of an object into a large, finite number of smaller elements. Each element can be differently shaped however the focus of this thesis will be on the standard hexahedron shape consisting of 8 nodes and 6 sides used in 3D analysis. Figure 2.5 shows the hexahedron shape and lists the nodal parent coordinates for an 8-node hexahedron element. Without going into excessive detail, the origin of the parent coordinate system is at the center and reaches a maximum value of 1 or -1 at the nodes. This rule is maintained irrespective of any deformation or change in shape of the element.

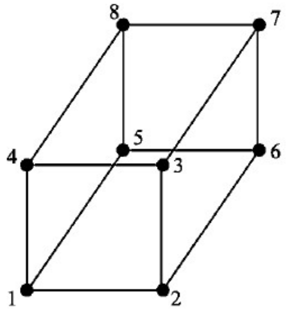

I	ξ_I	η_I	ζ_I
1	−1	−1	−1
2	1	−1	−1
3	1	1	−1
4	−1	1	−1
5	−1	−1	1
6	1	−1	1
7	1	1	1
8	−1	1	1

Figure 2.5: 8-node hexahedron element with nodal parent coordinates [29].

The thermomechanical properties across the body of each element can be found through a linear interpolation of the nodal values. By use of the parent coordinates, the same interpolation equations or shape functions can be used throughout a simulation which is critical to properly solve any finite element problem. The standard shape functions for an 8-node hexahedron element are commonly known and shown below, where ξ, η and ζ are the natural coordinates of the particle ranging from -1 to 1.

$$N_I(\xi, \eta, \zeta) = \frac{1}{8}(1 + \xi_I\xi)(1 + \eta_I\eta)(1 + \zeta_I\zeta) \tag{2.1}$$

With this ability to map nodal values throughout the body of an element, it is then possible to interpolate thermomechanical properties such as displacement, force, stress and temperature at any point in an element as a function of its nodal values and a set of non-changing shape functions in natural coordinates. The precise governing equations, formulated from the principle of virtual work or the weak form of equations derived from conservation laws, are not presented here for brevity however will be described in detail within Chapter 3 when presenting the MPM. These governing equations and shape functions are similar within any mesh-based finite element solver. The primary difference lies in how the bodies are discretized (i.e. meshed) as well as the formulation of the constitutive equations which govern material properties such as stress. A brief description of the most common finite element formulations follows.

2.3.1 Lagrangian Methods

A Lagrangian FEM is characterized by its use of a mesh that deforms with the material. In a Lagrangian formulation, the mesh distorts as the material is deformed under an applied load.

Historically in FEA, the predominant analysis techniques in solid mechanics revolved around using Lagrangian meshes. This can be primarily attributed to their ease in dealing with more complex imposed boundary conditions and ability to easily follow points within a material in order to track history-dependent variables. Figure 2.6 shows a typical simulation result observed using a Lagrangian formulation of an Al particle impact on an Al substrate in CS near the critical velocity.

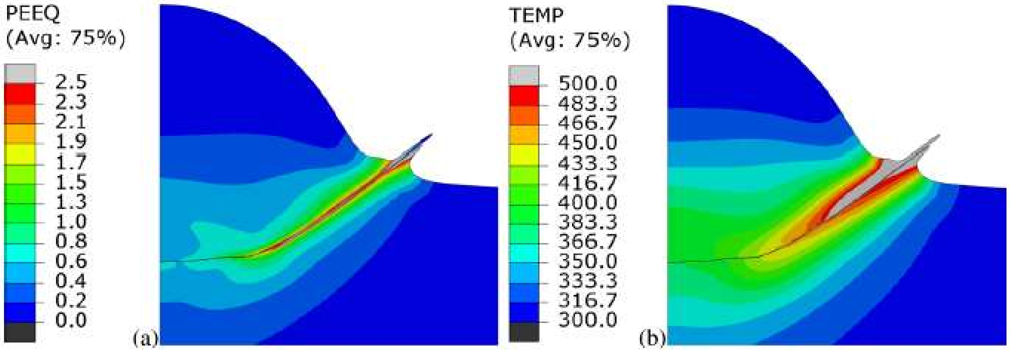

Figure 2.6: Contours of the (a) equivalent plastic strain and (b) temperature for Al/Al impact obtained using the Lagrangian method at 19 ns post-impact [30].

From the contours, it can be seen that there is noticeable material jetting near the perimeter of the contact surface. As previously mentioned, although there may be several theories on what causes this material jetting, it is undisputed based on experimental evidence that this jet formation is critical to impact-induced bonding. The fact that this phenomenon is somewhat captured within a Lagrangian formulation is good, however the actual material jets are sharp and unphysical in shape. This results in heavy mesh distortion in these regions which leads to critical errors in severe deformation problems such that simulations like the one by by Xie et al. [30] in Figure 2.6 were unable to be completed and forced to be terminated at 19 ns.

Mesh distortion is as a result of the primary issue of having a mesh which deforms with the object. Although insignificant in the modeling of small deformations, if strains are large, element distortions become severe and result in a failure of the simulation due to a negative or near-zero element Jacobians. The extreme strains within the jetting region in CS can be as high locally as 450%, leading to the highest inaccuracy in the most sensitive region for accurate bond modeling [16, 31]. Adaptive meshing can be used to alleviate mesh distortion problems to a degree, however frequent remeshing can cause non-conserving energy variation and unphysical material jetting [28]. Overall, it is clear that a pure Lagrangian formulation is not ideal for modeling the high strain CS process.

2.3.2 Eulerian and Other Mesh-based Methods

To address the issues of Lagrangian formulations related to large deformations and mesh distortion, Eulerian methods typically used in fluid modeling have been applied to solid mechanics. In a Eulerian formulation, material mass flows through stationary points of a mesh that does not deform with the material. Consequently, the mesh no longer deforms at all and is able to avoid the inaccuracies and critical solver errors seen in a Lagrangian formulation. Finite element simulations by Yu et al. [17] have been conducted using ABAQUS/Explicit with a Eulerian formulation, producing reasonable predictions of the critical velocity of Cu particles impacting on same material substrate. Figure 2.7 shows a contour of the particle impact from these simulations, where it can be seen how the solid material is simulated to behave similarly to a liquid.

Although a Eulerian formulation allows for more accurate modeling of the material jet in both the particle and substrate, it is not without disadvantages. Since Eulerian methods only calculate material quantities advected between elements, it is difficult to enforce boundary conditions and model deforming interfaces which are prevalent in contact problems. Furthermore, there exists other shortcomings such as numerical dissipation and difficulties in tracking history dependent variables within a body which are important in solid mechanics and not originally an issue with Lagrangian methods [32].

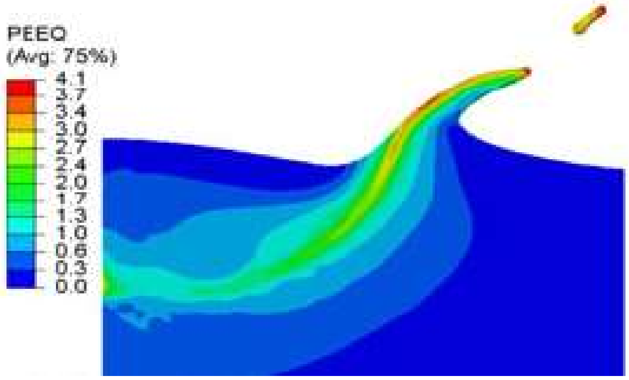

Figure 2.7: Contour of equivalent plastic strain for Cu particle impacting a Cu substrate at 500 m/s [17].

An alternative is to combine Lagrangian and Eulerian meshes in discretizing a body to combine the advantages of both methods [30, 33]. The Arbitrary Lagrangian-Eulerian formulation (ALE) does this where the user is required to specify the mesh combination based on the desired mesh motion. As a result, this places much of the emphasis on the user in selecting the appropriate combination in order to achieve a result which properly combines the advantages of both mesh types. A study by Xie et al. [30] compared ALE performance with a Lagrangian formulation and noted that although excessive mesh distortion was avoided, a new type of unrealistic result is observed. Specifically, the equivalent plastic strain is observed to reach a maximum value then slowly decrease over time when physically, it should reach a plateau like in the Lagrangian simulations. This result was attributed to interpolation errors resulting from the adaptive remeshing and the high-strain gradients near the interface.

Figure 2.8 shows the contours of a particle impact near its critical velocity calculated using an ALE mesh. To note, it can be seen that with this ALE formulation, accurate modeling of the material jet is still an issue as it becomes smooth and rounded contrary rather than the cloud of fragmented material seen experimentally by Hassani et al. [9]. Rather than using ALE, most recent research utilizes a Coupled Eulerian-Lagrangian (CEL) approach with a Lagrangian substrate and Eulerian particle with improved results over ALE [16, 30]. In any case, there are inherent issues with both Lagrangian and Eulerian FEMs in modeling the extreme conditions seen in CS which are not easily solved by combining the two in various ways.

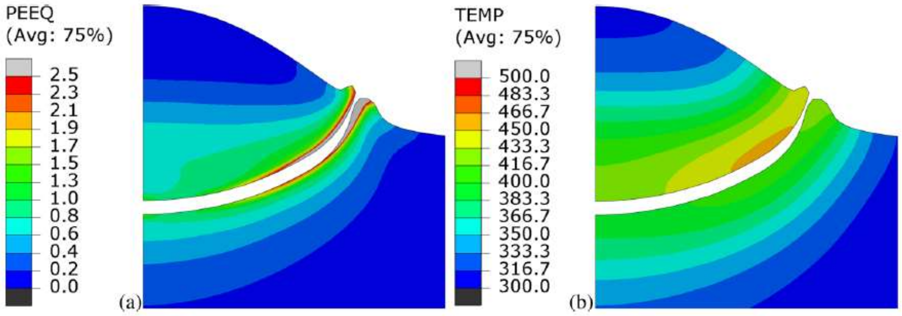

Figure 2.8: Contours of the (a) equivalent plastic strain and (b) temperature for Al/Al impact obtained using an ALE mesh [30].

2.3.3 Particle-based Methods

None of the above mesh-based techniques are ideal in their modeling of severe-deformation problems. As such, the use of particle-based methods has emerged as a promising alternative to combine the advantages of Lagrangian and Eulerian methods. Smoothed particle hydrodynamics (SPH) is one such particle-based FEM originally developed for astrophysics simulations that has been applied to CS [34, 35, 36]. Rather than discretizing a body into a finite number of meshed 3D elements, SPH instead discretizes a body into a number of particles. These particles are essentially state variables which carry all the properties necessary to describe the material such as mass, velocity, pressure and stress. Although technically a Lagrangian particle method as the particles deform with the body, the particles are also free to move and become disordered. No background mesh is present at all thus avoiding the most problematic mesh distortion issues of traditional Lagrangian methods.

Without a mesh, the interpolation previously achieved through use of shape functions is impossible and an entirely different method must be implemented. In SPH, this interpolation is achieved through a weighting function known as an SPH kernel, represented mathematically by Equation 2.2 [37]:

$$A(x_a) = \sum_{b \in \Lambda_a} A_b \frac{m_b}{\rho_b} W(x_a - x_b, h) \tag{2.2}$$

where A represents a vector function of position x, m_b the mass of particle b and ρ_b the density of particle b. $W(x_a - x_b, h)$ is the actual kernel function itself. A kernel function is essentially a smoothed delta function with added convergence requirements to ensure mathematical consistency. The h parameter within the kernel function is called the smoothing length and defines the radius of the kernel, or the resolution of the simulation. Each particle has a domain of influence that is represented by Λ, with the interparticle distance being typically less than h [37]. The gradient of A can be calculated by simply taking the derivative of the kernel function which replaces shape function derivatives used in mesh-based FEMs. Figure 2.9 gives a visual representation the SPH kernel function used for interpolation in the simulation space.

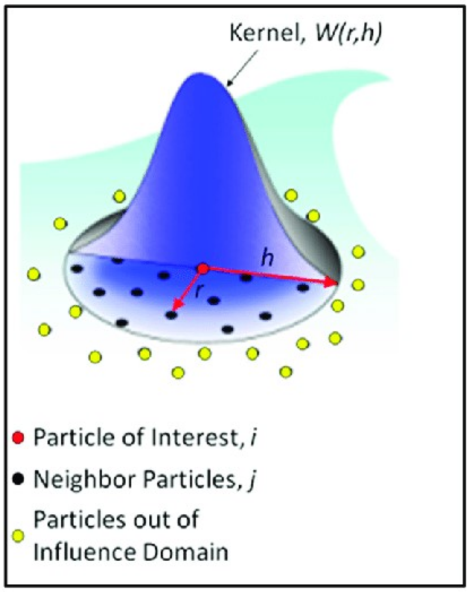

Figure 2.9: Interpolation technique used in the SPH method [38].

In preliminary studies of CS impact using SPH, oblique impacting copper particles were simulated with results noted by Li et al. [39] to be fairly well-matched to experimental evidence. Comparisons of SPH and Lagrangian methods not only showed improvements in avoiding mesh distortion, but also reduced dependence on particle weight in SPH than mesh type and size in Lagrangian methods [40]. Bonding of ceramic particles in a deposition method similar to CS has also been studied through SPH [41]. However, the contact boundaries in the above studies were treated as free surfaces which may reasonably simulate deformation behavior but are lacking in providing accurate predictions of critical and maximum velocities. Later, Manap et al. [34] were able to define this boundary condition and include particle-substrate interaction effects. Through this, they were able to use the ratio of rebound and deposition energy to evaluate CS coating quality, verifying results based on experimentally measured quantities. Further SPH simulations have also been conducted including the effects of varying oxide layer thickness which were also able to closely match experimental results [42]. Overall, the use of SPH in CS process modeling showed good results in predicting critical as well as maximum and optimum impacting particle velocities. Nevertheless, as a particle-based method, SPH is not without disadvantages such as requiring computationally expensive neighbor searching and tensile instability [32].

2.4 Constitutive Models

2.4.1 Johnson-Cook Strength Model

When modeling microparticle impacts, it is essential to begin with an accurate continuum description of material behavior. This is especially important when the conditions are extreme as in CS particle impacts at supersonic velocities which result in extreme strains and strain rates as well as moderate temperature changes. In these cases, predictions by some constitutive models may no longer be representative of experimental observations. Despite some of its known shortcomings at high strain rates, the Johnson-Cook (JC) equation has been by far the most widely implemented constitutive model in simulating CS [43, 28, 8, 16, 35, 34, 11, 44, 45]

$$\sigma_y = (A + B\varepsilon^n)(1 + C ln\dot{\varepsilon}^*)(1 - T^{*m}) \tag{2.3}$$

This equation describes the flow stress in terms of three components, taking into account the effects of strain hardening, strain rate hardening and thermal softening. However, the JC model is a purely empirical model was fit experimental data only up to $10^5\ s^{-1}$ [46]. In comparison, the effective plastic strain rates during the simulated CS process can reach strain rates several orders of magnitude higher, up to $10^9\ s^{-1}$. As a result, the JC model may present inaccuracies at the high strain rates present during CS which lie well beyond the experimental range it was fitted to. In particular, its simple linear logarithmic relation between flow stress and strain rate hardening proves inaccurate at high strain rates [45]. Albeit not as impactful in CS, the JC model has also been noted to have unrealistically small strain-rate dependence at high temperatures [47]. Due to these issues, which are particularly relevant during the high-strain rate CS process, use of an improved constitutive model will be beneficial.

2.4.2 Preston-Tonks-Wallace Strength Model

The Preston-Tonks-Wallace (PTW) model has been developed with specific components that can model plastic deformation in the overdriven shock regime (strain rates greater than $10^7 s^{-1}$) [47], making it much more suitable for CS fconditions [47, 48]. Rahmati and Jodoin [49] have implemented the PTW model in numerical studies of CS impacts within an ALE framework specifically due to its improved accuracy at extreme strain rates. Due to these benefits, the original MPM code developed by Zhang et al. [32]. has been used as a basis with the addition of a numerical implementation of the PTW strength model, used for calculating flow stress within each material point. The flow strength in the PTW model can be calculated as follows:

$$\sigma_y = 2\left[\tau_s + \alpha \ln\left[1 - \psi\, exp\left(-\beta - \frac{\theta\varepsilon_p}{\alpha\psi}\right)\right]\right]\mu(p, T) \tag{2.4}$$

$$\alpha = \frac{s_0 - \tau_y}{d}, \beta = \frac{\tau_s - \tau_y}{\alpha}, \psi = \exp(\beta) - 1 \tag{2.5}$$

where ε_p is the plastic strain, τ_s is the normalized work hardening saturation stress, τ_y is the normalized yield stress, h is the hardening constant, d is a dimensionless material constant and s_0 is the value of τ_s at zero temperature. Furthermore, μ is the shear modulus which has been shown to be able to be accurately predicted by the Mechanical Threshold Stress shear modulus model as only a function of temperature [47]:

$$\mu(T) = \mu_0 - \frac{D}{\exp\left(\frac{T_o}{T}\right) - 1} \tag{2.6}$$

where μ_0 is the shear modulus at 0 K, D and T_0 are material constants and T is the material temperature. Lastly, τ_s and τ_y are defined as follows:

$$\tau_s = \max\left\{s_0 - (s_o - s_\infty) erf\left[k\hat{T}\, ln\left(\frac{\gamma\dot{\xi}}{\dot{\varepsilon}_p}\right)\right], s_o\left(\frac{\dot{\varepsilon}_p}{\gamma\dot{\xi}}\right)^{s_1}\right\} \tag{2.7a}$$

$$\tau_y = \max\left\{y_0 - (y_o - y_\infty) erf\left[k\hat{T}\, ln\left(\frac{\gamma\dot{\xi}}{\dot{\varepsilon}_p}\right)\right], \min\left\{y_1\left(\frac{\dot{\varepsilon}_p}{\gamma\dot{\xi}}\right)^{y_2}, s_o\left(\frac{\dot{\varepsilon}_p}{\gamma\dot{\xi}}\right)^{s_1}\right\}\right\} \tag{2.7b}$$

where γ, k, s_0, s_1, s_∞, y_0, y_1, y_2 and y_∞ are all material parameters with $\hat{T} = T/T_m$ and

$$\dot{\xi} = \frac{c_T}{2a} = \frac{1}{2}\left(\frac{4\pi\rho}{3M}\right)^{\frac{1}{3}}\left(\frac{\mu(T)}{\rho}\right)^{\frac{1}{2}} \tag{2.8}$$

where c_T is the transverse sound speed, a is the atomic radius, ρ the density and M the atomic mass of the material. Note that $\dot{\xi}$ is in fact equal to the reciprocal of the time required for a transverse wave to cross an atom [48]. It serves as a scaling factor for the strain rates such that it always appears within the dimensionless strain rate variable of the PTW model as $\dot{\varepsilon}_p/\dot{\xi}$. In terms of the units to be used, ρ will be in $ng/\mu m^3$, M in ng and μ in MPa. Working out the units, the reciprocal of the time for a transverse wave to cross an atom $\dot{\xi}$ will be in μs^{-1}, therefore the strain rates within the numerical implementation must also be in μs^{-1} to match.

In this thesis, the focus is in simulating Al particle impact on an Al substrate. Table 2.1 below lists all the material properties and PTW parameters for Al used in this study [49]. It should be noted that certain PTW model parameters have largely been identified or calibrated using data from bulk material which may differ in composition and microstructure from the microparticles considered in CS. Further, they have not been identified under the extreme strain and strain rate CS conditions. To address this, in a recent study by Razavipour and Jodoin [50], the PTW model parameters for Cu and Ni have been recalibrated using experimental coefficient of restitution (CoR) data from CS impacts on same material substrates. Although no bonding effects were considered, the recalibrated model parameters showed significantly improved accuracy in predicting the CoR as well as the crater diameter from rebounded particles over the original PTW model. Recalibration of the PTW parameters for Al-Al impacts have not yet been performed but given these results, may be required in the future.

Table 2.1: Al material properties and PTW parameters [38].

PTW Parameters	**Aluminum**
Strain rate dependence constant (γ)	2.04e-5
Strain hardening rate (θ)	0.01156
Strain hardening constant (d)	3
Yield stress constant at 0 K (y_0)	0.0115
Yield stress constant at melting (y_∞)	0.002003
Medium strain rate constant (y_1)	0.0168
Medium strain rate constant (y_2)	0.2339
High strain rate exponent (s_1)	0.2034
Saturation stress at 0 K (s_0)	0.01489
Saturation stress at melting (s_∞)	0.002819
Temperature dependence constant (κ)	1.3
Atomic mass (M), kg	4.48039×10^{-23}
Shear modulus at 0 K (G_0), GPa	28.8
Material constant (D), GPa	3.44
Temperature material constant (T_0), K	215

Although a different constitutive model is introduced for calculating the deviatoric stress components and flow stress, the Mie-Grüneisen equation of state remains the method used to calculate the pressure within the shock-compressed solid, similar to previous works [16, 47, 51]. Exact details of how this is implemented may be found later in Section 3.5.2.

Furthermore, it is known that the melting temperature can increase drastically with pressure [47], which can be extremely relevant in high strain-rate processes such as CS. As melting temperature is an input to many PTW parameter values, it is deemed necessary to consider this within a numerical model. One method to consider the effects of pressure on melt temperature is through a modified Lindemann law from the Steinberg-Cochran-Guinan (SCG) melt model [52]:

$$T_m(\rho) = T_{m0} \exp\left[2a\left(1 - \frac{1}{\eta}\right)\right] \eta^{2\Gamma_0 - a - \frac{1}{3}} ; \; \eta = \frac{\rho}{\rho_0} \tag{2.9}$$

where T_{m0} is the melt temperature at $\eta = 1$ (ambient pressure), a is the coefficient of the first order volume correction to Grüneisen's gamma (Γ_0). Although other melt models such as the Burakovsky-Preston-Silbar model exist, they are much more involved require more detailed definitions of the shear and bulk modulus as functions of pressure [47].

2.5 Bonding Models

2.5.1 Cohesive Zone and Adhesion Models

Historically, in many studies on CS bonding mechanisms, bonding has either not been directly considered in the simulations or has been assessed through numerical analysis of results during post-processing [41, 28, 30, 53, 33, 54]. Li et al. [39] have noted that even without a bonding model, impacted particles using with SPH did not rebound from the substrate. They attributed this phenomenon to the interpenetration of SPH particles from different bodies into each other near the interfacial surface. Nevertheless, a formal bonding model with a sound theoretical basis will improve the robustness of the simulation. There exists only a few studies which have incorporated bonding effects directly into simulations. Many of these studies, have examined the use of the Dugdale-Barenblatt cohesive zone model in modeling bonding during CS with SPH [34, 55, 56, 57, 58]. The Dugdale-Barenblatt model, like many cohesive models, originates from non-linear fracture mechanics theory. In brief, this model was used to describe non-linear fracture processes and stress transfer across cracks in various types of materials by considering a zone across and extended crack tip where cohesive forces exist [59]. With this model, so long as the separation distance is less than a critical crack opening distance, a constant cohesive force is assumed to be present. Knowing this, it is clear how a cohesive zone model normally used in fracture modeling can be useful in the simulation of bonding, which is a similar phenomenon on the opposite end of the spectrum.

Although cohesive zone models may be informative, it is unable to model exact bonding behavior as it is incapable of including the requirement for breaking the native oxide layer. To address this, adhesion models such as the one developed by Profizi et al. [35] using the SPH method, were created with an activation and deactivation criterion based on observed simulation variables such shear stress, surface energy dissipation, and element erosion. They were able to accurately predict critical velocity and include a damage value to cause breakage of cohesion before all surface adhesion energy has dissipated in order to predict the maximum impact velocity beyond which erosion will occur. However, the activation criterion for determining when the cohesive stress is applied is based on a measure which lacks a strong physical basis, where a cohesive stress was directly applied on SPH particles when a 30% drop in local yield stress was detected. Nevertheless, the use of energy as a bonding measure has been supported by a recent theoretical study by Sun et al. [60]. They have indicated that jetting is a source of energy dissipation and suggested that there is a threshold level of jetting-induced energy dissipation as a result of material jetting that is required to result in bonding.

Despite the promising results, only a small number of other studies have been conducted which have attempted to directly incorporate adhesion/bonding forces within a simulation, all of which use the concept of an adhesion energy [61, 62, 63, 49]. In a study by Rahmati and Ghaei [45], a separate adhesion model was developed where bonding or successful particle deposition is considered to have occurred when the adhesion energy is higher than the rebound (i.e. elastic) energy. Their model within an ALE framework and is only in its preliminary stages where adhesion energy is assumed to be a function of sublimation energy which is potentially different from the fracture energy required to cause debonding [49]. A similar concept of adhesion and rebound energy to define when bonding has occurred has been applied by a small number of other studies [61, 64].

2.5.2 Adhesion Energy Definition and Bond Strength Prediction

The adhesion energy used in previous energy-based models was determined by Shorshorov and Kharlamov in 1978 [65]. Equation 2.10 describes how the adhesion energy A is used to compare with the rebound energy in simulations to identify bonding is calculated:

$$A = a\% A_{\max}$$
$$where\ a\% = 1 - \exp\left\{-\nu t_c\, exp\left[-\frac{E_a}{kT_c + (1-e_r)m_p v_p^2/2}\right]\right\} \tag{2.10}$$

where ν is the natural frequency of Eigen-oscillations of atoms in the crystal lattice, t_c is the contact time, E_a is the activation energy of chemical bonds, T_c is the contact temperature, e_r is the elastic recoil coefficient, m_p and v_p are the atomic mass and velocity, respectively, of the sprayed particle. The maximum adhesion energy $A_{max} = S_c N_a E_1$ where S_c is the contact area, N_a is the number of atoms in a unit contact plane and E_1 is the energy of a single bond between two atoms evaluated by the sublimation energy. In a similar manner, Shorshorov and Kharlamov [65] have also obtained a relationship for predicting the relative bond strength in CS, given by

$$\sigma = 1 - \exp\left[-\nu t_a\, exp\left(\frac{-E_a}{\alpha_1 kT_c + \alpha_2 m_p v_p^2/2}\right)\right] \tag{2.11}$$

where the new variables introduced are α_1 and α_2, which are the coefficients of utilization of the internal and kinetic energy of the sprayed particle upon impact with the substrate.

It is clear that the above relationships for adhesion energy and bond strength are not based on measures which are easily quantified in practice. In particular, determining the value of α_1 and α_2 can be complicated [63]. Furthermore, it has been pointed out by Rahmati and Jodoin [49] that it is difficult within this bonding model framework to include the effects of oxide layers. Although the use of these measures and the adhesion energy derived from them are certainly valid, the development of a continuum-based direct bonding or adhesion model is sparce. More specifically, no previous adhesion energy model has been developed which only utilizes values from directly within the simulation they are applied within to identify the critical adhesion energy required for bonding. Furthermore, to the best of the author's knowledge, no direct bonding model also developed within an MPM framework, which shows clear advantages over mesh and other particle-based methods.

Chapter 3 Material Point Method Formulation

The process to be modelled by MPM in this thesis is the single-particle impact of an Al particle on a same material cylindrical substrate. Figure 3.1 gives a 2D schematic representation of the initial system used to represent the CS deposition process, with black dots representing material points and red grid lines representing the computational grid. Every simulation is set to begin as the first material point in the particle contacts the substrate at a specified velocity. The following section begins by describing the governing equations and weak form formulation which are similar to traditional FEM. Afterwards, the MPM will be described and the MPM algorithm is presented to explain how the method is implemented numerically in the code.

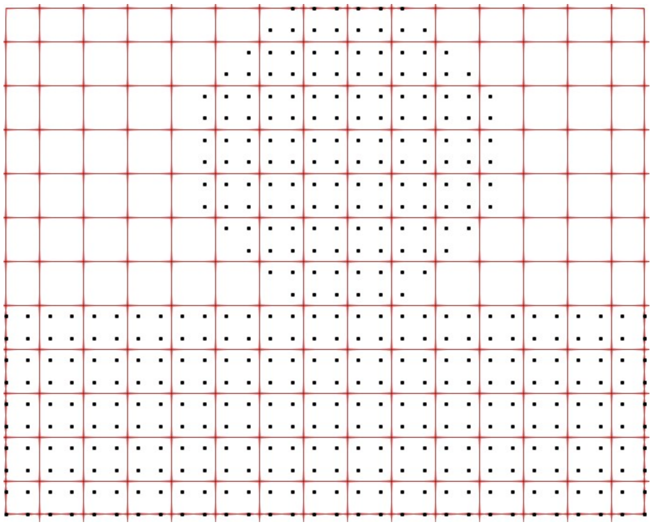

Figure 3.1: 2D schematic representation of the initial system used to model a single-particle CS impact. Red lines indicate the computational grids while black dotes indicate material points.

3.1 Governing Equations

As a continuum-based FEM, the behavior of each body can be defined by a material-specific constitutive equation in addition to a set of governing equations. The governing equations in MPM are based on conservation laws for mass, momentum and energy. These equations are formed in similar fashion to those used in traditional mesh-based FEM; a brief description will be presented in this section.

Rather than a total Lagrangian approach where stress and strain measures are defined with respect to the initial or reference coordinates (typically denoted by $\boldsymbol{X}$ in literature), the updated Lagrangian approach is the most widely used in MPM [32]. Note that per convention, bolded characters are tensor values and dotted terms indicate a derivative with respect to time. In an updated Lagrangian approach, stress and strain measures are defined instead with respect to the current configuration (typically denoted $\boldsymbol{x}$ in literature) using the Cauchy stress and rate of deformation. Furthermore, all gradients and integrals are also to be calculated with respect to the current configuration. For brevity, it is assumed that there is a basic understanding of concepts such as the deformation gradient, rate of deformation, Cauchy stress and, the Jaumann rate of

Cauchy stress [29]. The following section briefly presents the partial differential equations (PDEs) derived from conservation laws.

3.1.1 Conservation of Mass

Before deriving any of the conservation equations, the concept of a material derivative must be presented. The material derivative is the partial derivative with respect to time for any quantity within a moving continuum body. For a volume integral of an arbitrary function $\boldsymbol{f}(\boldsymbol{x}, t)$, the material time derivative can be expressed using Reynolds Transport Theorem [32] as follows:

$$\frac{D}{Dt}\int_{\Omega} f(\boldsymbol{x}, t)dV = \int_{\Omega} \left[\dot{f}(\boldsymbol{x}, t) + f(\boldsymbol{x}, t)\nabla \cdot \boldsymbol{v}\right]dV \tag{3.1}$$

where $\boldsymbol{v}$ is the velocity tensor, dV a current infinitesimal volume element, Ω is a body the volume integral is applied on and ∇ is the gradient operator. Note that $\nabla \cdot \boldsymbol{v}$ is simply the divergence of the velocity tensor v. With the material time derivative defined, we can proceed with defining the conservation laws within a continuum body. The total mass of a continuum body in its current configuration can be expressed in volume integral form as:

$$m = \int_{\Omega} \rho(\boldsymbol{x}, t)dV \tag{3.2}$$

where $\rho(\boldsymbol{x}, t)$ is the local density of the body. In order for conservation of mass to be satisfied, the material time derivative of the mass in body m must be equal to 0. By Reynolds Transport Theorem Equation (3.1), this can be written in the current configuration as

$$\frac{D}{Dt}\int_{\Omega} \rho(\boldsymbol{x}, t)dV = \int_{\Omega} (\dot{\rho} + \rho\nabla \cdot \boldsymbol{v})dV = 0 \tag{3.3}$$

Or

$$\dot{\rho} + \rho\nabla \cdot \boldsymbol{v} = 0 \tag{3.4}$$

Equation (3.4) is known as the continuity equation and can also be written with respect to the reference coordinates. However, for current purposes Equation (3.4) suffices and must always be true in order satisfy the conservation of mass law.

3.1.2 Conservation of Momentum

Another important consideration in any FEM is the conservation of linear momentum. In order for momentum to be conserved, the material time derivative of the linear momentum in a continuum body must be equal to the resultant force acting on it. Mathematically, this is expressed as

$$\frac{D}{Dt}\int_{\Omega} \rho\boldsymbol{v}(\boldsymbol{x}, t)dV = \int_{\Omega} \rho\boldsymbol{b}(\boldsymbol{x}, t)dV + \int_{\Gamma} \boldsymbol{t}(\boldsymbol{x}, t)dA \tag{3.5}$$

where $\boldsymbol{b}$ is the body force per unit mass acting on the continuum body Ω and $\boldsymbol{t} = \boldsymbol{n} \cdot \boldsymbol{\sigma}$ is the traction force acting on the external surface Γ along the normal of body Ω defined by $\boldsymbol{n}$. Again, by Reynolds Transport Theorem, the term on the left-hand side of (3.5) can be rewritten as

$$\frac{D}{Dt}\int_{\Omega} \rho \boldsymbol{v}(\boldsymbol{x}, t) dV = \int_{\Omega} \left[\frac{D(\rho \boldsymbol{v})}{Dt} + \rho \boldsymbol{v} \nabla \cdot \boldsymbol{v}\right] dV = \int_{\Omega} [\rho \dot{\boldsymbol{v}} + \boldsymbol{v}(\dot{\rho} + \rho \nabla \cdot \boldsymbol{v})] dV \tag{3.6}$$

Meanwhile, the divergence theorem can be applied to change the surface integral term on the right-hand side of Equation (3.5) containing the traction force to a volume integral as follows:

$$\int_{\Gamma} \boldsymbol{t}(\boldsymbol{x}, t) dA = \int_{\Gamma} \boldsymbol{n} \cdot \boldsymbol{\sigma} dA = \int_{\Omega} \boldsymbol{\sigma} \cdot \nabla dV \tag{3.7}$$

Combining the above equations and making use of the continuity (3.4), the conservation of linear momentum for an updated Lagrangian approach can be described as

$$\int_{\Omega} (\rho \dot{\boldsymbol{v}} - \rho \boldsymbol{b} - \boldsymbol{\sigma} \cdot \nabla) dV = 0 \tag{3.8}$$

Or

$$\rho \dot{\boldsymbol{v}} - \rho \boldsymbol{b} - \boldsymbol{\sigma} \cdot \nabla = 0 \tag{3.9}$$

This governing equation must be met in order to satisfy the conservation law for linear momentum.

3.1.3 Conservation of Energy

The last conservation law that needs to be considered is that for energy and relates to the first law of thermodynamics. Essentially, the total energy of a continuum body must be equal to the sum of the mechanical work done by the various forces acting on the body and the net heat flux into the body. For the current CS modeling application, there is assumed to be no heat supply and negligible heat flux. As such, the first law of thermodynamics for a continuum body can be expressed as

$$\frac{D}{Dt}\int_{\Omega} \left(\rho e + \frac{1}{2} \rho \boldsymbol{v} \cdot \boldsymbol{v}\right) dV = \int_{\Omega} \rho \boldsymbol{v} \cdot \boldsymbol{b} dV + \int_{\Gamma} \boldsymbol{v} \cdot \boldsymbol{t} dA \tag{3.10}$$

where e is the specific internal energy, $\boldsymbol{b}$ the body force per unit mass and $\boldsymbol{t}$ the surface traction force. Using the divergence theorem and the fact that $\boldsymbol{W}: \boldsymbol{\sigma} = 0$ (due to the skew-symmetric property of $\boldsymbol{W}$ where $\boldsymbol{L} = \nabla \boldsymbol{v} = \boldsymbol{D} + \boldsymbol{W} = \frac{1}{2}(\boldsymbol{L} + \boldsymbol{L}^T) + \frac{1}{2}(\boldsymbol{L} - \boldsymbol{L}^T)$), the last term on the right-hand side of Equation (3.10) can be rewritten as

$$\int_{\Gamma} \boldsymbol{v} \cdot \boldsymbol{t} dA = \int_{\Gamma} \boldsymbol{n} \cdot \boldsymbol{\sigma} \cdot \boldsymbol{v} dA = \int_{\Omega} \nabla \cdot (\boldsymbol{\sigma} \cdot \boldsymbol{v}) dV \tag{3.11a}$$

$$= \int_{\Omega} (\nabla \boldsymbol{v}: \boldsymbol{\sigma} + (\nabla \cdot \boldsymbol{\sigma}) \cdot \boldsymbol{v}) dV \tag{3.11b}$$

$$= \int_{\Omega} (\boldsymbol{D}:\boldsymbol{\sigma} + \boldsymbol{W}:\boldsymbol{\sigma} + (\nabla \cdot \boldsymbol{\sigma}) \cdot \boldsymbol{v}) dV \tag{3.11c}$$

$$= \int_{\Omega} (\boldsymbol{D}:\boldsymbol{\sigma} + (\nabla \cdot \boldsymbol{\sigma}) \cdot \boldsymbol{v}) dV \tag{3.11d}$$

Meanwhile, by making use of what has been shown in (3.7) to eliminate the $\dot{\rho}$ term, the left-hand side of (3.10) can be rewritten as

$$\frac{D}{Dt}\int_{\Omega} \left(\rho e + \frac{1}{2}\rho \boldsymbol{v} \cdot \boldsymbol{v}\right) dV = \int_{\Omega} \left(\rho \dot{e} + \frac{1}{2}\rho \dot{\boldsymbol{v}} \cdot \boldsymbol{v} + \frac{1}{2}\rho \boldsymbol{v} \cdot \dot{\boldsymbol{v}}\right) dV$$

$$= \int_{\Omega} (\rho \dot{e} + \rho \boldsymbol{v} \cdot \dot{\boldsymbol{v}}) dV \tag{3.12}$$

Combining these with Equation (3.10) describing the conservation of energy yields the following expression:

$$\int_{\Omega} [\rho \dot{e} - \boldsymbol{D}:\boldsymbol{\sigma} + \boldsymbol{v} \cdot (\rho \dot{\boldsymbol{v}} - \boldsymbol{\sigma} \cdot \nabla - \rho \boldsymbol{b})] dV = 0 \tag{3.13}$$

Now, the last term in the integral can be noted to be equal to the result obtained from the conservation of momentum equation. Substituting in the equality from conservation of momentum (3.9) and invoking the arbitrariness of the domain gives the final conservation of energy governing equation. (3.14) This expression essentially governs the stress state within a particle and will be used later in Section 3.5.2 to determine the pressure in each material point using an equation of state.

$$\rho \dot{e} = \boldsymbol{D}:\boldsymbol{\sigma} \tag{3.14}$$

3.2 Weak Formulation

In the previous section, the governing equations for a deforming continuum body were described as essentially a set of PDEs. This section now focuses on briefly describing the weighted residual method used in numerically solving the weak form of these PDEs. To begin with, the weighted residual method introduces an arbitrary virtual displacement δu_j to the strong form conservation of momentum equation (3.8). A similar process is applied to the traction boundary condition given by (3.16) which essentially states that the traction boundary force must equal the boundary stress in the body. This produces a weak form which in tensor index notation, can be written for momentum (3.8) and boundary conditions respectively as:

$$\int_{\Omega} \delta u_i (\sigma_{ij,j} + \rho b_i - \rho \ddot{u}_i) dV = 0 \tag{3.15}$$

$$\int_{\Gamma_t} \delta u_i (\sigma_{ij} n_j - \bar{t}_i) dV = 0 \tag{3.16}$$

where the new term $\bar{t}_i = n_j\sigma_{ij}|_{\Gamma_t}$ is the traction force and Γ_t is the traction boundary. The first term in Equation (3.15) can be rewritten using integration by parts, divergence theorem and (3.16) to yield

$$\int_\Omega \delta u_i \sigma_{ij,j} dV = \int_\Omega \left[\left(\delta u_i \sigma_{ij}\right)_{,j} - \delta u_{i,j}\sigma_{ij}\right] dV \tag{3.17a}$$

$$= \int_\Gamma \delta u_i \sigma_{ij} n_j dA - \int_\Omega \delta u_{i,j}\sigma_{ij} dV \tag{3.17b}$$

$$= \int_{\Gamma_t} \delta u_i \bar{t}_i dA - \int_\Omega \delta u_{i,j}\sigma_{ij} dV \tag{3.17c}$$

Substituting (3.17) into (3.15) and multiplying by -1 yields the following virtual work equation:

$$\int_\Omega \rho \ddot{u}_i \delta u_i dV + \int_\Omega \sigma_{ij}\delta u_{i,j} dV - \int_\Omega \rho b_i \delta u_i dV - \int_{\Gamma_t} \delta u_i \bar{t}_i dA = 0 \tag{3.18}$$

Alternatively, the terms in Equation (3.18) can be separated into internal, external and inertial work components respectively. This leads to what is known as the virtual equation shown below

$$\delta w = \delta w^{int} - \delta w^{ext} + \delta w^{kin} = 0 \tag{3.19a}$$

where

$$\delta w^{int} = \int_\Omega \sigma_{ij}\delta u_{i,j} dV \tag{3.19b}$$

$$\delta w^{ext} = \int_\Omega \rho b_i \delta u_i dV + \int_{\Gamma_t} \delta u_i \bar{t}_i dA \tag{3.19c}$$

$$\delta w^{kin} = \int_\Omega \rho \ddot{u}_i \delta u_i dV \tag{3.19d}$$

These equations serve as the basis for the formulation of a numerical solution presented in the following sections.

3.3 MPM Description

The Material Point Method (MPM) [32] is implemented in this thesis and is a particle method designed to incorporate the advantages of both Lagrangian and Eulerian methods. Similar to the SPH method [36], bodies are discretized into a finite number of material points each of which carry the stresses, strains, energy, momentum and all other thermomechanical properties. Again, by discretizing the bodies into point particles rather than elements, the Lagrangian issue of mesh distortion and element entanglement is avoided while the focus on points within the material is maintained. Furthermore, by solving the constitutive equations at the material points and having them carry all information, the issue of numerical dissipation due to the transfer of information between material and grid in Eulerian methods is eliminated [32]. What separates MPM from SPH is how interpolations are carried out. Rather than a SPH kernel function describing how the value of a property at a particle diffuses into its surrounding volume, a computational grid and shape functions identical to mesh-based FEM are utilized. Boundary conditions can be easily enforced directly on the necessary nodes of the computational grid. Previous work by Raymond et al. [37] has introduced methods which couple the MPM and SPH however this has not been implemented in the current thesis as it has not been shown to specifically improve performance in CS modeling.

Constitutive equations are solved at the material points, which essentially serve as integration points, while the computational grid is employed only to determine gradient and divergence terms in solving for the forces and momentums. This grid is typically composed of hexahedron elements which collect data from material points within it to its grid nodes. Then, total forces and momentums at grid nodes are calculated based on values at the material points and integrated to determine nodal displacements and velocities. These nodal displacements and velocities are then mapped back to the material points to update particle displacements and velocities as well as particle strain and vorticity increments. After all this, the grid is reset to its initial position at the end of each time step while particles remain in their deformed position along with their updated stress, momentum and other properties. The solution on the new grid can be reconstructed at the beginning of the next time step, thus eliminating the convection term in Eulerian formulations [32]. Figure 3.2 shows a schematic representation of the MPM algorithm describing the major steps in the MPM algorithm.

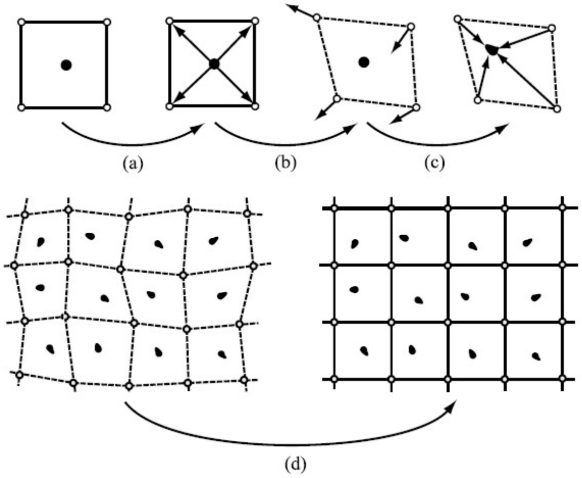

Figure 3.2: Schematic representation of the MPM algorithm showing a) mapping of particle mass and momentum to nodes, b) calculation of new nodal forces and momentums etc., c) updating of particle velocity and position with nodal values, d) storage of all material properties in particles and resetting of grid [32].

By the MPM formulation, several advantages exist over SPH and other meshfree methods. Firstly, MPM does not require the computationally expensive neighbor search required in meshfree methods. Rather, with its use of a computational grid, MPM is able to avoid tensile instability and other inconsistencies present in meshless methods like SPH. The standard shape functions used in mesh-based FEM given by (2.1) are used again in the original MPM implemented in this thesis. Again, this is given by (3.20),

$$N_{Ip}(\xi,\eta,\zeta) = \frac{1}{8}(1+\xi_I\xi)(1+\eta_I\eta)(1+\zeta_I\zeta) \tag{3.20}$$

where ξ, η and ζ are the natural coordinates of a particle p and ξ_I, η_I and ζ_I are the natural coordinates of the specific node I of the grid element, which are always either +1 or -1 by definition. Similar to in mesh-based FEM, these shape functions serve to map any nodal value or the gradient of said value to a material point and vice versa. Equation (3.21) and (3.22) describes how this can be done using displacement and displacement gradient as an example.

$$\delta u_{ip} = N_{Ip}\delta u_{iI} \tag{3.21}$$

$$\delta u_{ip,j} = N_{Ip,j}\delta u_{iI} \tag{3.22}$$

Note that only the original MPM implementation is considered in this thesis, where the use of the linear shape function in (3.20) results in a discontinuous shape function gradient. As a result, numerical issues will exist if a particle happens to lie directly on the boundary between cells as it will have an undefined shape function gradient. This is commonly known as cell crossing noise which may result in unsatisfactory and unphysical results [32]. Techniques have been developed over the years to modify the original MPM such as the Generalized Interpolation Material Point (GIMP) method by Bardenhagen et al. [66], which essentially smoothens the linear shape functions by taking the convolution of (3.20) with a characteristic particle function. Various forms of the GIMP method are able to largely alleviate or eliminate the effects of cell crossing noise, however these have been left as part of future work in overall improvements to the MPM implementation.

3.4 Numerical Implementation

The explicit scheme numerical implementation of the MPM has been developed by Zhang et al. [32], and serves as the basis which the current MPM code is developed upon. A Modified Update-Stress-Last (MUSL) scheme is used as it leads to more stability when a grid node is only related to a single particle. Schemes that update stress last (i.e. at the end of a time step) have also been shown by numerical studies to damp out unresolved modes [67]. Figure 3.3 presents a flow chart of the steps in the MUSL MPM scheme with contact considerations in comparison to traditional, mesh-based FEMs.

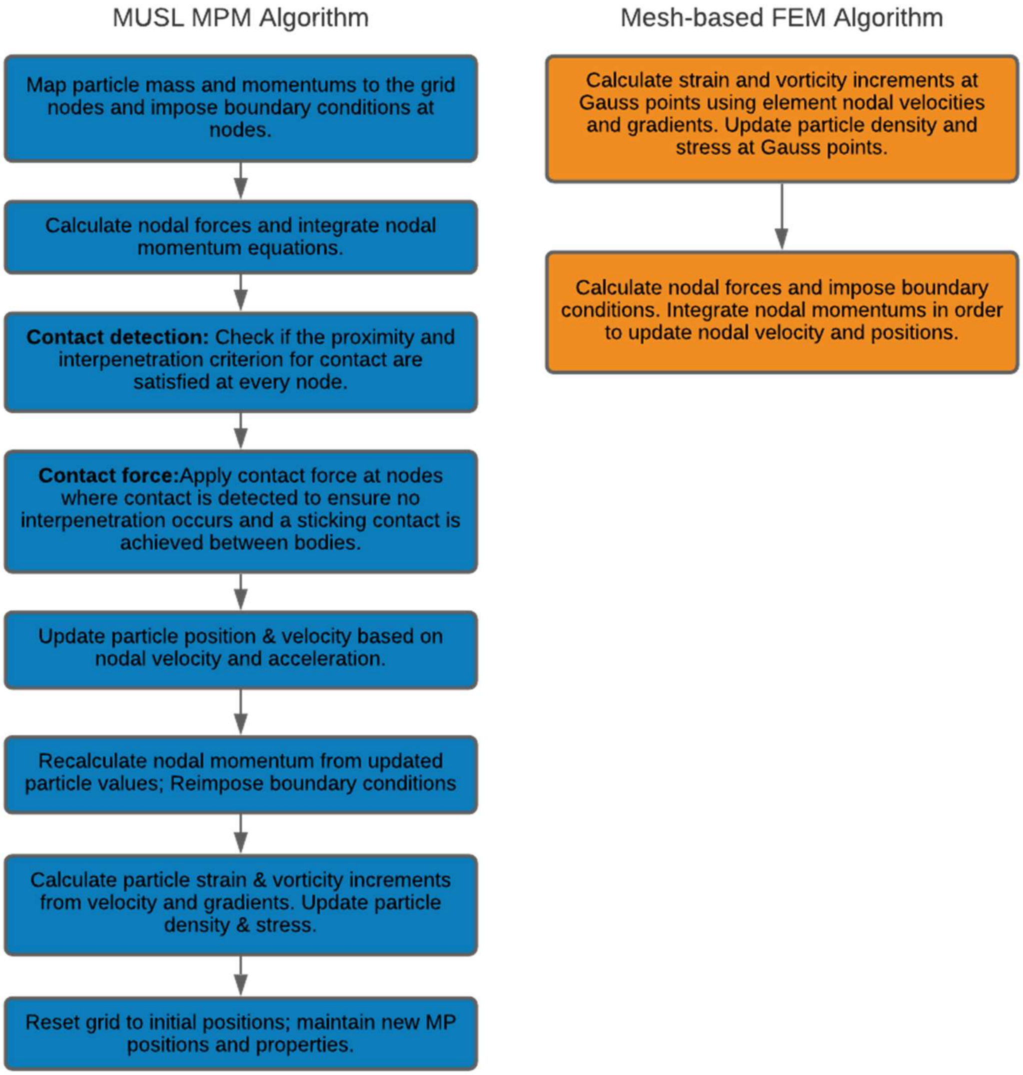

Figure 3.3: Flow chart of the MUSL MPM algorithm with contact considerations compared with traditional FEMs.

The numerical implementation of the MPM algorithm using a central difference method explicit integration is described in detail by the following steps:

1. At the beginning of each time step, shape functions (N_{Ip}^k) identical to those used in traditional FEM shown in Equation (3.20) are used to map initial values for mass and momentum from the particles to the computational grid (Figure 3.2a).

$$m_I^k = \sum_{p=1}^{n_p} m_p N_{Ip}^k \tag{3.23}$$

$$\rho_{iI}^{k-1/2} = \sum_{p=1}^{n_p} m_p v_{ip}^{k-1/2} N_{Ip}^k \tag{3.24}$$

where ρ_i is the momentum and v_i is the velocity of the material point p. Note that to match notation from Zhang et al. [32], ρ_i indicates momentum while ρ indicates density. The meaning of the subscripts and superscripts are as follows:

- Subscript *I* refers to a grid node *I*.
- Subscript p refers to a material point p.
- Subscript *i* refers to coordinate direction.
- Superscript *k* refers to time step number.

Essential boundary conditions can be easily applied to specific grid nodes by explicitly setting the momentum of the desired grid node along a direction to a desired value.

2. Internal forces are calculated using stress values from the previous time step and combined with external forces to produce the total inertial force applied at a grid node. The nodal acceleration can then be calculated from the inertial force and integrated to find velocity and position. Nevertheless, these equations are derived from the virtual work equation (3.19) described in Section 3.3. In essence, the virtual displacement terms δu_i at the grid nodes are numerically approximated as functions of N_i and virtual displacements at the material points. Since the virtual displacements themselves can be of arbitrary value, work/energy terms can be written in terms of force. These force equations must still be equal to the volume/surface integrals within the Equation (3.19), which numerically can be represented using shape functions as follows:

$$f_{iI}^{int,k} = -\sum_{p=1}^{n_p} N_{ip,j}^k \sigma_{ijp} \left(\frac{m_p}{\rho_p}\right) \tag{3.25}$$

$$f_{iI}^{ext,k} = \sum_{p=1}^{n_p} m_p N_{Ip}^k b_{ip}^k + \sum_{p=1}^{n_p} N_{Ip}^k \bar{t}_{ip}^k h^{-1} \left(\frac{m_p}{\rho_p}\right) \tag{3.26}$$

$$f_{iI}^k = f_{iI}^{int,k} + f_{iI}^{ext,k} \tag{3.27}$$

Additional variables and notation introduced are as follows:

- $N_{ip,j}^k$ refers to the derivative of the shape function value at particle p w.r.t. a coordinate direction j at time step *k*.
- σ_{ijp} refers to the Cauchy stress tensor of a particle p.
- b_{ip}^k refers to the body force at time step *k*.
- $\bar{t}_{ip}^k$ refers to the traction force at time step *k*.

An additional term h is also present in $f_{iI}^{ext,k}$ which refers to the thickness of a fictitious layer used to convert the surface integral described by the traction force summation to a volume integral. Since no traction forces are considered as part of the simulation, this term is not actually defined and may be ignored.

3. Grid nodal momentums are then calculated by explicitly integrating the inertial force at each node using the central difference method as shown by Equation (3.28).

$$\rho_{iI}^{k+1/2} = \rho_{iI}^{k-1/2} + f_{iI}^{k}\Delta t^{k} \tag{3.28}$$

4. **Contact detection:** A basic contact algorithm is implemented within the current thesis which detects contact through the nodal velocities calculated from the newly determined nodal momentums. If particles from body *m* and body *s* are both near the same grid node such that mass from both are detected on that grid node and are approaching each other as dictated by their momentums shown in Equation (3.29), then the bodies may interpenetrate within the current time step. Note that the opposite of this expression may be used to evaluate if bodies are separating as opposed to impacting as well, which will be useful later in determining when to apply bonding effects.

$$\left(m_I^{s,k}\bar{\rho}_{iI}^{m,k+1/2} - m_I^{m,k}\bar{\rho}_{iI}^{r,k+1/2}\right)\hat{n}_{iI}^{m} > 0 \tag{3.29}$$

$\hat{n}_{iI}^{m}$ refers to the components of the unit normal vector of body *m* at grid node *I*. The most simple way to calculate this vector is by using the mass gradients as shown in Equation (3.30).

$$\hat{n}_{iI}^{m} = \frac{\sum_{p=1}^{n_p^m} m_p N_{Ip,i}}{\left|\sum_{p=1}^{n_p^m} m_p N_{Ip,i}\right|} \tag{3.30}$$

There are more complex methods of contact detection where the above velocity criterion is combined with a separation criterion to improve accuracy but these are not considered within this thesis [68]. Further discussion on the challenges in identifying the most accurate normal vector in MPM is provided in section 3.5.4. Figure 3.4 provides a schematic representation of a grid node *I* in 2D that would detect imminent contact if the material points in a body *r* and body *s* within its region of influence are approaching node I.

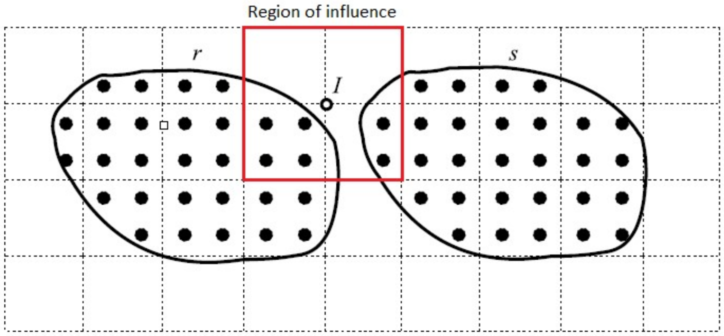

Figure 3.4: Contact detection schematic, showing the region of influence of a contact node [32].

5. **Contact force:** If contact is detected to be imminent at a grid node, it is necessary for that grid node to apply an equal and opposite contact force onto each body to prevent interpenetration. For a sticking contact condition, the grid nodal velocity for each body must be exactly equal (i.e. the particles in both bodies must have a relative velocity of 0

when mapped to grid node *I*). Using this certainty, the sticking contact force at grid node *I* can be calculated as follows:

$$f_{iI}^{m,c,k} = \frac{1}{\left(m_I^{m,k} + m_I^{s,k}\right)\Delta t^k}\left(m_I^{m,k}\rho_{iI}^{s,k+1/2} - m_I^{s,k}\rho_{iI}^{m,k+1/2}\right) \tag{3.31}$$

This sticking condition contact force can be separated into normal and tangential components, with the tangential component being subjected to change if slipping occurs. In the present thesis, only a frictionless contact condition is considered therefore $f_{iI}^{m,c,k}$ is never subject to change as a result of Coulomb's stick-slip law.

6. Nodal momentums are adjusted with the calculated contact force in identical fashion to in Step 3. These nodal force and momentum calculations constitute step b) in Figure 3.2.
7. Particle velocity and position are updated using the eight updated nodal momentums of the grid each particle is currently within. This can be done using Equation (3.32) shown below and corresponds to step c) in Figure 3.2.

$$v_{ip}^{k+1/2} = v_{ip}^{k-1/2} + \sum_{I=1}^{8} \frac{f_{iI}^k N_{Ip}^k}{m_I^k}\Delta t^k \tag{3.32a}$$

$$x_{ip}^{k+1} = x_{ip}^k + \sum_{I=1}^{8} \frac{\rho_{iI}^{k+1/2} N_{Ip}^k}{m_I^k}\Delta t^{k+1/2} \tag{3.32b}$$

8. As part of the MUSL scheme, an additional step is required where grid nodal momentums are recalculated based on the updated particle velocity from step 7, with essential boundary conditions imposed. As previously mentioned, the essential boundary conditions can be imposed by simply setting the appropriate nodal momentums to a desired value.

$$\rho_{iI}^{k+1/2} = \sum_{p=1}^{n_p} m_p v_{ip}^{k+1/2} N_{Ip}^k \tag{3.33}$$

9. Nodal velocities are recalculated from the updated nodal momentums by simply dividing the nodal momentum by the nodal mass.

$$v_{iI}^{k+1/2} = \frac{\rho_{iI}^{k+1/2}}{m_I^k} \tag{3.34}$$

10. These updated nodal velocities are then used to calculate strain and vorticity increments of each particle for a given time step using the symmetric and skew-symmetric components of the velocity gradient, similar to in mesh-based FEMs.

$$\Delta D_{ijp}^{k+1/2} = \frac{1}{2}\left(N_{Ip,j}^k v_{iI}^{k+1/2} + N_{Ip,j}^k v_{jI}^{k+1/2}\right)\Delta t^{k+1/2} \tag{3.35a}$$

$$\Delta W_{ijp}^{k+1/2} = \frac{1}{2}\left(N_{Ip,j}^k v_{iI}^{k+1/2} - N_{Ip,j}^k v_{jI}^{k+1/2}\right)\Delta t^{k+1/2} \tag{3.35b}$$

Particle densities are also now updated using the hydrostatic strain components with:

$$\rho_p^{k+1} = \frac{\rho_p^k}{1 + \Delta\varepsilon_{iip}^{k+1/2}} \tag{3.36}$$

11. These strain and vorticity increments are then used within the PTW model to update the stress state of each particle for use in the next time step. A description of the stress update algorithm can be found in Appendix A.
12. The grid is reset to its initial positions at the end of each time step while material points maintain their updated positions, velocities and other properties. This corresponds to part d) in Figure 3.2.

With MPM, boundary conditions at fixed boundaries can be imposed by setting the appropriate nodal momentums to 0. The time step size used for the explicit integration is required to be small enough to satisfy a stability requirement. In traditional FEM, this time step is defined by

$$\Delta t_{cr} = \min_{e} \frac{l^e}{c} \tag{3.37}$$

where l^e is the characteristic length of element e and $c = \sqrt{\frac{E(1-\nu)}{(1+\nu)(1-2\nu)\rho}}$ for an assumed linearly elastic material. In the actual implementation, it was deemed necessary through initial testing to impose an additional requirement setting the time step size to a small fraction of Δt_{cr} such as 5% for stability. Further details on convergence testing will be presented in Section 4.2 and an ideal time step size will be identified through explicit testing in Section 5.1.4. It is also important to note that all material properties are stored within the material points, thus allowing the grid to be able to be reset at the end of each time step. By doing so, the MPM is able to avoid the mesh distortion problems typically seen for large-deformation simulations using Lagrangian FEM and eliminate convection terms in Eulerian FEM.

Similar to mesh-based methods, an important criterion in MPM is the relationship between grid size and particle spacing (i.e. the distance between two material points). The grid configurations will be referred to by the format DCell/dp where DCell refers to the length in µm of the grid dimension and dp refers to the material point spacing, also in µm. A well-known source of divergence in MPM is the number of material points per computational grid. Sinaie et al. [69] has been shown that although grid refinement does have the highest influence on accuracy, the number of material points or particles in the test also plays a significant role. As a result, any refinement of the grid size also requires a similar refinement in particle spacing to maintain a sufficient/similar number of particles per grid. The error between predicted initial stiffness in simulations by Sinaie et al. [69] and experimental values can be over 150% if there are insufficient material points per grid.

Finally, to note in two-body contact problems, one grid must be used for each body within the simulation to store values pertinent to contact such as normal vectors and momentums from particles in each separate body. Although this does increase the computational cost of the algorithm, it remains a necessary step to distinguish between bodies and incorporate the contact algorithm within MPM. In order to reduce this cost, the method proposed by Ma et al. [70] is utilized where the multi-mesh is only employed at nodes where there is contact, as shown in

Figure 3.5. Since each grid is identical and kept as such due to the reset at the end of every time step, contact nodes can be easily identified as the same one in each grid.

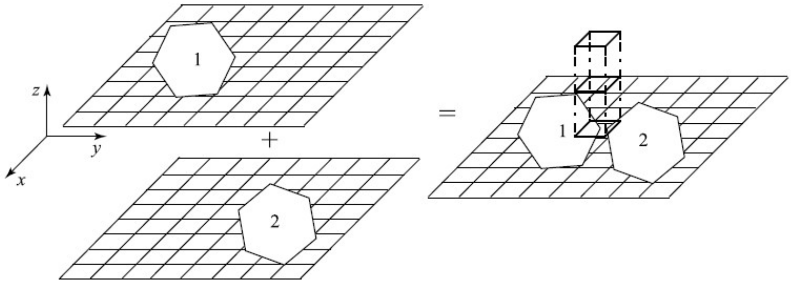

Figure 3.5: Multi-mesh method applied only at contact nodes introduced by Ma et al. [70].

3.5 Numerical Considerations

3.5.1 Strength Model

As was previously described in Chapter 2, an appropriate constitutive model is essential in order to generate an accurate finite element simulation. Historically, the JC model has been the most widely implemented constitutive model in simulating CS [8, 28, 43, 16, 35, 34, 11, 44, 45]. This model is suitable for modeling of most processes but is noticeably lacking when modeling process with large strain and particularly high strain rates as is observed in CS particle impacts. Instead, the PTW model has components that are specifically tailored to modeling plastic deformation in the overdriven shock regime (strain-rates above $10^7 s^{-1}$). In a study by Banerjee et al. [47] comparing five constitutive models including JC and PTW, it was determined that the PTW model performed the best overall being very accurate for both high ($\geq 100\ s^{-1}$) and low strain rates ($\leq 100\ s^{-1}$) and is valid for the greatest strain rate range. The PTW model clearly stood out against other models as it showed the lowest overall error compared to experimental data in flow stress prediction as shown in Table 3.1.

Table 3.1: Average error from maximum absolute (MA) errors in yield stress for five flow stress models under various conditions [47].

Condition	Average MA Error (%)				
	JC	SCGL	ZA	MTS	PTW
All Tests	36	64	33	23	17
Tension Tests	25	20	19	14	18
Compression Tests	45	126	50	35	10
High Strain Rate (≥ 100 /s)	29	22	20	15	18
Low Strain Rate (< 100 /s)	45	219	76	49	5
High Temperature (≥ 800 K)	43	90	40	27	16
Low Temperature (< 800 K)	20	20	17	15	14

As it can be seen, percent error in both tension and compression are both low which is unique among the tested models. Simulations in the overdriven shock regime were not specifically tested by Banerjee et al. [47], however the model does explicitly account for rapid increases in yield stress at strain rates above $1000\ s^{-1}$. Recalibration of certain model material parameters for processes with strains in the overdriven shock regime may be required to improve prediction accuracy of CoR as shown by Razavipour and Jodoin [50]. Nevertheless, the overall results obtained by Banerjee are also supported by numerical studies from Rahmati and Ghaei [45] and Cormier et al. [71], specifically for its advantages and improvements over the JC and other models at the extreme strain rates seen in the CS process. Although these studies have utilized a constitutive model which considers CS-specific parameters, they have been implemented within ABAQUS/Explicit using mesh-based methods which are not ideal for CS conditions.

Using an alternate strength model will have a strong influence on the performance of any direct bonding model as well. Aside from the work by Rahmati and colleagues [45, 49], all previous bonding models as mentioned in Chapter 2.4 made use of the JC strength model which as previously mentioned is not suitable for CS conditions. The use of an appropriate strength model for CS conditions such as the PTW model is critical to achieving accurate bonding model performance. Although the PTW model has also been previously implemented in ABAQUS/Explicit [45, 49], it has never been implemented within an MPM framework to the best of the authors knowledge. Consequently, this thesis seeks to address this knowledge gap and use the implementation of a modified PTW strength model to develop a direct bonding model using the MPM.

3.5.2 Equation of State

In order to determine the internal energy and subsequently, the pressure within each material point, the linear Mie-Grüneisen equation of state is utilized. The following equations have been derived in detail by Zhang et al. [32], but are summarized here. From the energy conservation expression (3.14) in Section 3.1.3, the rate of internal energy per initial volume $\dot{E}$ can be written for isothermal cases as

$$\rho\dot{e} = \boldsymbol{D}:\boldsymbol{\sigma} = \dot{E} = J\boldsymbol{D}:\boldsymbol{s} - Jptr(\dot{\boldsymbol{\varepsilon}}) \tag{3.38}$$

where J is the Jacobian determinant, $\boldsymbol{D}$ is the deformation tensor, $\boldsymbol{s}$ is the deviatoric stress tensor, p is the pressure and $\dot{\boldsymbol{\varepsilon}}$ is the total strain rate. Then, the following equation for the internal energy at the next step e^{n+1} can be derived through numerical integration using values at t^n and $t^{n+1/2}$.

$$\begin{aligned} e^{n+1} &= e^n + V_0\dot{E}^{n+1/2}\Delta t \\ &= e^n + V^{n+1/2}\boldsymbol{s}^{n+1/2}:\Delta\boldsymbol{\varepsilon}^{n+1/2} - V^{n+1/2}p^{n+1/2}\Delta\varepsilon_v^{n+1/2} \end{aligned} \tag{3.39}$$

The second line in (3.39) has taken advantage of the fact that $V = JV_0$ and that $tr(\dot{\boldsymbol{\varepsilon}})\Delta t = \sum_{i=1}^{3}\Delta\varepsilon_{ii} = \Delta\varepsilon_v^{n+1/2}$ is the volumetric strain increment. This means that $V^{n+1/2}\Delta\varepsilon_v^{n+1/2} = V^{n+1} - V^n = \Delta V$. Any value at time step $t^{n+1/2}$ is calculated as the average of its value at time step t^n and t^{n+1}. With this, (3.39) can be rewritten as

$$e^{n+1} = e^{*n+1} - \frac{1}{2}\Delta V p^{n+1} \tag{3.40}$$

where p^{n+1} is the pressure and e^{*n+1} the trial specific internal energy at t^{n+1} defined as follows:

$$e^{*n+1} = e^n + V^{n+1/2}\boldsymbol{s}^{n+1/2}:\Delta\boldsymbol{\varepsilon}^{n+1/2} - \frac{1}{2}\Delta V p^n \tag{3.41}$$

Converting the internal energy e^{n+1} to the internal energy per initial volume $E^{n+1} = e^{n+1}/V_0$, the pressure at t^{n+1} can be found by assuming a linear equation of state using Equation (3.42):

$$p^{n+1} = A^{n+1} + B^{n+1}E^{n+1} \tag{3.42}$$

where A^{n+1} and B^{n+1} are material-specific constants. These constants are functions of material properties and can be defined in a variety of ways. In this research, the well-known Mie-Grüneisen equation of state will be used in determining A^{n+1} and B^{n+1}. For brevity, the formulation of these constants is not described here but can be found as Equation (6.180) in Section 6.3.5 of the textbook by Zhang et al. [32]. Substituting (3.40) and (3.41) into (3.42), p^{n+1} can be found as follows:

$$p^{n+1} = \frac{A^{n+1} + B^{n+1}E^{*n+1}}{1 + \frac{1}{2}B^{n+1}\left(\frac{\Delta V}{V_0}\right)} \tag{3.43}$$

By Equations (3.40) and (3.43), the internal energy and pressure for each subsequent time step can be found and used to calculate future values.

3.5.3 Adiabatic Heating

Although the powder feedstock material is considered to be at room temperature initially, in spite of its namesake, CS particles still experience a noticeable temperature change that must be considered in numerical modeling. Although it is difficult to measure particle temperature experimentally, Nastic and Jodoin [72] have reported 15-µm copper particle temperatures of 44, 77 and 99°C at the nozzle exit with a gas stagnation temperature of 200, 400 and 500°C, respectively. Particle temperatures upon impact have been shown by Manap et al. [34] within an SPH framework to reach up to 450°C locally for Al on Al impacts. Experimental data from Al7075 on AZ31B impacts have validated this as temperatures as high as 330°C have been recorded [21]. Changes to gas stagnation or particle temperature is not examined within the numerical simulation and the particle is simply assumed to be initially at room temperature. However, significant particle heating must still be expected and is calculated assuming adiabatic heating, which has proven reasonable in a number of other fundamental studies [28, 8]. Material temperature is updated as a function of plastic work and using a standard constant Taylor-Quinney coefficient of 0.9 [73]. In essence, this assumes that 90% of the plastic work calculated during each time step is converted to heat. Equation (3.44) presents the temperature increment as a function of plastic strain increment and specific heat C_p within a time step.

$$\Delta T = \frac{\chi\sigma_y}{\rho C_p}\Delta\varepsilon_p \tag{3.44}$$

Nevertheless, it should be noted that the precise implications of temperature on the simulation output does not lie with only the particle temperature but rather the ratio between particle temperature, a reference and melting temperature. The reference temperature is a constant however melt temperature is updated using the SCG melt model, based on a Mie-Grüneisen material constant and previously presented in Section 2.4.2.

3.5.4 Normal Vector Calculation

An additional variable that has not been explicitly addressed is the direction of the contact/bonding force. The MPM contact algorithm is severely affected by variations in the definition of a normal vector and it affects both contact and bonding forces. Due to the magnitude of contact forces required to prevent interpenetration of such high velocity impacts, a different normal definition will lead to effects which propagate throughout the simulation to drastically affect the final result. Normal vectors in a basic MPM implementation for a body b at grid node I is calculated using the mass gradients as shown in (3.30). Note that in the current thesis, only a single material system is considered thus the mass gradient suffices. If multiple materials are to be considered simultaneously, it is recommended that the normals be calculated through the volume gradient instead to account for different material densities [74].

Since the calculated normals from each body are generally not perfectly aligned, either one of the normal vectors $\hat{n}_{iI}^{b}$ or a function of the two may be selected as the contact normal (n_{iI}). Typically, the normal from the stiffer body should be selected but in the present case of identical materials, the normal from the body with the larger mass gradient is selected. For simplicity, it is assumed that the body with the larger mass also has the larger mass gradient and more accurate normal vector, particularly near edge nodes as shown in Figure 3.6. This method is known as the Maximum Volume Gradient (MVG) technique which selects the normal of the body with the greatest volume gradient, or the greatest mass gradient single material systems. This has shown good performance so long as material stiffnesses are not too high [74].

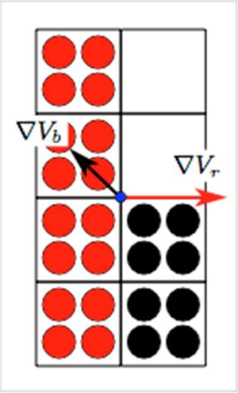

Figure 3.6: Schematic showing the improved accuracy of using the normal vector of the larger volume body r, particularly around edge nodes [75].

Overall, the choice and calculation of normal vectors is a known source of error in MPM, with numerous techniques having been developed to minimize error for certain scenarios. For simplicity, the MVG is used here which sets the normal vector of the substrate ($\hat{n}_{iI}^{m}$) as the contact normal in all tests within this thesis ($n_{iI} = \hat{n}_{iI}^{m}$). The logic is that the substrate which has the much larger mass and mass gradients is more likely to be closer to the physical contact interface and more accurate [74]. Conceptually, it is reasonable to assume smaller volume bodies like the powder particle are less likely to have the more accurate volume/mass gradients. An equal and opposite force is applied by the particle on the substrate along the $-\hat{n}_{iI}^{m}$ direction to adhere to conservation laws. The collinearity condition is explicitly enforced to ensure conservation of momentum by setting the nodal normal value associated with the particle body to $\hat{n}_{iI}^{s} = -\hat{n}_{iI}^{m}$ [32, 74].

As a final note on normal vector calculations, it is known that the MPM contact and interface calculations can be very accurate provided an accurate normal vector is available [76]. Aside from MVG, there exists several other commonly used methods for normal vector identification as well as filtering techniques to address edge node issues. Unfortunately, the most accurate method depends on the problem and in particular, may vary with the location and orientation of the contact interface relative to the computational grid [74]. With these factors in mind, it is easy to see that identifying the best normal vector technique for modeling of CS can be challenging, particularly with the large deformations and material ejection or numerical fracture observed in the current application. Considering and comparing the performance different mathematical and machine learning techniques for identifying the most accurate normal vector definition is a topic of ongoing research [68]. Overall, this lies outside the scope of the current thesis but suffice to say, additional testing will be required to calibrate and evaluate the model in the future, if an improved normal vector definition is to be considered.

3.5.5 Infinite/Semi-infinite Media

Another factor that must be considered is the numerical modeling of an infinite or semi-infinite media, such as the particle-substrate system in CS. In order to have good particle resolution within the particle, it is not feasible to discretize the full system without high computational costs. As such, the viscous damping boundary method as described by Ross, has been developed to have a finite media behave in similar fashion to an infinite media. Within this method, stresses are applied by fictitious viscous dampers to boundaries based on the primary and secondary wave velocities of the material [77]. These velocities are defined by standard material properties given as Equation (3.45).

$$V_p = \sqrt{\frac{(1-\nu)E}{(1-2\nu)(1+\nu)\rho}} \tag{3.45a}$$

$$V_s = \sqrt{\frac{E}{2(1+\nu)\rho}} \tag{3.45b}$$

For a given boundary in 3D cartesian coordinate system, the primary direction considered by the dampers is the direction perpendicular to the boundary while the secondary direction are the remaining orthogonal directions. Figure 3.7 provides a schematic of the viscous damping boundary concept where z is the primary wave direction and x and y are the secondary wave directions.

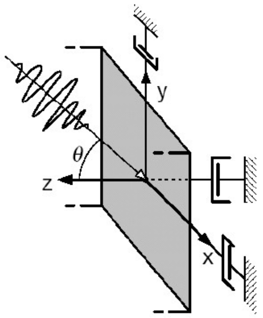

Figure 3.7: Viscous damping boundary schematic, showing primary (z) and secondary wave (x and y) directions [77].

The damping coefficient of the fictitious dampers can be calculated from these wave velocities as follows:

$$c_{ii} = \int_{\Gamma} a\rho V_p d\Gamma \quad Primary\ wave, z - direction \tag{3.46a}$$

$$c_{ii} = \int_{\Gamma} a\rho V_p d\Gamma \quad Secondary\ wave, x\ or\ y\ direction \tag{3.46b}$$

where Γ is the surface area of the element. The a and b terms are dimensionless parameters which for small incident angles (θ < 30º) can be set to one [78]. Numerically, the grid nodes containing surface particles of the cylinder substrate will be subjected to an additional internal damping force defined by the product of the damping coefficient, particle velocity and particle volume. To note is that only surface particles on the bottom and circumferential boundaries are considered and the top surface is left unaffected. In the case of the bottom boundary, there will be one primary (z) and two secondary (x, y) wave directions while the circumferential boundaries will have two primary (x, y) and one secondary (z) directions.

Chapter 4 Direct Bonding Model

From the literature review, all research into impact-induced bonding in the CS process clearly point toward the existence of an intimate relationship between material jetting and bonding. As previously described, the precise physical phenomenon behind jet formation is still a subject of debate with initial theories attributing jetting to adiabatic shear instability but more recent literature suggesting it is as a result of a hydrodynamic spall process. The purpose of this thesis is not to identify which elastoplastic-dynamic process is correct. Instead, the goal is to represent bonding effects on material behavior directly within a simulation and accurately predict critical velocity and bond strength. In order to specifically tailor the MPM to CS conditions, the basic FE equations are solved with the PTW strength model, SCG melt model, viscous damping boundaries, linear Mie- Grüneisen equation of state and MVG normal vector definition.

4.1 Strain-based Bonding Model

4.1.1 Model Formulation

As an initial step towards a complete direct model of bonding, the aim is to first be able to predict bonding as a binary solution (bonded or rebounded) without any quantitative prediction of bond quality. The feedstock powder is assumed to always be at room temperature initially with friction and surface topology not considered in any simulation. Rahmati and Jodoin [49] have previously developed a strain-based cohesive zone model considering specifically the effects of oxide layers within an ALE framework. Their results showed good performance in predicting critical velocities and coefficients of restitution for Al, Cu and Ni particles impacting on same material substrates. This along with the relationship between jetting and bonding motivates the initial development of a strain-based bonding model within a MPM framework.

The following model formulation has been developed by Hirmand et al. [15] and will be utilized in this thesis work. It has been developed with the knowledge that there is a critical velocity required for bonding which corresponds to a specific set of process parameters. This suggests that successful bonding is likely also governed by a critical threshold value. Given the strong correlation between material jetting and bonding, the hypothesis is that this threshold value may be defined by the level of material jetting. From here, it is postulated that there exists within certain material points a time-discrete variable D_{bond}, called the *bonding parameter,* which defines whether bonding has either occurred or not. This bonding parameter is a history variable which serves to track the evolution of material jetting along the surface of each body and serves to define the threshold level of jetting required for bonding.

With this basis, two bodies B^1 and B^2 are considered which are externally bounded by surfaces ∂B^1 and ∂B^2 and come into contact. The contact interface can then be defined by the union of these two surfaces and denoted as $S = \partial B^1 \cap \partial B^2$. This bonding parameter D_{bond} is initialized to zero within each material point with $\dot{D}_{bond}(\boldsymbol{x}_p) \geq 0$ for $\boldsymbol{x}_p \in S$ and $\dot{D}_{bond}(\boldsymbol{x}_p) = 0$ otherwise. The key concept of the bonding model is in how $\dot{D}_{bond}(\boldsymbol{x}_p)$ is defined for impacting particles. Given the physical knowledge that material jetting manifests in large plastic strains occurring at extreme rates, it is sensible that $\dot{D}_{bond}(\boldsymbol{x}_p)$ is a function of these terms. An additional term which may be reasonable to consider is the amount of contact pressure and friction that must be exerted on the contact interface S for bonding to occur. The general evolution law for $D_{bond}(\boldsymbol{x}_p)$ is assumed to have functional relation with state variables given by

$$\dot{D}_{bond} = f\left(\varepsilon_n^p, \varepsilon_s^p, \dot{\varepsilon}_n^p, \dot{\varepsilon}_s^p, \boldsymbol{t_n}, \boldsymbol{t_s}\right) \tag{4.1}$$

where effective plastic strains (ε^p), strain rates (ε^p) and traction forces ($\boldsymbol{t}$) have been separated into normal and shear components.

Sufficient normal stress and strain have been shown in numerical studies to be critical for properly extruding material between the gaps in the oxide layer created by material jetting [49]. Experimental evidence from Wang et al. [54] has further shown that there is a spray angle below which bonding is compromised, indicating that a certain level of normal pressure/strain is required for impact-induced bonding. For simplicity, it is assumed that there is always sufficient normal contact pressure for successful bonding, given that only normal (90°) impacts will be considered. This allows D_{bond} to be purely a representation of the level of material jetting and subsequent oxide layer breakage/removal. As a result, the dependence of $\dot{D}_{bond}$ on normal and shear traction forces may be eliminated. Furthermore, by extension of this assumption, the normal components of strain and strain rate may also be ignored in the determination of $\dot{D}_{bond}(\boldsymbol{x}_p)$ as it can be presumed to be governed by the normal contact pressure threshold. In the end, the evolution of D_{bond} can be reduced to a function of the following variables:

$$\dot{D}_{bond} = f\left(\varepsilon_s^p, \dot{\varepsilon}_s^p\right) \tag{4.2}$$

where ε_s^p and $\dot{\varepsilon}_s^p$ refer to the shear component of effective plastic strain and plastic strain rate, respectively. Lastly, it is also deemed reasonable to assume lack of dependence on shear direction in the as the precise direction of shear strains should not affect the removal of oxide layers and subsequent bonding. This means that for the evolution of the D_{bond}, ε_s^p and $\dot{\varepsilon}_s^p$ can be simply taken as a magnitude rather than a vector.

Equation (4.2) can now serve as a basis for the development of an explicit form of $\dot{D}_{bond}(\boldsymbol{x})$. With this, the following can be written:

$$\dot{D}_{bond} = \frac{\left|\dot{\varepsilon}_s^p\right|}{\varepsilon_{bond}} \tag{4.3}$$

in which ε_{bond} is the effective bonding strain of a material which defines the threshold level of jetting required for bonding, given by

$$\varepsilon_{bond} = \varepsilon_c\left(1 - \ln\frac{\dot{\varepsilon}_s^p}{\dot{\varepsilon}_c}\right) \tag{4.4}$$

where ε_c and $\dot{\varepsilon}_c$ refer to the critical bonding strain and critical bonding strain rate. Intuitively, there is a distinct similarity between damage/fracture and bonding where bonding can in essence be viewed as a similar but opposite process to damage. As such, ε_{bond} in the proposed bonding model is loosely based on the form of the damage parameter in the Johnson-Cook (JC) dynamic failure model, in which fracture occurs once a critical strain is achieved [46].

Within a numerical integration framework, the evolution of $D_{bond}(\boldsymbol{x}_p)$ in a material point $\boldsymbol{x}_p$ can be described at time step n using a backward-Euler finite difference scheme as follows:

$$D_{bond}^{n+1}(\boldsymbol{x}_p) = D_{bond}^{n}(\boldsymbol{x}_p) + \dot{D}_{bond}^{n}(\boldsymbol{x}_p)\Delta t = D_{bond}^{n}(\boldsymbol{x}_p) + \frac{\Delta\varepsilon_s^p}{\varepsilon_{bond}} \tag{4.5}$$

where $\Delta\varepsilon_s^p = \left(\varepsilon_s^p\right)_{n+1} - \left(\varepsilon_s^p\right)_n$.

In order to directly include bonding phenomena in the numerical model, implementation of the bonding model is done as an extension of the contact algorithm. Originally, the contact algorithm can be distinguished by an impact and separation phase. During impact, a contact force is applied to prevent interbody penetration between points while no additional forces are applied if the points of each body are detected to be separating. As the bonding parameter $D_{bond}(\boldsymbol{x}_p)$ evolves within material points over time, they are also mapped to grid nodes like any other value in MPM. Since $D_{bond}(\boldsymbol{x}_p) > 0$ for $\boldsymbol{x}_p \in S$, it will only be non-zero at grid nodes where contact is detected. With a contact multi-mesh, the nodal $D_{bond}(\boldsymbol{I}_b)$ is calculated for node I each body b as the arithmetic average of the $D_{bond}(\boldsymbol{x}_p)$ of all surface particles within the volume of influence of node I in the multi-mesh of body b. Then, assuming that each body contributes equally to the bonding parameter evolution, the global nodal bonding parameter is then calculated as the average of the local $D_{bond}(\boldsymbol{I}_b)$ values from each body. Mathematically, for a two-body system this can be expressed within a time step as

$$D_{bond}(\boldsymbol{I}_b) = \frac{\sum_{p=1}^{n_{sp}^b} D_{bond}(\boldsymbol{x}_p)\, N_{ip}}{n_{sp}^b} \tag{4.6}$$

$$D_{bond}(\boldsymbol{I}_g) = \frac{D_{bond}(\mathbf{I}_1) + D_{bond}(\mathbf{I}_2)}{2} \tag{4.7}$$

where $D_{bond}(\boldsymbol{I}_b)$ is the bonding parameter value at node I of body b, n_{sp}^b is the number of surface particles on body b in the volume of influence of node I and $D_{bond}(\boldsymbol{I}_g)$ is the global bonding parameter at node I. Per this formulation, bonding effects are enforced by a grid node I on all material points within its volume of influence during the separation phase if $D_{bond}(\boldsymbol{I}_g) \geq 1$. This is done through applying an equal and opposite bond force to each body which is identical to the sticking contact force from the contact implementation. To recall, this contact force ensures a relative velocity of 0 between the contacting bodies which can be used to effectively model bond forces within a simulation. Thus, bond effects have been directly incorporated within the MPM simulation. Figure 4.1 presents how the proposed bonding model framework fits within the base MPM contact algorithm.

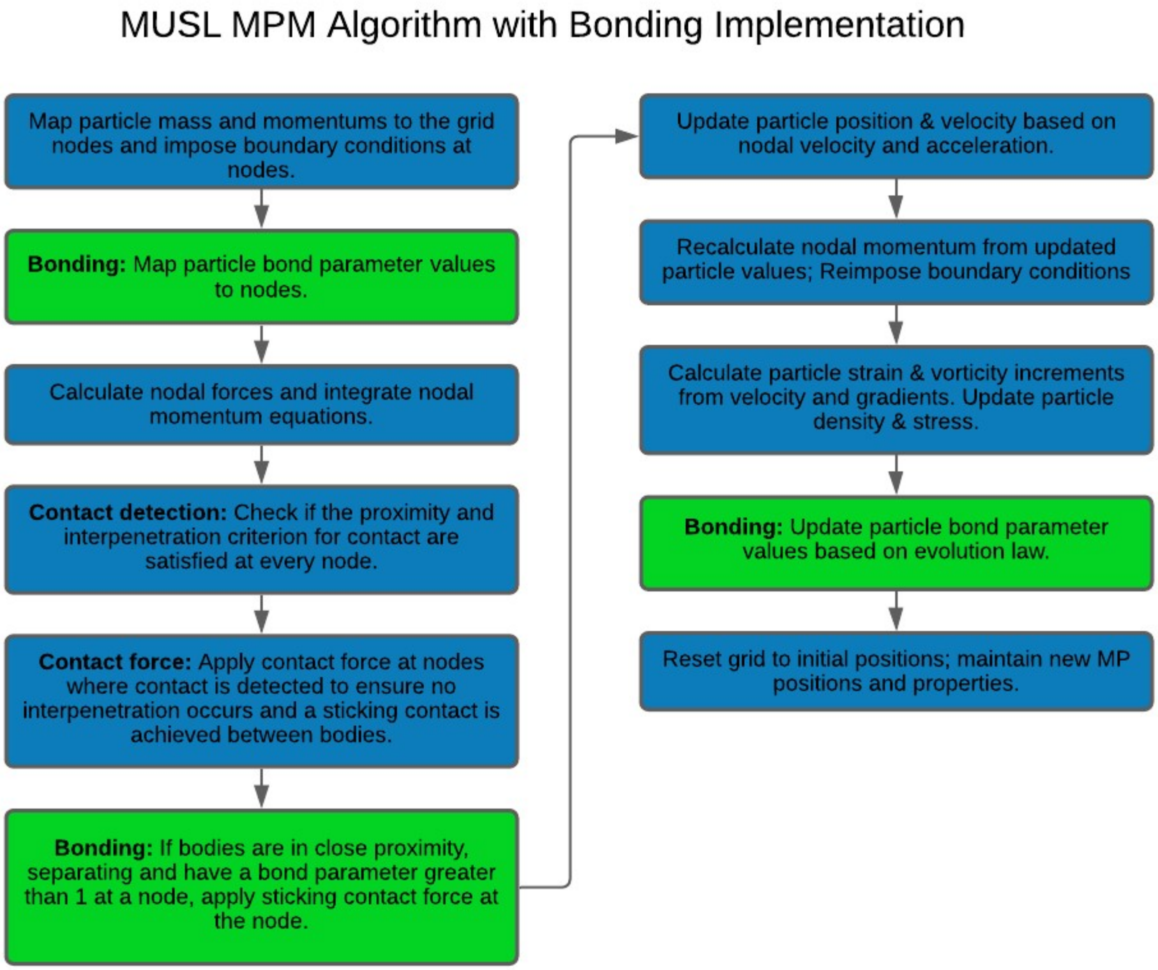

Figure 4.1: Flow chart of the MUSL MPM algorithm with contact considerations, updated with blocks in green showing how the bonding considerations are included.

4.1.2 Calibration Tests and Results

To limit computational costs, only a 1.0/0.35 grid configuration has been used in the initial testing of the strain-based bonding model calibration tests. Given the availability of existing experimental data, an Al/Al system with an aluminum particle sprayed onto an aluminum substrate will be modeled. A smaller spherical particle with a diameter of 14-μm and larger 30-μm diameter particle are impacted at their critical velocities of 810 and 770 m/s determined from experiments on a same material substrate [9]. From the model formulation, the critical bonding strain ε_c and critical bonding strain rate $\dot{\varepsilon}_c$ need to be calibrated for the current material system. The calibration method is as follows [15].

In order to calibrate the model parameters, a wide range of ε_c and $\dot{\varepsilon}_c$ combinations are tested, without friction effects, to observe how the steady-state restitution ratio varies with respect to average bonding parameter, for both particle sizes. This set of parameters may then be generalized to other particle sizes to predict critical velocity for other different-sized Al particle impacts on Al substrates. Figure 4.2 shows plots of restitution ratio vs. average bond parameter from the results of all the calibration tests. Solid vertical and horizontal lines represent the classification tolerances for average D_{bond} and restitution ratio, respectively such that only tests resulting in data points in the bottom right quadrant are considered bonded. Labeled data points refer to model parameters which produced a particle that isn't bonded but has been affected bonding forces (i.e. partially bonded particles). These will used in Section 4.1.4 in analyzing bond initiation sites.

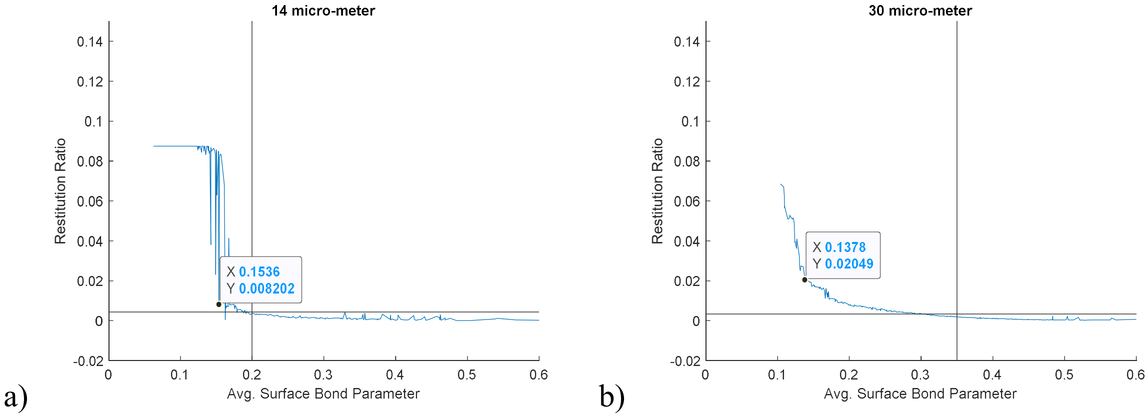

Figure 4.2: Plots of restitution ratio at 100 ns with respect to average surface bonding parameter for 14 μm (a) and 30 μm (b) diameter Al powder particles. Solid vertical and horizontal lines represent the classification tolerances for average D_{bond} and restitution ratio, respectively. Labeled points indicate tests results within the transition zone.

With this, the problem has been simplified to only have a binary result for each test of either a fully bonded or not bonded powder particle. Since the outcomes have now been classified into two main categories, logistic regression can then be applied to identify the bonding boundary along a plot of ε_c vs. $\dot{\varepsilon}_c$ along bonding is deemed to have just barely occurred. The intersection of these boundaries for both the 14 and 30-μm diameter particles can then be determined to be the calibrated bonding model parameters which may be applied for all particle sizes. Note that although the precise tolerance values are not particularly relevant, they were required to be adjusted by inspection to ensure a bonded boundary intersection.

Logistic regression is a well-established method with wide use in machine learning algorithms [79]. A Matlab program has been developed previously within FATSLAB to perform logistic regression on the model calibration results. The process can be described as follows [80]:

1. First, the final output of each test must be classified as either bonded or not bonded. To do so, a set of tolerances is required to define which test results are considered bonded (or have a value of $y = 0$) and which are not bonded (or have a value of $y = 1$). Based on the plots from Figure 4.2, the outputs from each test are classified into two discrete groups as follows for both particle sizes.

$$y_{14\mu m} = 1 \; for \; CoR \leq 0.002 \;\&\; ABP \geq 0.15$$
$$0 \; otherwise \qquad (4.8)$$

$$y_{30\mu m} = 1 \; for \; CoR \leq 0.0015 \;\&\; ABP \geq 0.25 \qquad 0 \; otherwise \tag{4.9}$$

where CoR is the coefficient of restitution and ABP is the average surface bond parameter tolerance value depicted in Figure 4.2.

2. Then a hypothesis must be defined which is limited between values of 0 and 1 with 0 corresponding to one category and 1 the other. In logistic regression, this hypothesis takes the form of a Sigmoid function shown below.

$$h(Z) = \sigma(Z) = \frac{1}{1 - e^{-Z}} \tag{4.10}$$

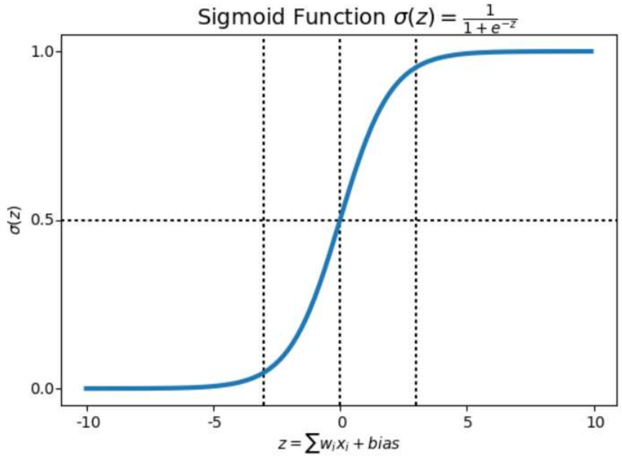

Figure 4.3: Typical sigmoid function graph centered at Z = 0 [80].

This hypothesis will be defined for each calibration test run, meaning that it will have *m* components for *m* number of tests.

3. Z in the above equation represents the input to the hypothesis and is typically represented by a polynomial of arbitrary order. A second order logistic regression is used in this case meaning that Z takes on the following form:

$$Z = \theta_1 + x_1\theta_2 + x_2\theta_3 + x_1^2\theta_4 + x_1x_2\theta_5 + x_2^2\theta_6 \tag{4.11}$$

where θ_i are unknown coefficients and x_1 and x_2 are the bonding model parameters ε_c and $\dot{\varepsilon}_c$, respectively used in each calibration test. In matrix form, Z can be represented as

$$Z = [1 \quad x_1 \quad x_2 \quad x_1^2 \quad x_1x_2 \quad x_2^2]\begin{bmatrix}\theta_1\\ \theta_2\\ \theta_3\\ \theta_4\\ \theta_5\\ \theta_6\end{bmatrix} = \boldsymbol{X}(x_1, x_2)\boldsymbol{\theta} \tag{4.12}$$

4. With the hypothesis now defined, it is then possible to define a cost function. The cost function for logistic regression is a scalar value and can be defined as follows [80]:

$$J(\boldsymbol{\theta}) = -\frac{1}{m}\sum_{i=1}^{i=m}\left(y^i \log\big(h(Z)\big) + \left(1 - y^i\right)\log\big(1 - h(Z)\big)\right) \tag{4.13}$$

   where y^i represents the previously classified output from test number *i* (either 0 or 1), Z as defined by Equation (4.12), log is the natural logarithmic and m the total number of tests performed. With this, each calibration test contributes a certain amount to the error function $J(\boldsymbol{\theta})$.

5. At this point, the bonding boundary identification problem has been reduced to an optimization problem where the goal is to find the values for $\boldsymbol{\theta}$ which will result in the smallest value of $J(\boldsymbol{\theta})$. To do so, the fminunc function for finding the minimum of an unconstrained multivariable function is utilized from the Matlab Optimization Toolbox with the following gradient definition [81, 80]:

$$\frac{\delta J(\theta)}{\delta \theta_j} = \frac{1}{m}\sum_{i=1}^{i=m} X_j^i \cdot \left(h(Z) - y^i\right) \tag{4.14}$$

   where X_j^i is defined for each test number *i* as the *j* components of the $\boldsymbol{X}$ array shown in Equation (4.12).

Through this process, the values of the $\boldsymbol{\theta}$ array have been found which will result in a minimum cost function $J(\boldsymbol{\theta})$. With this, it is then possible to work backwards to calculate the components of the $\boldsymbol{X}$ input array which will result in a specific value of $h(Z)$. It should be noted that by the class definition, a value of $h(Z) = 1$ corresponds to a test with a bonded result while $h(Z) = 0$ a test with a rebounded result. Since the purpose of the logistic regression is to identify a decision or bonding boundary, solving for the components of $\boldsymbol{X}$ which will produce a value of $h(Z) = 0.5$ will be the model parameters which will result in a result that is at the boundary of the bonded and not bonded classifications. Without any offset, this value corresponds exactly to $Z = 0$ meaning that the bonding boundary can now be identified as the ε_c and $\dot{\varepsilon}_c$ values which need to be input to array $\boldsymbol{X}$ in Equation (4.12) to produce $Z = 0$, thus giving the coordinates in a ε_c vs. $\dot{\varepsilon}_c$ plot of points along the bonding boundary curves. By following this logistic regression process, the following bonding boundary curves shown in Figure 4.4 are identified.

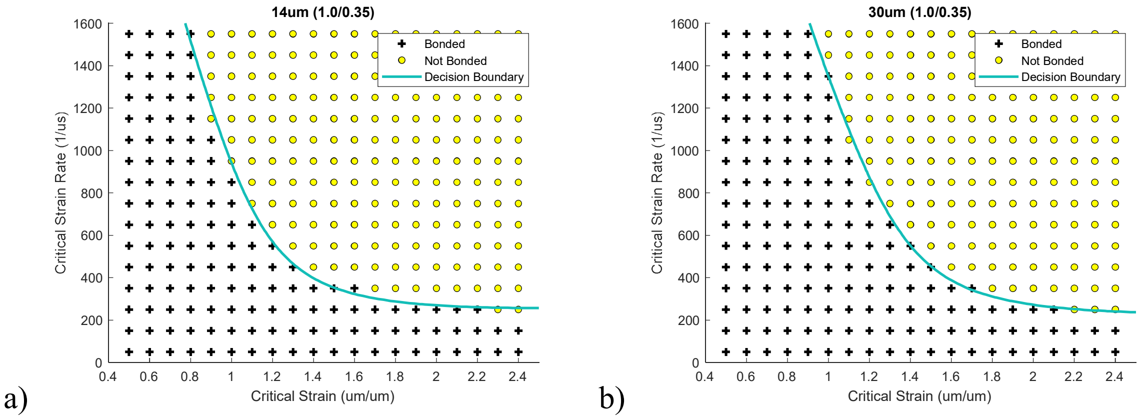

c)

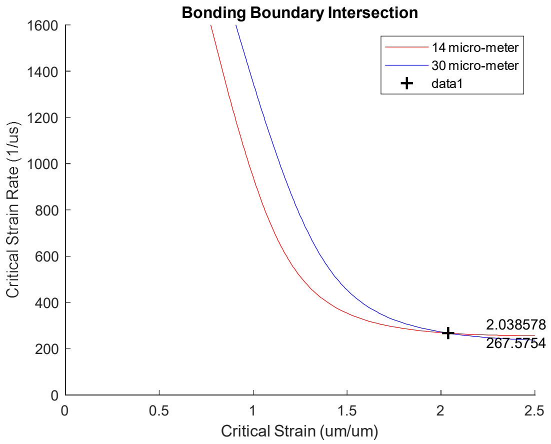

Figure 4.4: Logistic regression plots showing the boundaries at which bonding occurs based on the previously identified tolerance values for the 14-µm (a) and 30-µm (b) diameter powder particles. The intersection of these boundaries (c) identifies the set of model parameters that would result in bond initiation for both-sized particles impacted at critical velocities.

Although an intersection is achieved, it should be noted that the bonding boundaries are not very similar throughout. This is not ideal and suggests that the current strain-based model only predicts bonding accurately for different particle sizes with model parameters specifically at the intersection point. Consequently, there exists a large number of model parameter combinations which may predict bonding for one particle size but no bonding for another. Producing bonding boundaries which show more overlap throughout the domain will allow for more consistent bonding predictions of different particle sizes with a wide range of model parameters. Nevertheless, there exists two other issues of greater concern which will be discussed in the following sub-sections.

4.1.3 Discretization Sensitivity Issue

The most concerning issue with the above bonding model is its sensitivity to grid configuration (i.e. discretization level). Jetting phenomena is experimentally observed to be critical for bonding [9, 28, 8], thus the fact that it is able to be realistically captured in the form of numerical fracture of material points within a simulation is an advantage of using the MPM. However, a drastically different amount of effective plastic strain is observed to be predicted in tests without bonding implementations using different grid configurations.

To demonstrate this, tests of a 14-µm particle impacting at critical velocity with a 1.0/0.35 and 0.5/0.175 grid configuration are conducted with the differences shown in Figure 4.5. As it can be seen from the strain contours, although jetting is not as visible in the coarser grid, it becomes apparent with grid refinement as material points of the powder particle can be seen to be completely ejected from the body. Although these tests did not include bonding effects, these results already suggest that a strain-dependent direct bonding model will show an unacceptably high sensitivity to the level of discretization. Consequently, it may be expected that the model will predict a significantly different bonding result for different grid configurations despite all other parameters remaining the same. A modification to the numerical implementation of the bonding model that significantly alleviates this issue will be presented in Section 4.3.

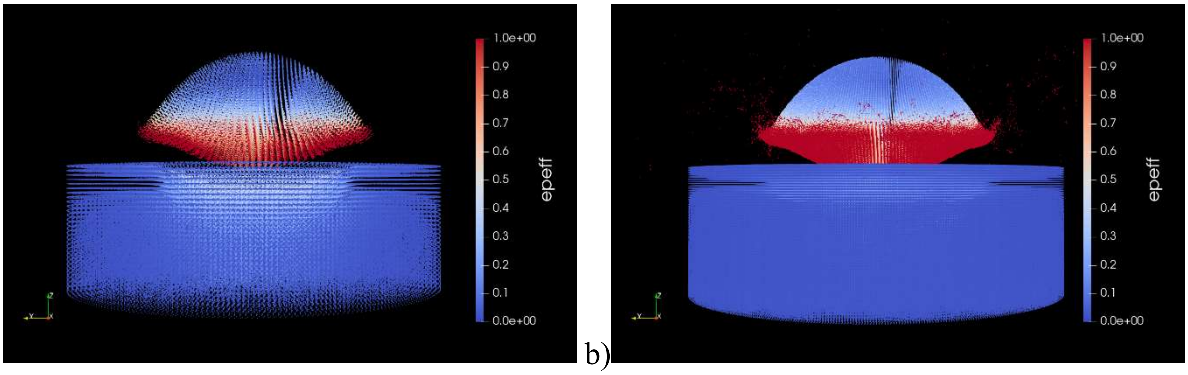

a) b)

Figure 4.5: Effective plastic strain distribution in the 14-µm particle using a) 1.0/0.35 and b) 0.5/0.175 grid configurations with no bonding model considerations shows that material jetting becomes apparent as the grid is refined.

Figure 4.6a explicitly compares the predicted bonding boundaries for the 14-µm diameter particle determined using two different grid configurations and identical classification tolerances. As it can be seen, the bonding boundaries are extremely different from each other, demonstrating the discretization sensitivity of the proposed model. Analysis of the effective strain contours in Figure 4.6b and 4.6c further shows this sensitivity to discretization as a drastically different material behavior is predicted with different grid configurations to the point of having different bonded results for the same model parameters. Both contours in Figure 4.6b and 4.6c have been calculated using the same $\varepsilon_c = 1.4$ and $\dot{\varepsilon}_c = 850\ s^{-1}$ parameters, labeled as *data1* in Figure 4.6a. Such sensitivity to discretization must be avoided with any FEM and adjustments must be made in the future to resolve this issue.

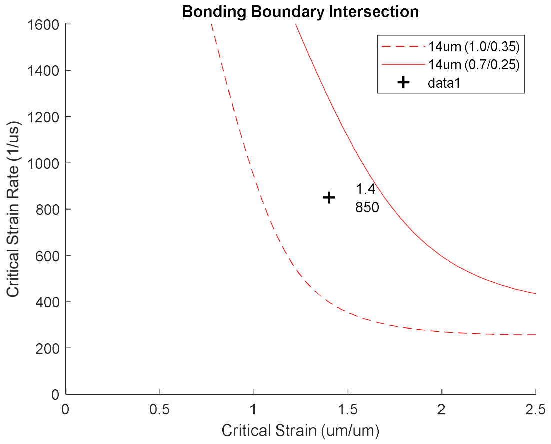

a)

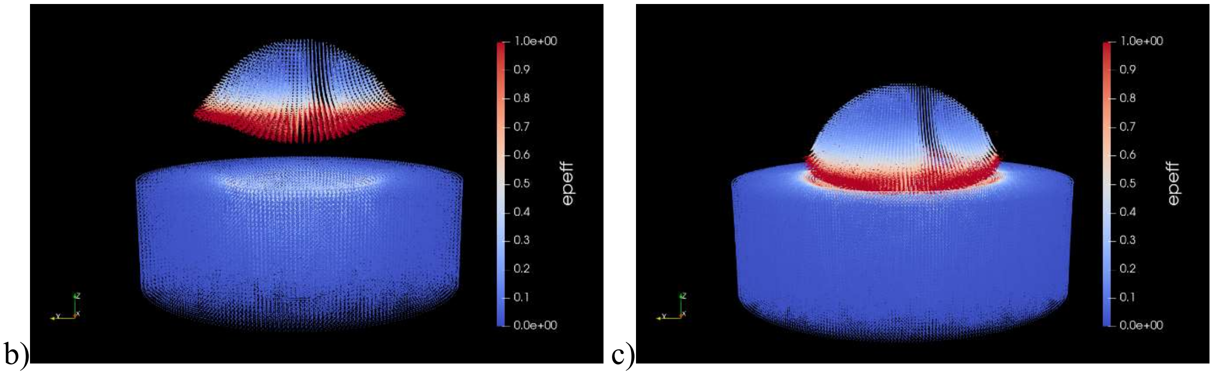

Figure 4.6: a) Plot of predicted bonding boundaries for the 14-um diameter particle using a grid configuration of 1.0/0.35 and 0.7/0.25. Effective plastic strains determined using the same bonding model parameters labeled in a) are also shown using grid configurations of b) 1.0/0.35 and c) 0.7/0.25.

4.1.4 Bond Initiation Site Issue

Another issue with the strain-based bonding model is the locations where strong bonding effects are predicted. As it can be seen in Figure 4.2, there is a transition region where the restitution ratio of the impacting powder particle goes from rebounded to bonded values with respect to the average bonding parameter. Analysis of the contour plots of tests within the transition region where a partially bonded particle is present can be beneficial in revealing where bonding is initiating within the simulation. Figure 4.7 shows the contour plot of effect plastic stress in a 14-µm diameter powder particle from the labeled test point in Figure 4.2a with model parameters set within the transition region. As it can be seen, the powder particle appears to have rebounded to a degree but are held back by a small number of bonded particles around the perimeter of the contact surface. Consequently, this suggests that particles within this region are experiencing strong bonding effects relative to the rest of the contact interface. This result clearly does not align with experimental observations of material jets and points towards possible intrinsic issues within the bonding model. Strong bonding within the shear-dominated jetting region, is also likely to violate the basis of the D_{bond} evolution law, where it is assumed that there is always sufficient normal contact pressure for proper bonding.

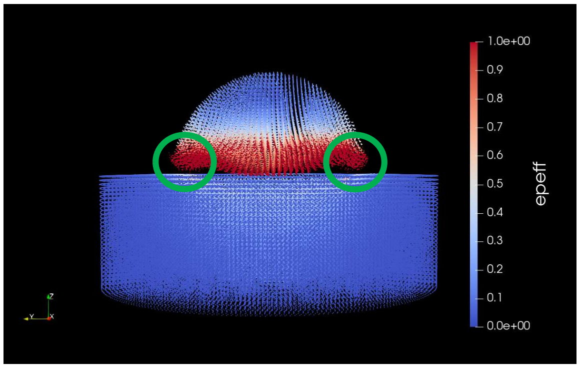

Figure 4.7: Contour plot of the effective plastic strain in the 14-µm diameter Al particle at 120ns post-impact. Circled regions show that bonding initiates in near the perimeter of the contact surface within the jetting region.

For the jetting region to be the site of bond initiation also does not align with previous experimental studies for CS of Cu, Ti and Ti-6Al-4V particles [82, 83, 84]. Such a result is also contrary to Al/Al simulations by Rahmati and Jodoin [49] using an ALE framework, where it was observed that bonding occurs away from the jetting zone and more towards the south pole of the particle. Reasoning for their result is that normal pressure, and not shear, is the driving mechanism for extruding material into surface cavities leading to intimate contact and bonding. Such a conclusion is deemed reasonable and as a result, bonding should not be expected to initiate in the shear-dominated jetting region. This suggests that a strain-dependent bonding model that only considers shear strains of the contacting surfaces can lead to inaccurate predictions of bond initiation sites. An alternative formulation that resolves this shortcoming which relies on energies rather than shear strains to formulate the bonding criterion will be discussed in Section 4.3.

4.2 Convergence Test

4.2.1 Convergence Test Motivation

The mesh dependence issue discussed in the previous section makes predictive simulations difficult to obtain since different grid configurations lead to different results. This prompts a mesh convergence study whose purpose is twofold: first, to assess the level of mesh dependence and study its characteristics and, second, to identify a less mesh-dependent measure upon which to base the bonding model. This measure should still be able to define the threshold level of material jetting leading to bonding and ideally also improve the accuracy of the predicted bond initiation sites.

4.2.2 Convergence Test Set-up

Since it is well-known that a source of divergence in MPM is the number of material points per computational grid [69], a range of grid size and particle spacing combinations are tested. Although grid refinement does have the highest influence on accuracy, the number of material points or particles in the test also plays a significant role [69]. As such, it is deemed necessary for the current tests to account for this by testing three different particle spacings for each grid size under consideration. Regardless of grid size and particle spacing, the powder particle and substrate dimensions are kept identical between each convergence test with a 14 μm diameter Al particle to minimize external effects. All convergence tests are performed without bonding considerations. The grid configurations tested at the critical impact velocity of 810 m/s are listed in Table 4.1. Given the large deformations expected, relatively fine particle spacings are used with each grid size to avoid significant errors from insufficient particles per grid.

Table 4.1: Grid configurations used in convergence testing.

	1.5 μm Grid Size			**1.0 μm Grid Size**			**0.5 μm Grid Size**		
Particle Spacing (μm)	0.5	0.4	0.35	0.4	0.35	0.25	0.2	0.175	0.15

A scaling factor of 0.05 times the critical time step size defined by the smallest tested grid size of 0.5 μm is used for all convergence tests. This choice of the time step size, which is significantly smaller than the critical value imposed by the stability condition of an explicit time stepping scheme, was made to resolve the time domain variations with a high resolution and minimize the errors that may be caused by temporal discretization. In the final model testing, this scaling factor will be adjusted to determine the optimal time step size for which the bonding model still shows good performance without excessive computational costs.

4.2.3 Convergence Test Results

Figure 4.8 below shows the average plastic strain in the powder particle throughout the simulation predicted by all tested grid configurations. This is done as a basic method to quantify the strains in the powder particle and observe its sensitivity to discretization. For simplicity, contact between the surfaces is considered to be frictionless in all tests. Tests with a friction factor of 0.2 were also performed with a similar convergence result was found demonstrating that friction implementation does not noticeably affect convergence. Note that several of the results were not able to be run fully to the 1000 ns end time due to the 24 h runtime limit from the Niagara supercomputer on which all tests are conducted. Figure 4.5 shows the plastic strain contours calculated using 1.0/0.35 and 0.5/0.175 grid configurations. Significant differences can be seen particularly around the perimeter of the contact interface where particles can be observed to be ejected outwards with the finer discretization.

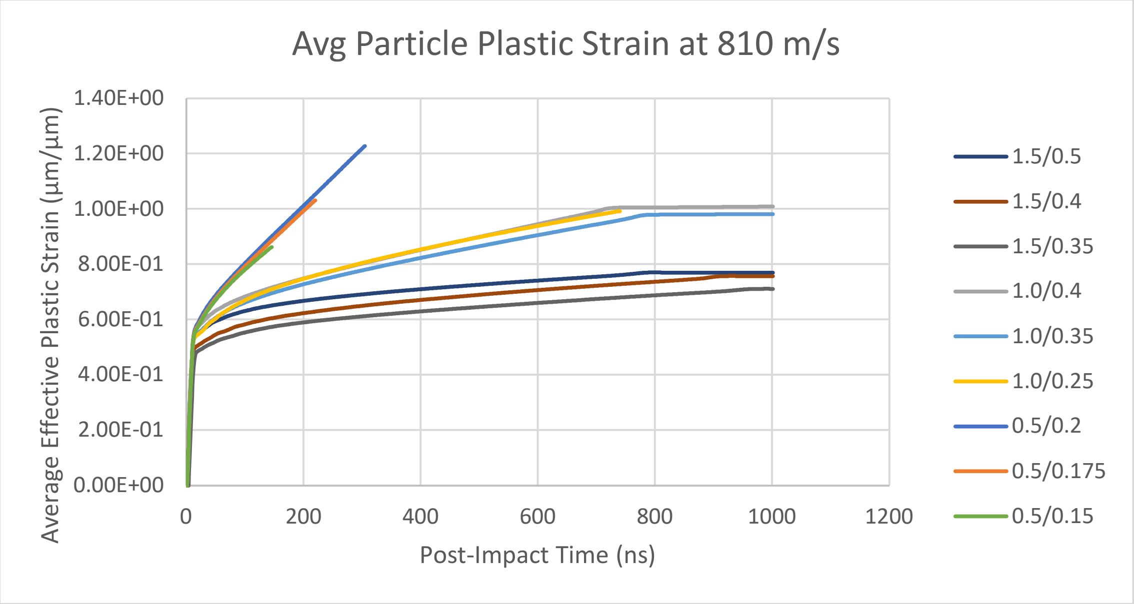

Figure 4.8: Plots of average effective plastic strain for the powder particle based on the PTW constitutive model without friction and bond effects considered.

From the above plot, it is clear that although the final predicted steady-state average effective plastic strains are fairly stable with respect to the tested particle spacings or particles per grid values, strains do vary drastically with grid size refinement. Not only can the final average plastic strain of the powder particle be inferred to be different with grid refinement, but the slopes or average strain rates beyond the initial time steps are drastically different as well. Strain values appear to converge to similar values for each grid size and with increasing numbers of material points per computational grid. As such, this result proves the discretization sensitivity of strain in MPM and the need for identifying a different, grid insensitive measure of material jetting.

4.2.4 Strain Energy Density Convergence

The concept of an adhesion energy as a function of sublimation energy has been previously studied by Manap and Profizi et al. [34, 35]. In these models, bonding is deemed to occur if adhesion energy is greater than rebound energy which suggests energy as an alternative measure of a threshold jetting value for bonding. Motivated by this, although it is clear that average plastic strain is extremely sensitive to grid size, it was found that average plastic strain energy density of the powder particle exhibits less sensitivity to discretization. Plastic strain energy density is calculated by Equation (4.15) as a function of the von Mises flow stress and plastic strain in each step.

$$E_p = \int_{\varepsilon^p=0}^{\varepsilon_c^p} \sigma_{vm} d\varepsilon^p \tag{4.15}$$

This can be observed in Figure 4.9 where the final value and rate of change of the energy density values obtained from different grid configurations clearly show smaller discrepancies. This can be attributed to the fact that although the jetted particles possess extremely high strains, they are subjected to negligible internal stresses.

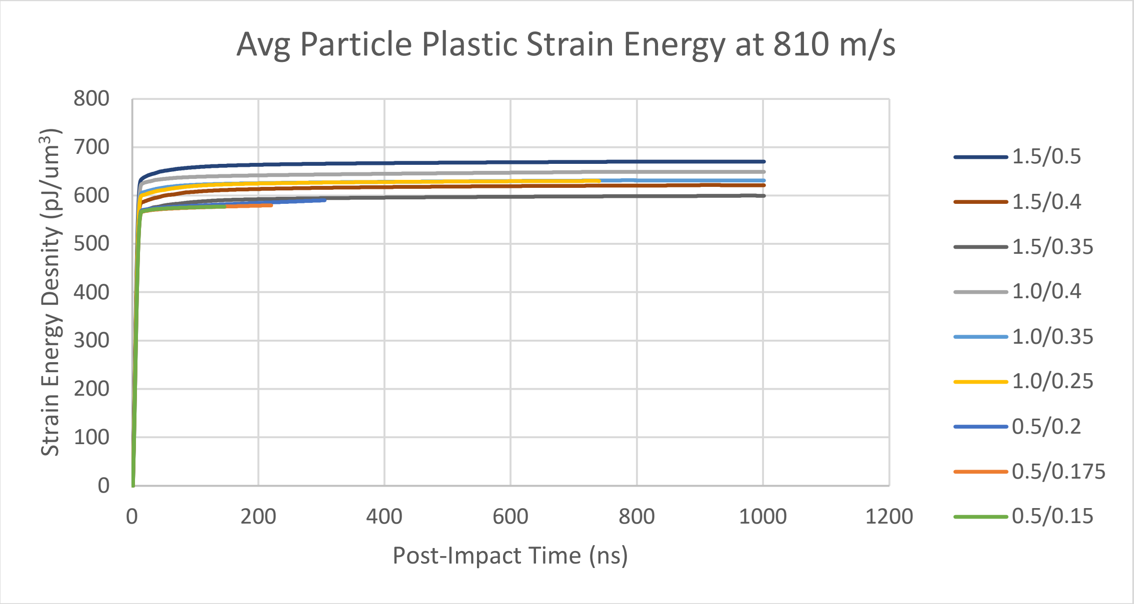

Figure 4.9: Plots of average plastic strain energy density for the powder particle calculated using the PTW constitutive model with no friction or bond effects considered.

Although these results are promising, it must be noted that the convergence of E_p is expected to change with the consideration of bond effects. The material jetting phenomenon in particular can be expected to be heavily affected by bonding effects incorporated directly into the simulation. This means particle strains and strain energy densities in a simulation where bonding effects are directly enforced will be very different from the present non-bonding tests. As a result, this suggests that the intrinsic issue of grid size dependence within MPM may not be fully addressed by using a simple energy density-based model. Nevertheless, the convergence study still suggests that an energy-based quantity is an improvement over strain as a measure of material jetting and bonding less sensitive to discretization. Specifically, strain energy has the potential to be a better numerical representation of the physical parameters which describe jetting and bonding. Thus, it is concluded that modifying the model to be based on energy rather than shear strain, and possibly other techniques, may lead to less discretization sensitivity.

4.3 Energy-based Bonding Model

4.3.1 Motivation for Development

An adhesion model based on an energy dissipative cohesive model has also been directly implemented by Profizi et al. [35] within an SPH framework. They were able to accurately predict critical velocity and include a damage value to cause breakage of cohesion before all surface adhesion energy has dissipated in order to predict the maximum impact velocity beyond which erosion will occur [35]. Several other studies have included adhesion energy as an input specifically in modeling the effect of oxide layers on critical velocity [85, 86]. Nevertheless, only a small number of studies in total have been conducted which have attempted to directly incorporate adhesion/bonding forces within a simulation using the concept of an adhesion energy within an SPH or Lagrangian formulation [61, 62, 64]. Again, adhesion energy in these studies has been quantified as a function of sublimation energy, microstructure characteristics and the bonded atom fraction relation for high-speed impact developed by Shorshorov and Kharlamov [65].

The motivation for development of the current model is to address the gap in direct bonding implementation within an MPM framework that shows advantages over both mesh-based FEMs and other particle-based methods like SPH. Furthermore, improvements are considered such as the inclusion of the PTW constitutive model and SCG melt model which is better suited to CS conditions [47]. The shift to an energy-based bonding model is motivated by previous works [61, 62, 35, 49], as well as results of the convergence study which suggests that energy will result in less variance in simulation results with respect to grid size. In contrast to previous energy-based adhesion models, the current formulation will focus on using continuum-level measures from within the simulation to calculate adhesion energy and predict bonding rather than atomic-scale material properties [65].

4.3.2 Energy-Based Bonding Model Formulation

The overall formulation of the bonding model is nearly identical to the original strain-based model, with the exception of how the bond parameter increment ΔD_{bond} is calculated. Rather than ε_c and $\dot{\varepsilon}_c$, ΔD_{bond} is instead described as a function of critical surface adhesion energy and energy rate G_c and $\dot{G}_c$. Surface adhesion energy is defined as the energy required for adhesion of a unit surface area and has been used in SPH adhesion models [35]. It is equivalent to the strain energy release rate G used in fracture mechanics for determining the work required to close a crack [87].

In the energy-based bonding model, the evolution speed of D_{bond} within each material point $\boldsymbol{x}_p$ will be defined by a critical surface adhesion energy G_{bond}, whose value is defined by G_c and $\dot{G}_c$, which need to be calibrated. Mathematically, this is expressed as Equation (4.16):

$$D_{bond}(\boldsymbol{x}_p) = \sum_{t_1,t_2,\dots} \mathit{\Delta} D_{bond}(\boldsymbol{x}_p) = \sum_{t_1,t_2,\dots} \frac{\Delta G_s(\boldsymbol{x}_p)}{G_{\mathrm{bond}}} \tag{4.16a}$$

$$where\ G_{bond} = G_c \left(1 - ln \frac{\Delta G_s(\boldsymbol{x}_p)}{\dot{G}_c \Delta t}\right) \tag{4.16b}$$

in which $\Delta G_s(\boldsymbol{x}_p)$ is the increment in surface adhesion energy for each material point $\boldsymbol{x}_p$. Similar to the previous model, a sticking contact condition is enforced at a grid node when sufficient material jetting has occurred and $D_{bond}(\boldsymbol{I}_g) > 1$ [15].

In terms of the numerical implementation of the above model, a regularization approach should be implemented similar to what is often used in damage/fracture mechanics to address mesh dependence of the numerical results. It is well known that the amount of energy dissipation in damage/fracture modeling is known to be sensitive to mesh size in traditional FEM [88] unless proper remedies are considered in the numerical implementation of the damage/fracture. Physically, the dissipated energy per unit crack surface is given by

$$G = \lambda \int_{\varepsilon=0}^{\varepsilon_c} \sigma d\varepsilon \tag{4.16}$$

where λ is a specific characteristic length of the material representing the physical width of the localization zone [88, 89]. Numerically, damage localization and eventual fracture always occurs across a single band of elements. Thus, the amount of dissipated energy will be different with different discretization sizes such that it decreases to zero in the limit of mesh refinement, making any argument of FE mesh convergence impossible. In that case, the numerical model captures the amount of dissipated energy correctly only if the width of the elements is exactly qual to λ. This issue is most commonly addressed by scaling the fracture energy of the damage/fracture model w.r.t. to mesh size so that the amount of energy dissipated by a given width of elements matches the physical value [88]. The scaled fracture energy is thus regarded as an “algorithmic” value of the fracture energy rather than being a strictly physical quantity.

Given that bonding is a similar albeit opposite process to fracture, it is reasonable to postulate that bonding also occurs across a “bonding band” along the surface of each body. The width represented by λ in fracture modeling is analogous to the depth or thickness of this band of elements into each body. In MPM, the numerical width of the bonding band can be approximated by $DCell$ or the edge length of the computational grid. By including this measure into the formulation of the bonding criterion as a scaling factor, it allows for the same calibration parameters to be consistently and accurately applied across a range of grid configurations. This effectively reduces the sensitivity of the energy-based bonding model to discretization level.

Thus, the increment in surface adhesion energy $\Delta G_s(\boldsymbol{x}_p)$ for each material point $\boldsymbol{x}_p$ is calculated numerically as

$$\Delta G_s(\boldsymbol{x}_p) = \sigma_{vm}(\boldsymbol{x}_p)\Delta\varepsilon_p(\boldsymbol{x}_p)DCell \tag{4.17}$$

where σ_{vm} is the von Mises stress of the material point, $\Delta\varepsilon_p$ the effective plastic strain increment of a material point $\boldsymbol{x}_p$ and $DCell$ the grid length measure. By this formulation, the surface adhesion energy within the algorithm is effectively regularized with respect to grid size. To note is that although not shown for brevity, simply the strain energy density without the $DCell$ measure does not result in discretization insensitivity despite convergence test results. This can be attributed to the bonding model which directly affects material behavior in the simulation. Only with the inclusion of $DCell$ is an appropriate level of insensitivity achieved meaning this insensitivity is more as a result of including $DCell$ than purely switching to an energy measure.

4.3.3 Calibration Test Setup

A more complete test is conducted to fully evaluate the energy-based bonding model performance as it will serve as the final proposed model of this thesis. In terms of the test setup, it must be noted that it is well known that large inaccuracies in energy measures can result from insufficient material points per grid. Larger changes are observed with larger grid sizes but the variations themselves have been observed to decrease as the number of material points is increased [69]. In order to account for this source of error, three initial material points per grid values will be tested for each grid size $DCell$. By extension, it can also be noted that particle spacing is essentially governed by computational grid size due to particle per grid requirements.

Three sets of grid sizes will be tested, each with three approximate particle per grid values as stated above. The result is a total of nine final grid configurations that will be tested for each powder particle size as listed in Table 4.2. By testing these grid configurations, it is also possible to explicitly quantify the effects of different $DCell$ and dp. All approximate initial particle per grid values considered are relatively high at approximately 8, 20 and 40 as the severe deformations each body experiences can lead to cases where there are relatively few particles in a grid. An acceptable bonding model must show convergence with grid and particle spacing refinement, as the particles act essentially as integration points within the grid element. Increasing the number of integration points in a FEM should not lead to a drastically different solution.

Table 4.2: All tested grid configurations for each particle size grouped by grid size and listing the approximate number of initial particles per grid.

Grid Config.	**Particles/grid**	
	14-µm	30-µm
1.5/0.5	9.08	9.00
1.5/0.35	28.0	26.0
1.5/0.3	41.4	41.5

Grid Config.	**Particles/grid**	
	14-µm	30-µm
1.0/0.35	8.74	7.79
1.0/0.25	22.7	21.6
1.0/0.2	44.3	42.1

Grid Config.	**Particles/grid**	
	14-µm	30-µm
0.7/0.25	8.04	7.63
0.7/0.175	23.5	22.6
0.7/0.15	38.1	35.4

All tests for both particle sizes are done with a 0.1 scaling factor on the critical time step size for a 0.5-μm grid, except for the finest grid configuration of 0.7/0.15 which uses 0.2. This is done in order to keep the dimensions of the system consistent across all tests and still achieve a steady state result within Niagara usage limits. Further testing and discussion on an ideal time step scaling factor can be found in Section 5.1.4, however in short, so long as the scaling factor remains below around 0.2, the differences are negligible. Since the proposed bonding model is primarily based upon achieving a threshold level of material jetting, it is critical for it to be properly captured within the simulation. A cylindrical substrate with a height of 10 μm is used for both particle sizes while diameters of 30 and 50 μm are used for the 14 and 30-μm particles, respectively across all tests.

Note that the substrate diameters have been set to be significantly larger than the particle diameters while height remains relatively low across all cases. This is done as the substrate is not restricted by any radial boundary conditions while its bottom surface is bound vertically by the computational grid. Given these boundary conditions, substrate height effectively only serves to define the thickness of a semi-infinite substrate, represented numerically through the inclusion of absorbing boundaries, and should not drastically affect jetting as it is primarily in the radial direction. Meanwhile, radial substrate deformations resulting from a lack of boundary conditions can impose internal forces on the contact interface which are not present in practice. In the worst case, the substrate may even be unable to fully accommodate the powder particle as it deforms radially and fail to provide a complete contacting surface. By this reasoning, it is deemed that an insufficient substrate diameter will be more problematic than insufficient height. Although a taller substrate would yield improved results (particularly with larger particles), any increase to substrate height would significantly increase computational cost without much benefit to predicted material behavior. Due to the above reasons and in order to maintain consistent system dimensions across all grid configurations for the same-sized particle, substrate height is kept consistent and relatively small while large diameters are used.

Chapter 5 Final Model Results and Discussion

The primary goal of the following sections is to present and analyze the results of the energy-based bonding model implemented within an MPM framework, as described in Chapter 4. Results from model calibrations and testing are shown and discussed. Final calibrated model performance is evaluated with identification of critical velocities, bond quality and performance in multiparticle simulations.

5.1 Simulation Results and Discussion

5.1.1 Model Calibration Results from Logistic Regression

Following a similar logistic regression process as with the strain-based model, tests were conducted in order to calibrate the critical surface adhesion energy G_c and energy rate $\dot{G}_c$ values. A wide range of model parameter combinations are tested. All results are extracted from tests completed until steady state, which is achieved for both particles at approximately 50-60 ns post-impact. The nine grid configurations listed in Table 4.2 are tested with both the 14 and 30-µm particle sizes to identify the respective bonding boundaries and boundary intersections. Considering the two particle sizes, this constitutes a total of eighteen grid configuration tests, each of which consisting of 375 simulations.

With this, the discretization sensitivity of the bonding model and MPM in general can be evaluated under CS conditions. Impact velocities are set to the experimentally determined critical velocity of 810 m/s and 770 m/s for the 14-µm and 30-µm particles, respectively [9]. Bonding boundaries for the three tested grid sizes with initial particles per grids of around 20 are shown in Figure 5.1, with a similar trend observed in all other grid configurations. The predicted bonding boundaries can be seen to be very similar to each other across the different tested grid configurations.

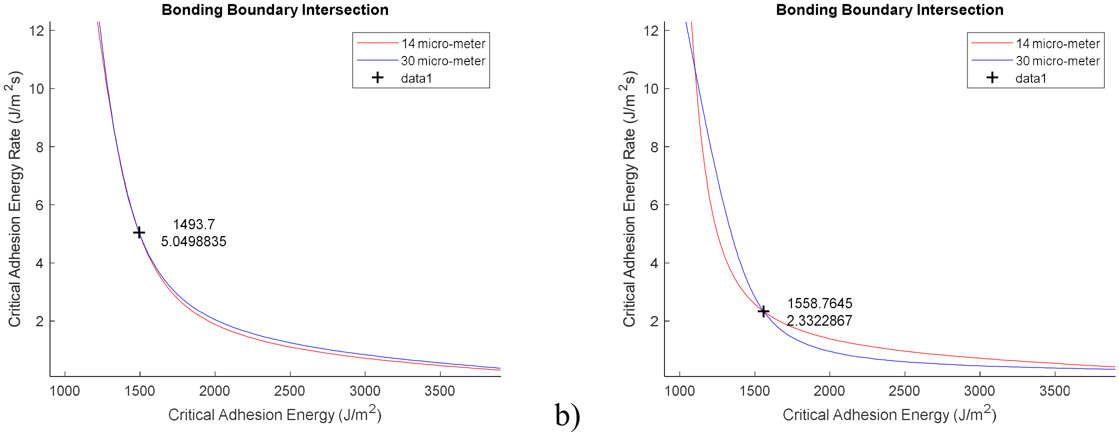

a)

b)

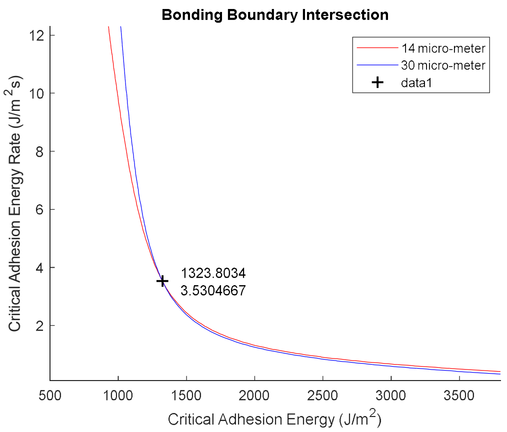

c)

Figure 5.1: Bonding boundaries and intersections achieved with the adhesion energy-based bond model with a grid configuration of a) 1.5/0.35, b) 1.0/0.25 and c) 0.7/0.175.

Figure 5.2 summarizes these results by showing the identified boundary intersection points for each grid configuration. With these results combined, it can be seen that the current bonding model is much less sensitive to discretization. This is largely be attributed to the inclusion of $DCell$ within the bonding model formulation which serves to regularize the bonding parameter increments and adhesion energy to the grid size. As was previously mentioned, this regularization with respect to element size concept is standard in damage/fracture modeling. Since the size of the computational grid is an approximation of element size in MPM, regularization with respect to $DCell$ can be seen here to also be important in bond modeling. Without the $DCell$ term, a drastically different range of intersections and bonding boundaries will be predicted with the different grid sizes.

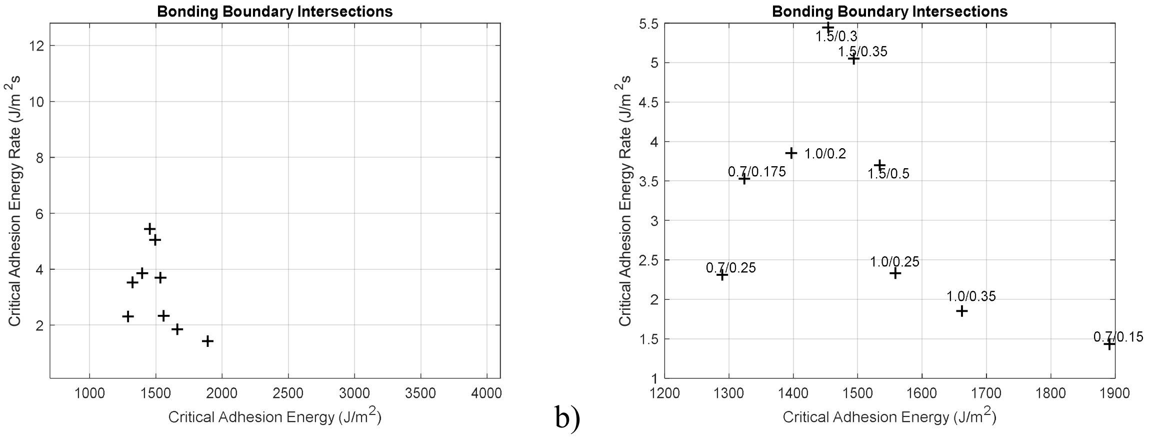

a) b)

Figure 5.2: a) Plot of all intersection points using the same axis dimensions as the tested domain and b) expanded view of intersection points, labelled with the associated grid configuration with which they were identified.

Although similar intersection points are obtained, analysis of the result classification process leading to identification of these bounding boundaries and intersections revealed an issue which must be addressed. As was previously described in Section 4.1.1, logistic regression requires tests with each set of model parameters to be first classified as bonded or not bonded. For this, tolerances for restitution ratio and average surface bond parameter were used in the strain-based model and have been implemented here as well. Table 5.1 lists the tolerances used to generate the bonding boundary intersections shown in Figure 5.2.

Table 5.1: Average bond parameter and restitution ratio tolerances (average bond parameter/restitution ratio) used to generate the bonding boundary intersections shown in the previous figure, grouped together by grid size.

Grid Config. (1.5 grid size)	**Tolerances** (Avg D_{bond}/restitution ratio)	
	14-µm	30-µm
1.5/0.5	0.25/0.0031	0.35/0.002
1.5/0.35	0.25/0.003	0.38/0.002
1.5/0.3	0.25/0.003	0.39/0.002
Grid Config. (1.0 grid size)	**Tolerances** (Avg D_{bond}/restitution ratio)	
	14-µm	30-µm
1.0/0.35	0.2/0.003	0.34/0.003
1.0/0.25	0.2/0.0031	0.40/0.002
1.0/0.2	0.2/0.003	0.41/0.002
Grid Config. (0.7 grid size)	**Tolerances** (Avg D_{bond}/restitution ratio)	
	14-µm	30-µm
0.7/0.25	0.25/0.006	0.30/0.007
0.7/0.175	0.25/0.003	0.305/0.0031
0.7/0.15	0.25/0.003	0.29/0.0031

From Table 5.1, it is noted that in order to generate a proper boundary intersection from similarly shaped bonding boundaries, the classification tolerance for average D_{bond} in the 30-µm particle in particular had to be adjusted to be quite different from the 14-µm particle. Consequently, this led to the classification of several tests with critical parameters which met the restitution ratio tolerance for bonding but were instead classified as not bonded as they did not meet the average D_{bond} tolerance. To demonstrate this, Figure 5.3 shows the test results obtained using the 1.0/0.25 grid configuration, with again, a similar phenomenon being observed with every tested grid configuration. The solid horizontal and vertical lines represent the restitution ratio and average D_{bond}, respectively, such that only test results in the bottom right quadrant are considered bonded.

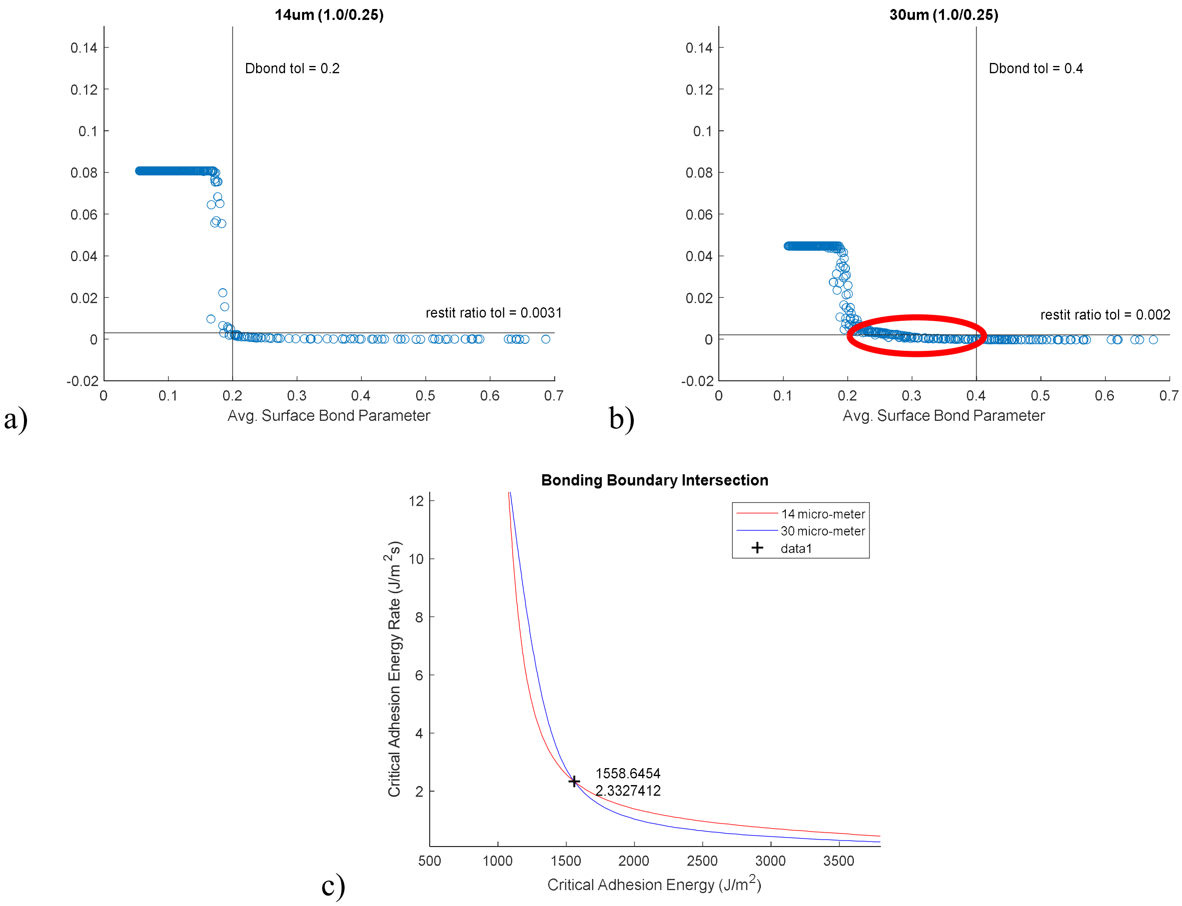

Figure 5.3: Energy-based bonding model simulation results with a 1.0/0.25 grid configuration showing the plots of restitution ratio vs. average bonding parameter (a, b) with solid black lines showing classification tolerances. Circled in red are test results which had to be incorrectly classified to achieve similar bonding boundaries. The bonding boundary intersection identified (c) for 14 μm and 30 μm diameter Al particles are also shown.

As it can be seen, there exists a significant amount of test results with the 30-μm particle within a wide range average D_{bond} values circled in red, where the larger particle is classified as not bonded despite having low enough restitution ratio. If these points were to be considered bonded as is expected from what is observed in the simulation based off the restitution ratio, the bonding boundaries from each curve would not intersect at all as shown in Figure 5.4. This is clearly problematic as it suggests that the bonding effects are being incorrectly modeled within the simulation of different-sized particle impacts. With the current view of the output data, there is no clear physical reasoning or explanation that can be derived to justify classification of the points circled in red in Figure 5.3 to be considered not bonded. Rather than disregard the entire model, an alternative classification metric is proposed to address this issue.

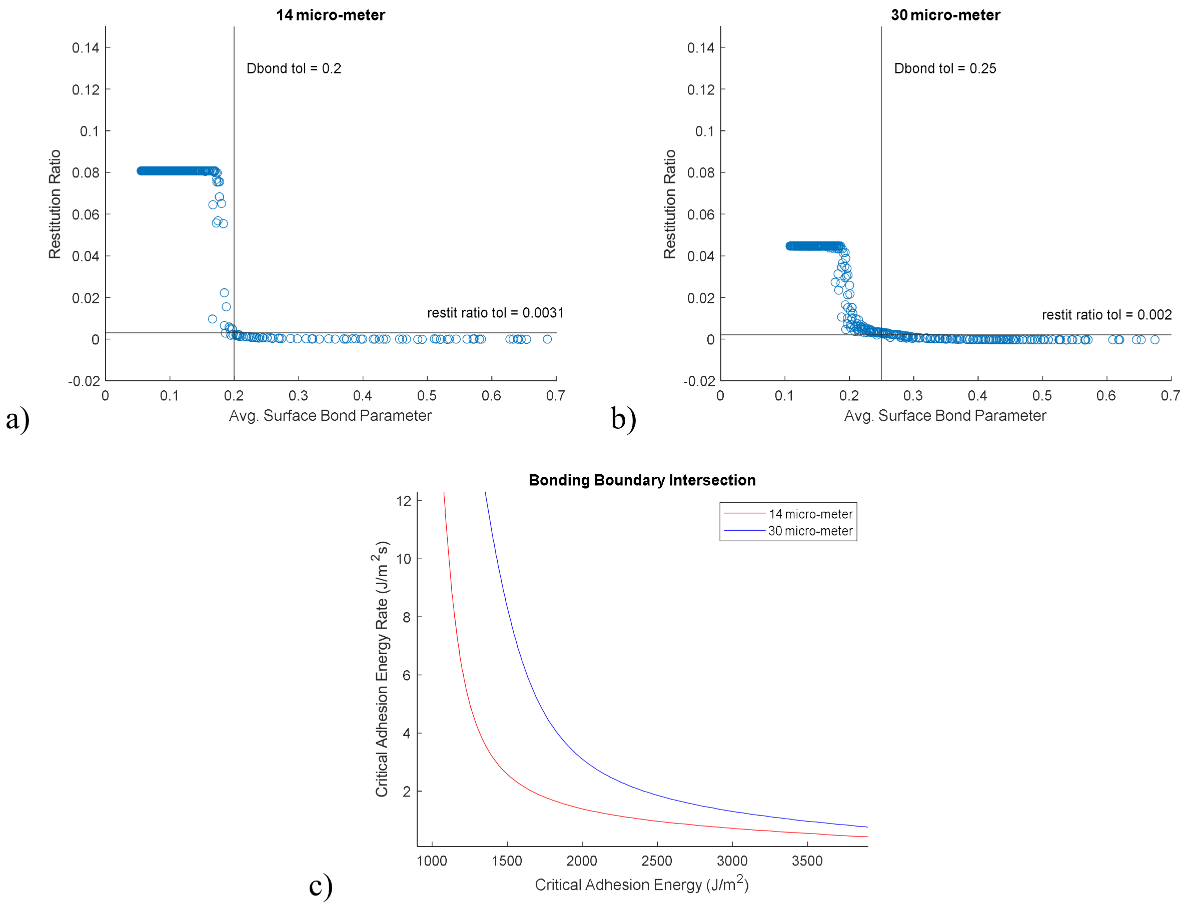

Figure 5.4: Energy-based bonding model simulation results with a 1.0/0.25 grid configuration showing the plots of restitution ratio vs. average bonding parameter (a,b) with solid black lines showing logistic regression tolerances that have been adjusted to expected values. The bonding boundaries predicted (c) show a clear difference between particle sizes and a lack of intersection.

5.1.2 Percent Bonded Contact Particle Classification Tolerance

Despite the classification tolerancing issues described in the previous section, there are still signs that show promise with the overall model. Key among these is that classifying the data points circled in red in Figure 5.3 as not bonded led to extremely similar bonding boundaries. Comparing this result to the purely strain-based bonding model in Figure 4.4, it is a clear improvement where no adjustments in tolerances led to such similar bonding boundaries. This suggests a change in perspective of the outputs is required and that average D_{bond} may not be the ideal tolerance for classifying the bonded status of tests.

Thus, a shift in perspective of the output data is proposed to minimize and justify the elimination of these data points. Previously, it was difficult to identify a precise value for complete bonding in all particle sizes using the average D_{bond} as a bonding classification tolerance. Instead, it is proposed that the percent bonded contact particles (PBCP) be utilized in lieu of the average D_{bond}. With using PBCP as a measure for identifying what constitutes a bonded particle, it allows for bonding classification that can be based on a quantifiable, physical metric with clear meaning as each particle represents a certain material volume. By defining a threshold value in terms of the PBCP and tracking its evolution over time, this allows for an indirect measure of the bond quality for different sets of process and material parameters. For instance, if a particle with the final calibrated model is to be impacted at an above-critical (i.e. supercritical) velocity, not only will the bond effects be directly simulated but the PBCP will return an above-threshold PBCP value to capture the effects of increased jetting. This accurately reflects the increase in coating density as well as bond strength with supercritical impacts observed both experimentally by Schmidt et al. [90] and numerically by Wang et. al [54].

To properly define PBCP within the bonding and contact algorithm implementation, it is first noted that the desired PBCP is with respect to the only the particles that have come into contact and not the total number of surface particles. This distinction is critical to maintain consistency of the measured value across tests with different particle sizes. Given the geometry of the bodies, it is fairly straightforward to specifically label material points on the surfaces as surface particles. As described in the bonding model formulation in Section 4.3.2, $\dot{D}_{bond}(\boldsymbol{x}_p)$ and thus $D_{bond}(\boldsymbol{x}_p)$ is only non-zero at material points which have come into contact with another body (i.e. $\boldsymbol{x}_p \in S$). Consequently, the total contacted area can be represented in each calibration test by the number of material points containing a non-zero D_{bond} value. In similar fashion, the total bonded area can be approximated by the number of material points with a $D_{bond}(\boldsymbol{x}_p) \geq 1$, as only the volumes represented by these points will be considered fully bonded. Mathematically, PBCP can be simply calculated by

$$PBCP = \frac{\#\ of\ material\ points\ with\ D_{bond} \geq 1}{\#\ of\ material\ points\ with\ D_{bond} > 0} \tag{5.1}$$

Although not a direct measure, the PBCP can also be related to the percentage of the contact area that has been bonded, despite surface area being difficult to define in the MPM. This is because each particle represents a certain volume which can then be associated with a certain surface area given some assumptions on the shape of the represented volume. In fact, PBCP will be equal to the percent bonded area if the surface area represented by each particle is identical. Of course, this is unlikely to ever be the case after particle impact. Nevertheless, for comparison purposes, it is deemed reasonable to assume material point volumes are similar enough in any given time step such that PBCP can be considered synonymous to the percent bonded area.

Figure 5.5 below then presents the identified boundary intersections identified using restitution ratio and PBCP tolerances while Table 5.2 lists the specific classification tolerances for each grid configuration. To note is that restitution ratio tolerances have been kept identical to those used when the average D_{bond} was used for consistency. It can be seen from Figure 5.5 that the boundary intersections are slightly different from those in Figure 5.2 but remain similarly close to each other relative to the tested domain.

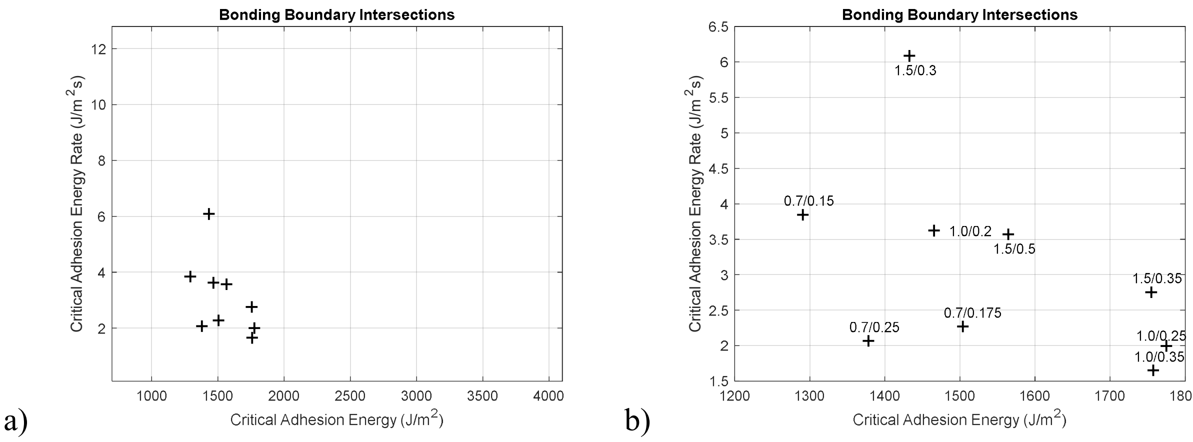

Figure 5.5: a) Plot of all intersection points using the same axis dimensions as the tested domain and b) expanded view of intersection points, labelled with the associated grid configuration with which they were identified.

Table 5.2: Percent bonded area and restitution ratio tolerances (PBCP/restitution ratio) used to generate the bonding boundary intersections shown in the previous figure, grouped together by grid size.

Grid Config. (1.5 grid size)	**Tolerances** (PBCP/restitution ratio)	
	14-µm	30-µm
1.5/0.5	8.5%/0.0031	8.1%/0.002
1.5/0.35	8.0%0.003	9.2%/0.002
1.5/0.3	8.5%/0.003	9.2%/0.002
Grid Config. (1.0 grid size)	**Tolerances** (PBCP/restitution ratio)	
	14-µm	30-µm
1.0/0.35	6.0%/0.003	8.1%/0.003
1.0/0.25	6.1%/0.0031	8.3%/0.002
1.0/0.2	6.1%/0.003	8.3%/0.002
Grid Config. (0.7 grid size)	**Tolerances** (PBCP/restitution ratio)	
	14-µm	30-µm
0.7/0.25	4.7%/0.006	4.9%/0.007
0.7/0.175	4.6%/0.003	5.3%/0.0031
0.7/0.15	4.8%/0.003	5.3%/0.0031

From the PBCP tolerances in Table 5.2, it noted that there is a clear convergence in the PBCP for what constitutes a fully bonded particle with grid size refinement. With the finest grid size of 0.7, the PBCP classification tolerance is approximately the same for both particle sizes at ~5%. As a result, it can be concluded that the current bonding model suggests that a similar PBCP value is expected to be sufficient for bonding across all particle sizes. Physically, this suggests that the oxide layer breakage over a similar percentage of the contact interface is required irrespective of particle size. This further allows the PBCP from tests with the finest 0.7 μm grid size to serve as a consistent measure of bond quality for all particle sizes. The predicted PBCP is also observed to be appropriately convergent as the number of initial particles per grid is increased with each grid size. From this result, it can be concluded that a grid size of 0.7 is sufficient for producing a consistent measure of bond quality for different-sized particles. A moderate number of initial particles per grid of approximately 20 is recommended in order to avoid potential issues caused by too few particles per grid as deformations occur, however fewer particles per grid will still yield usable results. Figure 5.6 shows the logistic regression tolerances and identified bonding boundaries for both particle sizes along with their intersection point for the 1.5/0.35, 1.0/0.25 and 0.7/0.175 grid configurations like in Figure 5.3. Bonding boundaries identified with other grid configurations have not been shown here for brevity but are all similar in shape and can be found in Appendix B.

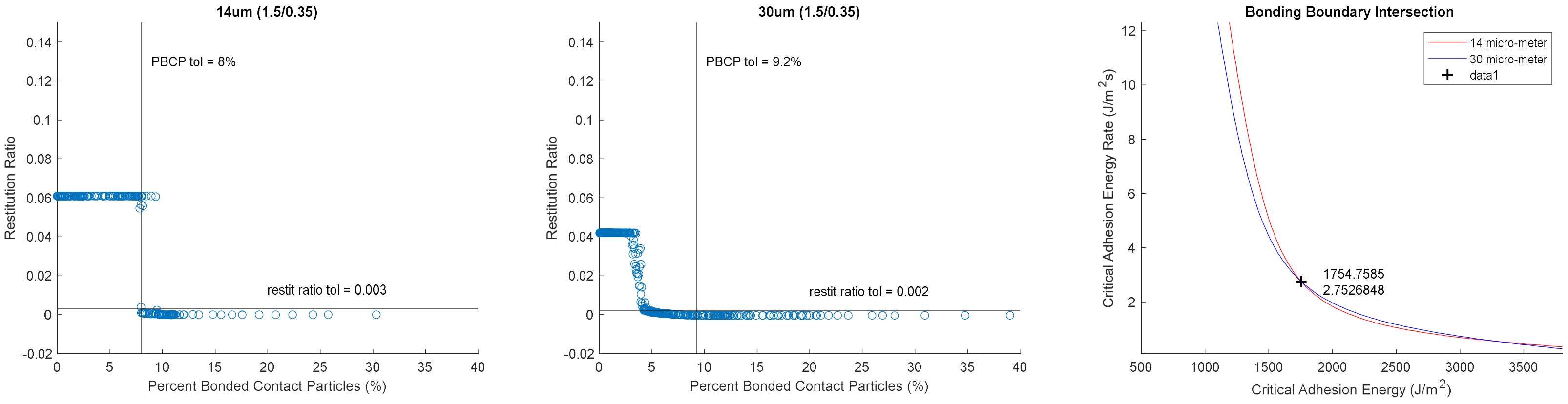
14um (1.5/0.35)
PBCP tol = 8%
restit ratio tol = 0.003
Restitution Ratio
Percent Bonded Contact Particles (%)
30um (1.5/0.35)
PBCP tol = 9.2%
restit ratio tol = 0.002
Restitution Ratio
Percent Bonded Contact Particles (%)
Bonding Boundary Intersection
14 micro-meter
30 micro-meter
data1
1754.7585
2.7526848
Critical Adhesion Energy Rate (J/m^2s)
Critical Adhesion Energy (J/m^2)

a)

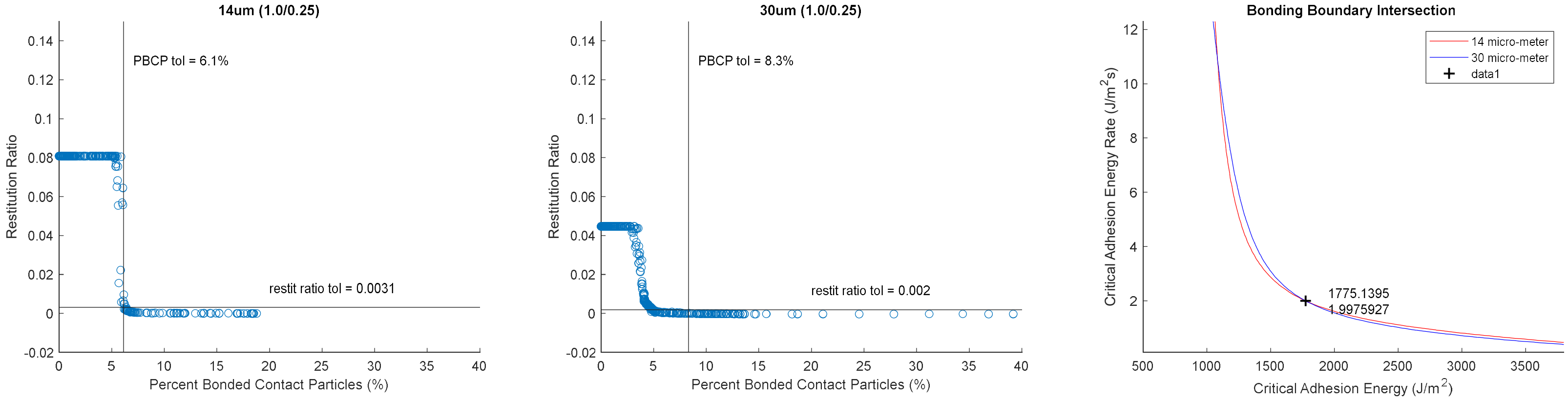
14um (1.0/0.25)
PBCP tol = 6.1%
restit ratio tol = 0.0031
Restitution Ratio
Percent Bonded Contact Particles (%)
30um (1.0/0.25)
PBCP tol = 8.3%
restit ratio tol = 0.002
Restitution Ratio
Percent Bonded Contact Particles (%)
Bonding Boundary Intersection
14 micro-meter
30 micro-meter
data1
1775.1395
1.9975927
Critical Adhesion Energy Rate (J/m^2s)
Critical Adhesion Energy (J/m^2)

b)

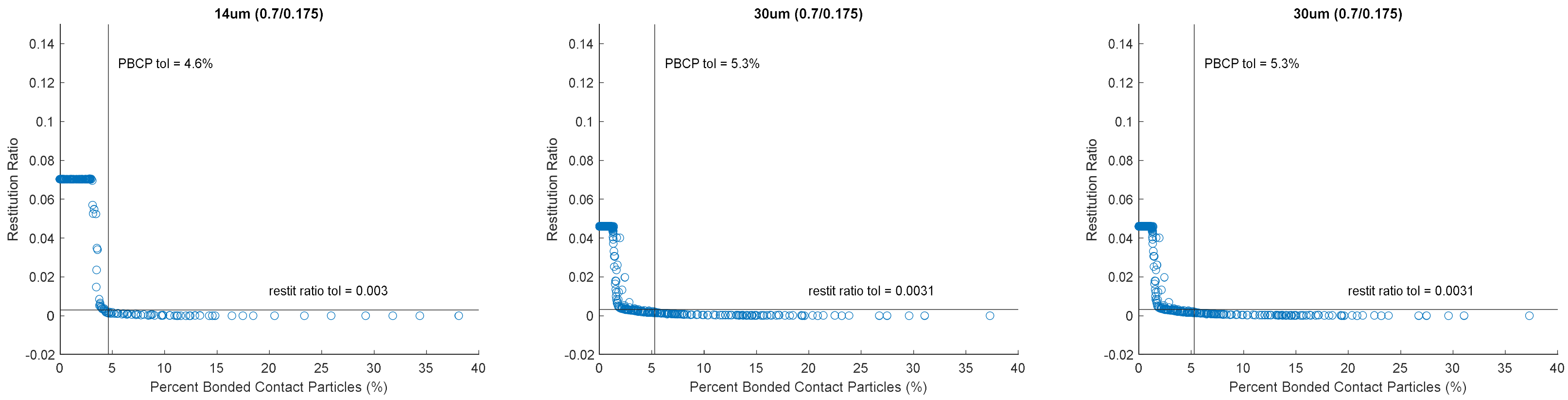

c)

Figure 5.6: Energy-based pressure independent bonding model simulation results showing the plots of restitution ratio vs. PBCP and bonding boundary intersection for 14 μm and 30 μm diameter Al particles determined with a) 1.5/0.35, b) 1.0/0.25 and c) 0.7/0.175 grid configurations.

Bonding boundary curves can be seen to be extremely similar to each other with each grid configuration similar to what was observed previously with restitution ratio and average D_{bond} tolerances. Although the range appears smaller, there still exists a large number of test results that had to be classified as not bonded despite having low enough restitution ratios. However, there now exists an argument with the PBCP perspective which did not exist with average D_{bond}. It is reasoned that the particles which meet the restitution ratio tolerance but not the PBCP tolerance may not have rebounded but also have not bonded sufficiently to have significant bond strength. The particle itself may have been affected by adhesion forces included directly in the simulation such that it has negligible rebound energy and low restitution velocity. However, it can be argued that physically there has not been sufficient jetting or oxide layer breakage to result in a fully bonded particle. Thus, the use of PBCP may not fully address the classification issues but at the very least, provides a quantifiable, physical metric that can be used to explain predicted material behavior.

5.1.3 Discretization Sensitivity

As was shown in the previous section, transitioning to a PBCP perspective is useful in classifying test results as bonded or not and providing a quantifiable, physically-based measure of bonding. Although the boundary intersection points were previously presented in Figure 5.5, all the precise bonding boundary curves predicted were not shown for brevity. Instead, as part of a more explicit analysis of the discretization sensitivity of the proposed model, the bonding boundaries identified using tolerances in Table 5.2 for all nine grid configurations and each particle size are presented in Figure 5.7. Note that grid sizes are grouped by color and the number of initial particles per grid (i.e. particle spacing) by line type, with more particles per grid being represented by a higher density line.

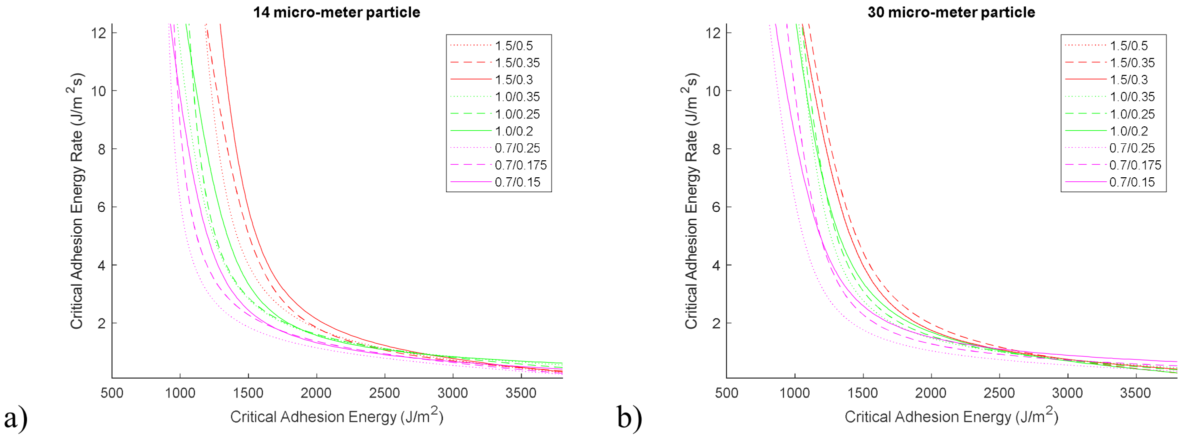

Figure 5.7: Plots of bonding boundaries of the a) 14-μm particle and b) 30-μm diameter particle identified using all grid configurations.

It can be seen from these plots that by basing the model parameters on adhesion energy, and in particular with the inclusion of the $DCell$ grid size regularization measure, a similar bonding boundary is able to be identified using all tested grid configurations. Overall, it can be seen that a similar bonding boundary shape is identified in each particle for each grid size, with different grid sizes resulting in slight differences. Although these small differences exist, some variation with grid or element size should be expected with any numerical method and the current result is considered acceptable. Smaller increments in the range of tested model parameters may lead to improved boundary accuracy however the current tests are deemed sufficient for validating the discretization sensitivity of the model. Ultimately, this suggests that the same set of calibrated parameters can be reasonably applied to simulations with any grid configuration that has sufficient initial particles per grid to produce accurate results. These results confirm that an approximate initial particle per grid value of 8 or 20 appears to be sufficient even with the severe deformations seen in CS.

The grid size in particular is noted to play a more significant role in the predicted deformations and bonding boundaries compared to particle spacing. To demonstrate this, plastic strain contours of the 14-µm particle using 1.0/0.25, 1.0/0.2 and 0.7/0.25 grid configuration are shown in Figure 5.8. These tests were conducted with identical bonding model parameters and other process parameters with the only difference being particle spacing or grid size, in order to explicitly investigate their effects on the overall simulation.

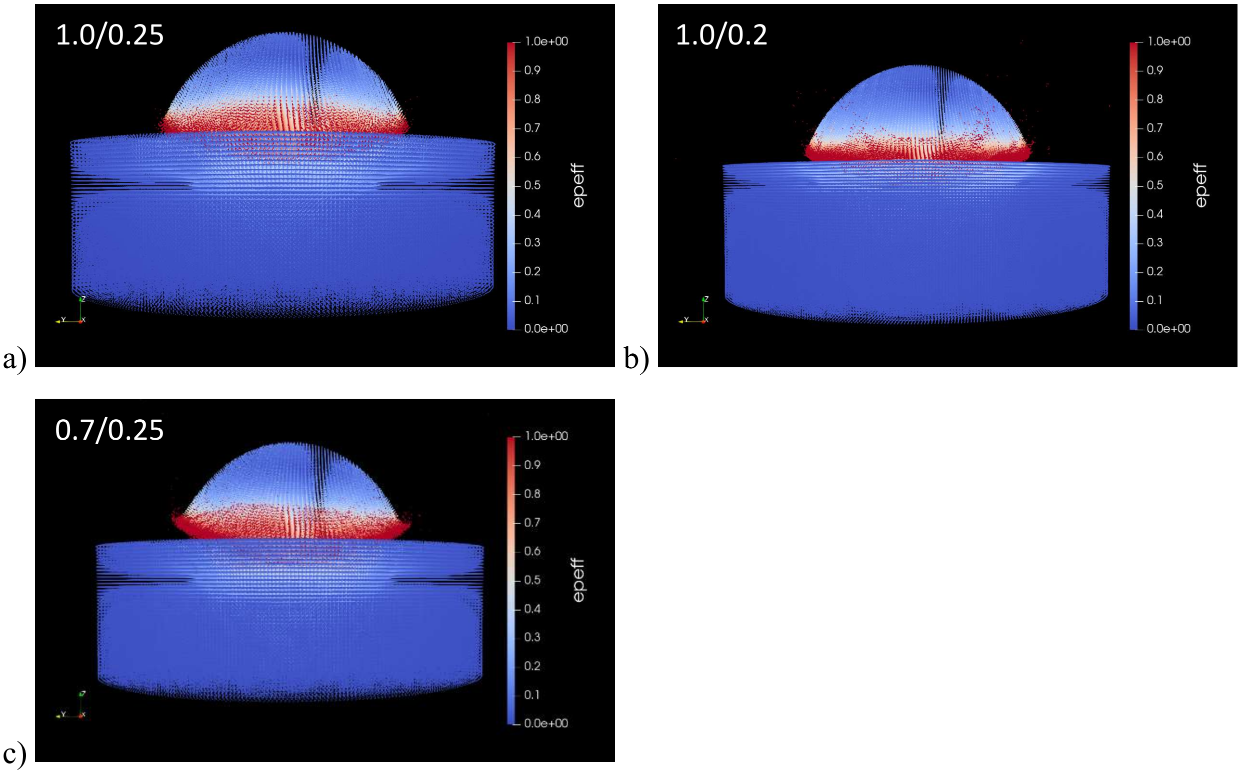

Figure 5.8: Contour plots of effective plastic strain using an a)1.0/0.25, b)1.0/0.2 and b) 0.7/0.25 grid configuration, explicitly comparing the effects of grid size and particle spacing on material behavior.

From these contours, it is clear that grid size appears to have a noticeably greater effect than particle spacing on the amount of plastic strain and material jetting predicted at the contact interface. Between Figure 5.8a and 5.8b, there is hardly any difference in particle shape and only a slightly greater number of ejected material points, which is expected since more points are present. However, between Figure 5.8a and 5.8c, the shape of the impacted particle has visibly changed in addition to showing increased material jetting and higher strains, giving a more accurate representation of bonded particle behavior relative to experimental evidence. The greater influence of grid size on test results in MPM is in line with results obtained by Sinaie et al. [69], who also demonstrated that grid size plays a greater role than particle spacing on simulation outputs.

5.1.4 Time Step Scaling Factor

Based on the above results and discussions, the calibrated model parameters are taken to be the bonding boundary intersection achieved using a 0.7/0.175 grid configuration with restitution ratio and PBCP as the classification tolerances for logistic regression. With this 0.7/0.175 grid configuration, a series of calibration tests are performed to determine the optimal time step size. Time step scaling factors of 0.1, 0.2 and 0.4 applied to the critical time step size of a 0.5-μm grid are tested for the 14-μm particle size using identical PCBP and restitution ratio classification tolerances for all cases. The identified bonding boundary curves are shown in Figure 5.9. Line density increases as time step size is reduced with the thick green line representing the test conducted with the 14-μm particle and a 0.05 scaling factor, to be used as a reference for convergence.

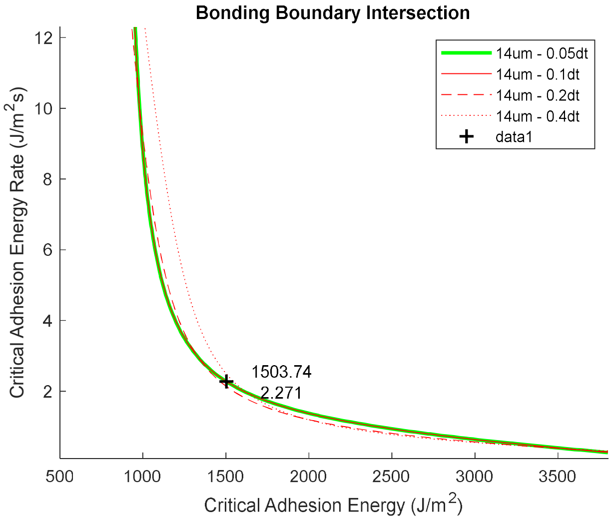

Figure 5.9: Bonded boundary curves achieved using a 0.7/0.175 grid configuration and time step scaling factors of 0.1, 0.2 and 0.4. Labeled is the intersection point of the bonding boundaries for the 14 and 30 μm particles with a 0.1 scaling factor.

From these plots, it is clear that time step size only slightly influences the bonding boundary predictions, although noticeable differences appear at the largest tested time steps. Although a time step scaling factor of 0.2 is also valid, a time step scaling factor of 0.1 is used for the most part to ensure convergence during model calibration testing. The predicted boundary with a 0.1 scaling factor is in fact identical to the one predicted with 0.05 given the testing resolution. The precise critical surface adhesion energy (G_c) and energy rate ($\dot{G}_c$) values are identified to be $1503.74 J/m^2$ and $2.271\ J/m^2s$ using a 0.1 time step scaling factor for both particle sizes. This model parameter combination will be used in the following section as the final calibrated parameters in order to evaluate model performance.

5.2 Calibrated Model Performance

5.2.1 Predicted Material Behavior under Subcritical and Critical Velocity Impacts

In order to evaluate the performance of the calibrated model in accurately predicting material behavior, the predicted strain contours are compared with what has been observed experimentally. The material ejection observed is in fact as a result of an artificial fracture as no explicit fracture or damage criterion has been included within any simulation in this thesis. Therefore, the material ejections observed may be said to be simply as a result of large deformations in the associated material points such that the ejected particles are considered like a separate body. Furthermore, in order to match the spatial and temporal dimensions listed experimentally as closely as possible, the time step scaling factor has been increased to 0.2 for all simulations to ensure 1-to-1 comparison. The differences from increasing time step size by this degree are considered negligible as shown in Section 5.1.4.

In any case, the ability of the proposed energy-based bonding model within an MPM framework can be seen in Figure 5.10 to quite accurately represent the cloud of fragmented or ejected material observed experimentally [12]. Note that in order to minimize computation time, the simulations only start upon initial impact of the particle or t_o. Experimental results by Hassani et al. [12] have been reproduced and relabeled according to the time of initial contact, t_o. The specific images which directly correlate to simulations have been boxed in green while the contours themselves have been labeled with timestamps to match the times in the appropriate experimental images. Figure 5.10a shows the plots of effective plastic strain predicted with the calibrated bonding model for a 45-µm particle with a 0.7/0.175 grid configuration impacted at a velocity of 550 m/s. This matches the experiment setup by Hassani et. al [12] for Al-on-Al impacts of a 45-µm sized particles as shown in Figure 5.10b. It can be seen in both Figure 5.10a and 5.10b that although the particle undergoes large plastic deformations, there is almost no predicted or observed material jetting when the impact velocity is subcritical.

Meanwhile, as velocity is increased to near or above critical values, significant material jetting phenomenon starts to be observed both numerically and experimentally. Figure 5.10c shows the simulation results of a 38-µm Al particle impacting on an Al substrate at a supercritical velocity of 780 m/s while Figure 5.10d is the experimental observations of a 38-µm Al particle impact under similar conditions made by Hassani et al. [12]. It is clear from these images that only with the occurrence of sufficient material jetting does bonding occur both numerically and experimentally. An additional contour has been included at 120 ns post impact in Figure 5.10c to show that the powder particle has been modeled to be fully bonded with the substrate. This demonstrates that the current adhesion model within a MPM framework is able to accurately capture the material jetting phenomenon, relate it to successful bonding and directly include the bonding effects within a simulation.

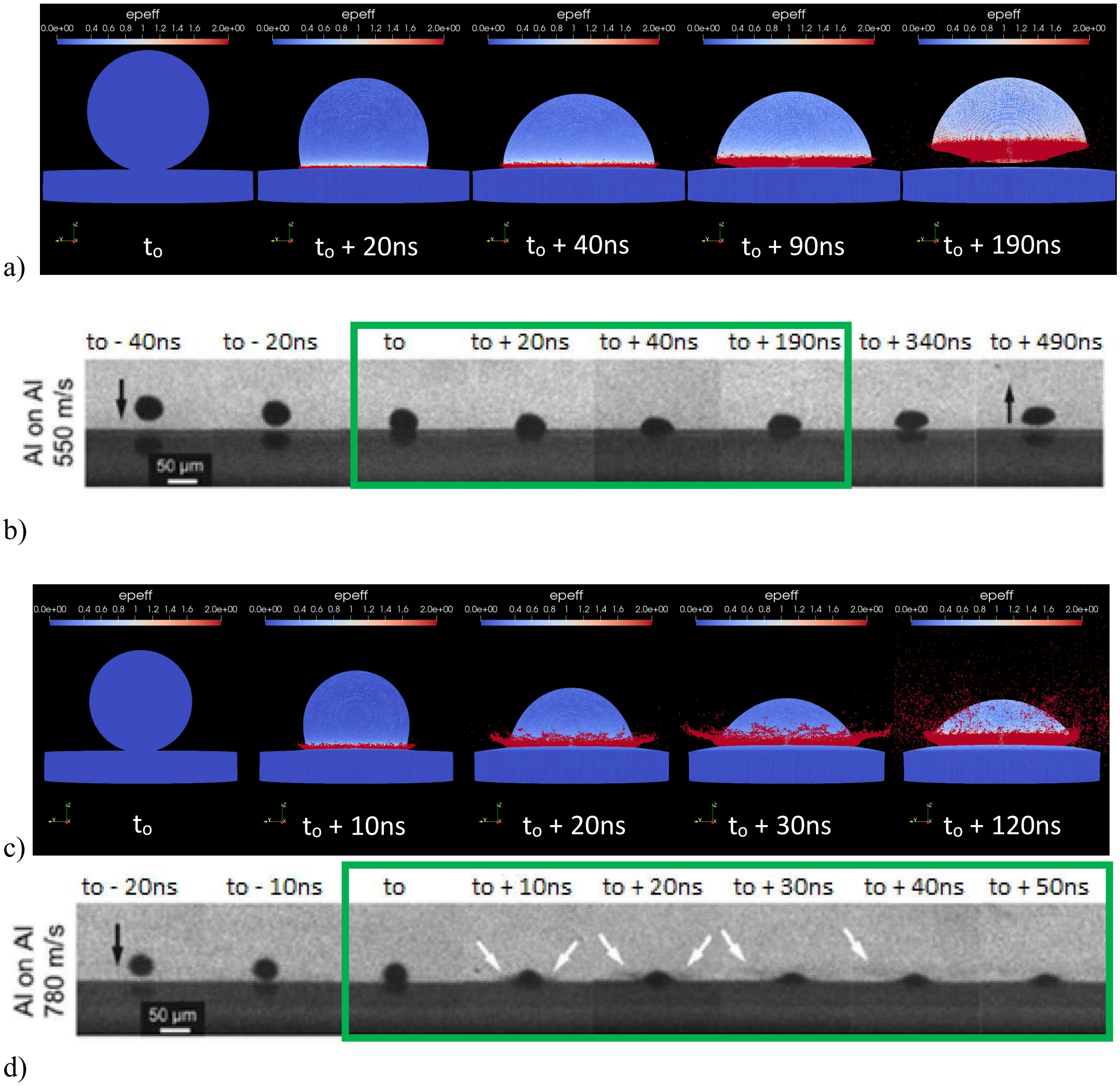

Figure 5.10: Comparison of subcritical velocity material behavior from: a) simulations of a 45-µm particle sprayed at 550 m/s and b) experimental observations of a 45-µm particle sprayed at 550 m/s [12]. Also shown are critical velocity material behavior from c) simulations of a 38-µm particle sprayed at 780 m/s and d) experimental observations of a 38-µm particle sprayed at 780 m/s [12].

To note is that with the present model, it is predicted that it is primarily material from the powder particle which is ejected while the substrate demonstrates little jetting behavior. This aligns with results obtained by Hassani et. al [9] using a CEL approach but opposite to results by Yu et. al [17] whose Eulerian simulations predicted heavy jetting in the substrate. Material properties of the particle and substrate have been shown to affect which body contributes more towards jetting [44]. However, accurately modeling from which body the ejected particles are from may also be affected by the normal vector definition and thus, require future improvements to the overall MPM contact algorithm to be fully addressed.

5.2.2 Critical Velocity Prediction

In order to test the performance of the calibrated MPM bonding model, a series of tests are conducted using a range of particle sizes to evaluate the ability of the model to predict critical velocity. Particles and substrates with dimensions listed in Table 5.3, such that they are of reasonable size relative to each considered particle size. All critical velocity prediction tests are done with a 0.7/0.175 grid configuration and the previously calibrated $G_c = 1503.74 J/m^2$ and $\dot{G}_c = 2.271\, J/m^2 s$ values for the bonding model parameters. As the experimental critical velocities are 810 m/s and 770 m/s respectively for a 14-µm and 30-µm diameter Al particle impacts on same material substrate, the range of tested initial impact velocities are set to be between 750-830 m/s. Only particles sizes between 14 and 30 µm are considered as the current bonding model parameters have been calibrated with experimental data from this range. Consideration of larger particles remains valid as shown previously in Figure 5.10, however there may be loss of accuracy in the predicted critical velocity.

Table 5.3: Approximate particle and cylinder substrate dimensions used to test model performance in predicting critical impact velocity.

Particle Diameter (µm)	Substrate Diameter (µm)	Substrate Height (µm)
14	30	10
18	36	10
22	44	10
26	46	10
30	50	10

Plots of the PBCP results at 80 ns post-impact for each particle size are shown in Figure 5.11, with solid vertical lines showing the approximate critical velocity assuming a linear relation between particle size and critical velocity. Note that the experimentally measured critical velocity of the 14 and 30 µm particles themselves are subject to a potential 2% measurement error [9]. Thus, the solid horizontal shows the average PBCP within the 2% error envelope for each interpolated critical velocity. It is clear that PBCP is steadily increasing as impact velocity is increased with every particle size. By observation from the average PBCP, it appears that a PBCP of about 4.6%-5.4% can be identified as the threshold for bonding assuming a linear relation between particle size and critical velocity with the current level of discretization.

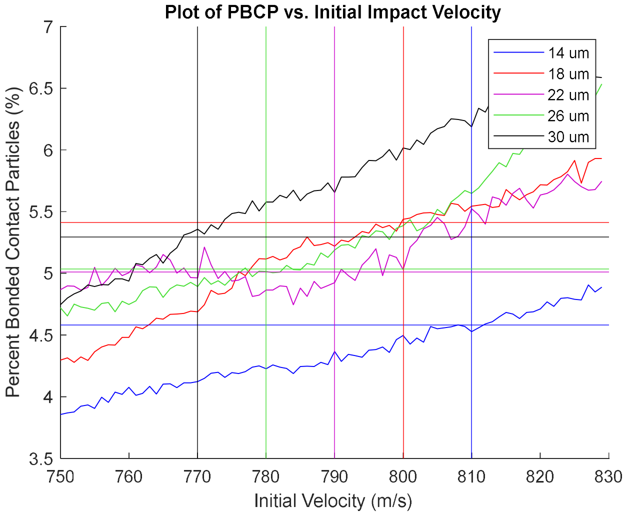

Figure 5.11: Plots of PBCP vs. initial particle velocity. Vertical lines label the critical velocity approximated by a linear size-to-velocity ratio and the horizontal line identifies the average PBCP of data points within a 2% error envelope.

In order to show further evidence of complete bonding at a precise impact velocity, it is natural to also observe the average particle restitution velocity, v_{rest}. Within a simulation, bonding can be quantified by the final steady state velocity of the particle, as a low enough v_{rest} represents a bonded particle in the simulation. However, there is a significant amount of material point jetting that occurs in every simulation as demonstrated in Figure 5.12, showing the effective plastic strain of the 14-µm and 22-µm diameter particle impacted at 810 m/s. The excessive material jetting in the 22-µm particle reflects that the 810 m/s impact is above the critical velocity limit necessary for bonding.

Nevertheless, the majority of these ejected material points have velocity magnitudes in the hundreds of m/s with some even reaching over 2000 m/s. If all are considered, these ejected particles can disproportionately affect the v_{rest} calculation and result in an inaccurate representation of the overall average particle rebound velocity. Furthermore, there can also be a different proportion of jetted material points for different particle sizes, resulting in inconsistencies between different particle/substrate sizes. As such, a filter is applied where only material points with a velocity magnitude lower than 60 m/s are considered in the calculation of the bulk particle v_{rest}. This velocity is selected intuitively as it is approximately the maximum restitution velocity in a fully rebounded particles for all tested sizes. Since only normal impacts are considered, the vertical or z component of these velocities are then averaged to give a consistent measure of overall particle restitution velocity.

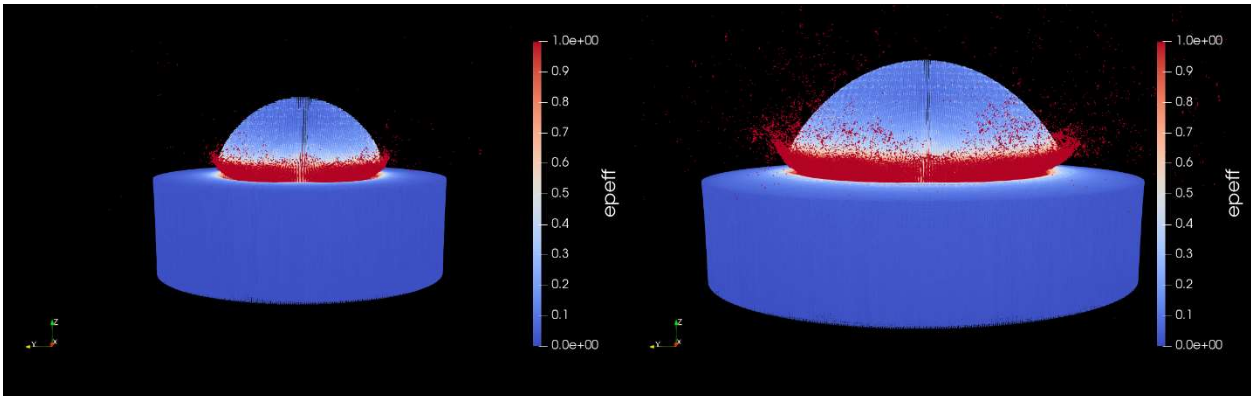

Figure 5.12: Contour plot of effective plastic strain for a) the 14-µm and b) the 22-µm diameter particles impacted at 810 m/s.

Figure 5.13 shows the plots of overall particle restitution velocity v_{rest} superimposed with the PBCP plots with respect to initial velocity for each tested particle size. By these results, it is clear that in the tests with every particle size, there is a clear decrease in v_{rest} as the impact velocity is increased. Tolerances of 5.0% for PBCP and 0.6 m/s for v_{rest}, shown by dashed blue and orange lines respectively, are assumed wherein the precise critical velocity is the lowest impact velocity in which both conditions are satisfied. Identical tolerances are used for all tests with the exception of the 14-µm particle which used tolerances of 4.8% and 0.9 m/s as the restitution velocities were slightly higher and PBCPs slightly lower on average than other particle sizes. This small adjustment to a tolerance is considered acceptable within the simulations and may be attributed to numerical error associated with the MPM algorithm and level of discretization. It may also possible that smaller particles require slightly less PBCP to be bonded overall as their kinetic energies are lower, however studies at finer grid configurations with an improved MPM implementation should be done to confirm this. In any case, the predicted critical velocities by the above criteria are labeled by solid green vertical lines in Figure 5.13. Critical velocities assuming a purely linear relation between particle size and critical velocity are shown by solid black vertical lines.

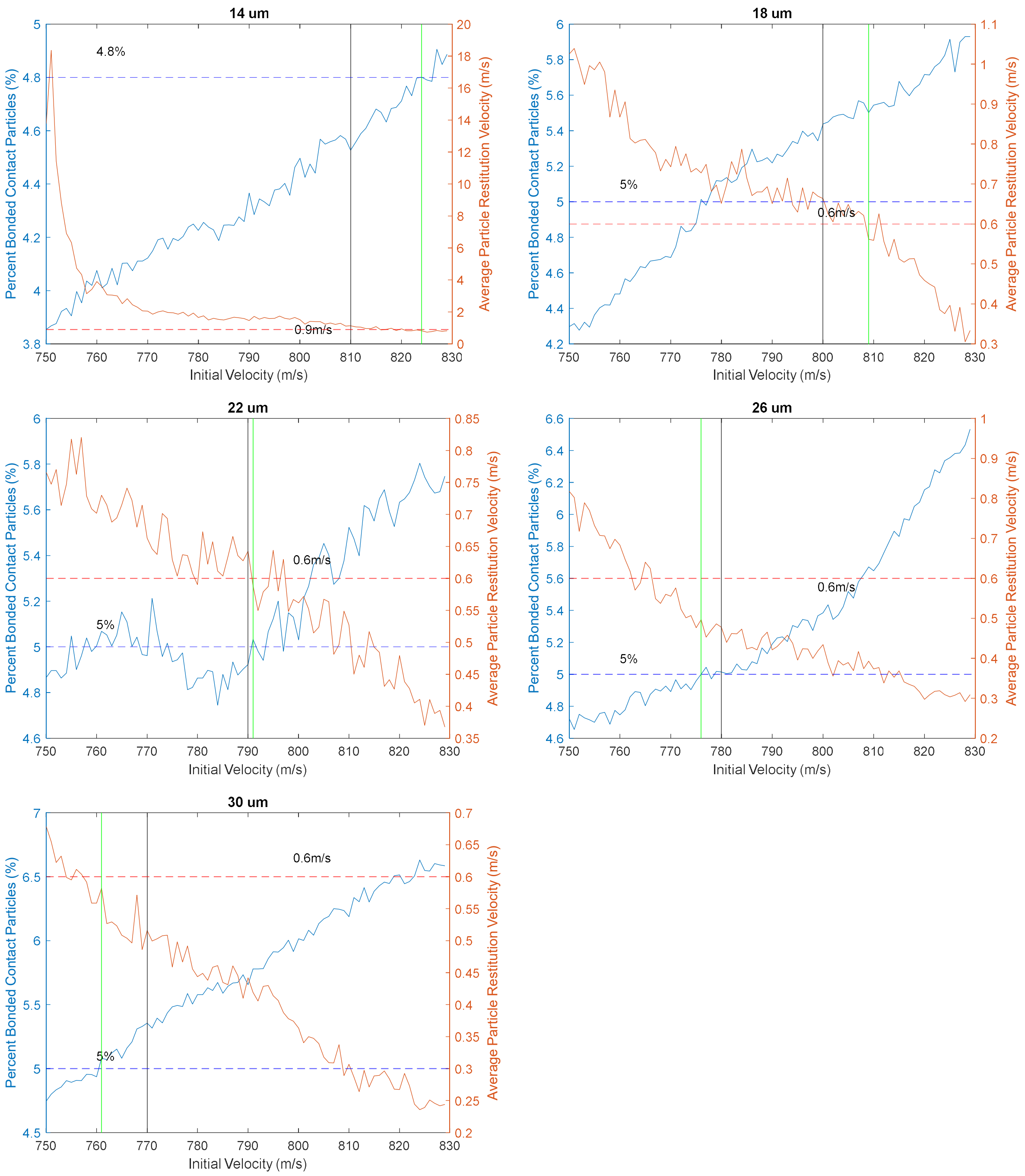

Figure 5.13: Plots of overall particle restitution ratio vs. initial particle velocity superimposed with PBCP vs. initial velocity plots of for all tested particle sizes. Vertical green lines show an estimate of the predicted critical velocity for each particle size using the tolerances as indicated by the dashed horizontal lines. Vertical black lines indicate the predicted critical velocities assuming a purely linear relation between particle size and experimental critical velocity.

Table 5.4 lists the predicted critical velocities for all particle sizes along with the respective PBCP and v_{rest} at this velocity. From this table, it is clear that PBCP and v_{rest} are very similar at the predicted critical velocities across all particle sizes. Furthermore, the critical velocities themselves follow the trend seen in experiments with larger particles exhibiting lower critical velocities. The PBCP values at the predicted critical velocities range from 4.8 – 5.5 % at the predicted critical velocities for all particle sizes while restitution velocities range from approximately 0.5 – 0.8 m/s. Figure 5.14 labels all the predicted critical velocities along with their associated particle sizes in a plot of PBCP vs. impact velocity to reveal the relationship between predicted critical velocity and particle size. Results from the present model suggests that critical impact velocity decreases linearly as particle diameter is increased.

Table 5.4: Table of predicted critical velocities for particles of various sizes, along with their associated PBCP and restitution velocity values.

Particle Diameter (μm)	Predicted Critical Velocity (m/s)	Percent Bonded Contact Particles (%)	Average Particle Restitution Velocity (m/s)
14	824	4.80	0.8156
18	809	5.50	0.5620
22	791	5.03	0.5884
26	776	5.00	0.4964
30	761	5.08	0.5815

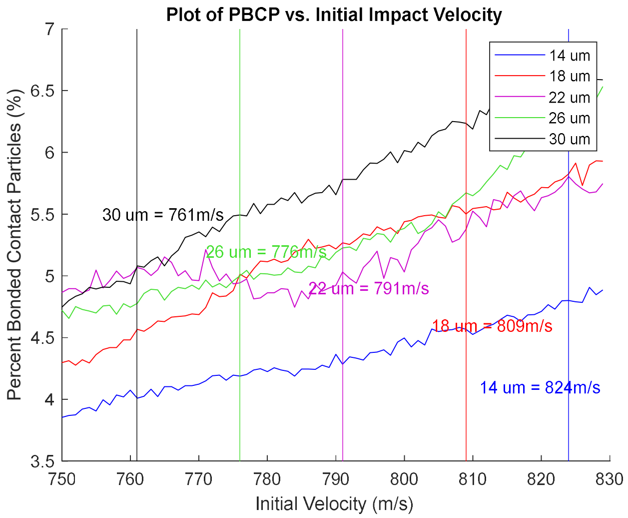

Figure 5.14: Plot of PBCP vs. initial velocity with vertical lines indicating the predicted critical velocities for particle sizes ranging from 14 to 30 μm diameter.

5.2.2 Two-Particle Impacts

In this section, the performance of the proposed bonding model will be briefly examined in the simulation of multiparticle impacts. Initially, two 14-μm diameter Al particles will be considered both with initial velocities of 810 m/s. The first powder particle will begin in contact with the substrate with the centre of the sphere located 7-μm above the substrate while the second particle is initialized with its center located 30-μm above the substrate. A total of four tests using a 0.7/0.175 grid configuration will be conducted with the second particle being set at

0, 2.5, 5 and 7.5 μm offsets in the x-direction from the first impacting particle. By this analysis, the ability of the current MPM bond model to accurately simulate the multiparticle deformations and simple particle-particle interactions will be evaluated.

Figure 5.15 shows the evolution of plastic strain at 30 ns increments across the first 90 ns post-impact for two 14-μm particle impacts at critical velocity with varying levels of centre offset. From these plots, it is clear that the amount of offset has a significant impact on the deformation behavior of each body. In Figure 5.15a it is assumed that the second powder particle impacts directly onto the center of the previously bonded particle. As a result, both particles can be seen to undergo an axisymmetric deformation. Of course, such an ideal scenario is rarely expected in actual processing conditions. Instead, two-particle impacts at offsets of 2.5, 5.0 and 7.5 μm to each other are shown in Figure 5.15b, c, and d, respectively. It can be seen that with an offset, the latter impacted particle appears to slide and shear across the top surface of the first bonded particle. As a result of this, material points can be seen to be sheared off along the particle-particle interface resulting in an ejection of material that is proportional to the amount of offset. This effect is more severe the greater the offset is, to the point that the second particle slides off and begins to shear off and de-bond from the first particle with a 7.5 μm offset at 90 ns post-initial particle impact.

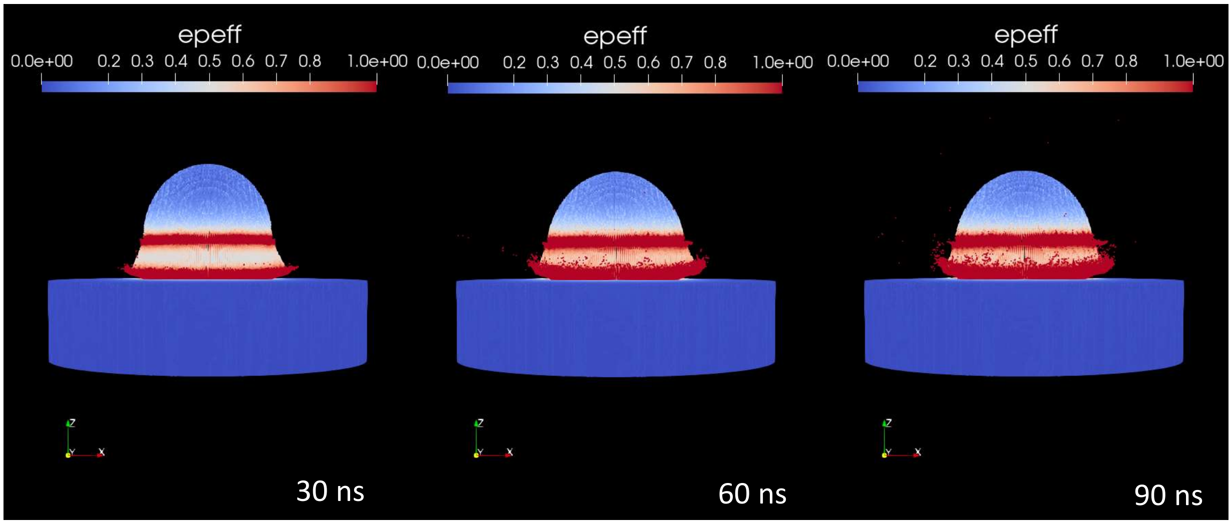

a)

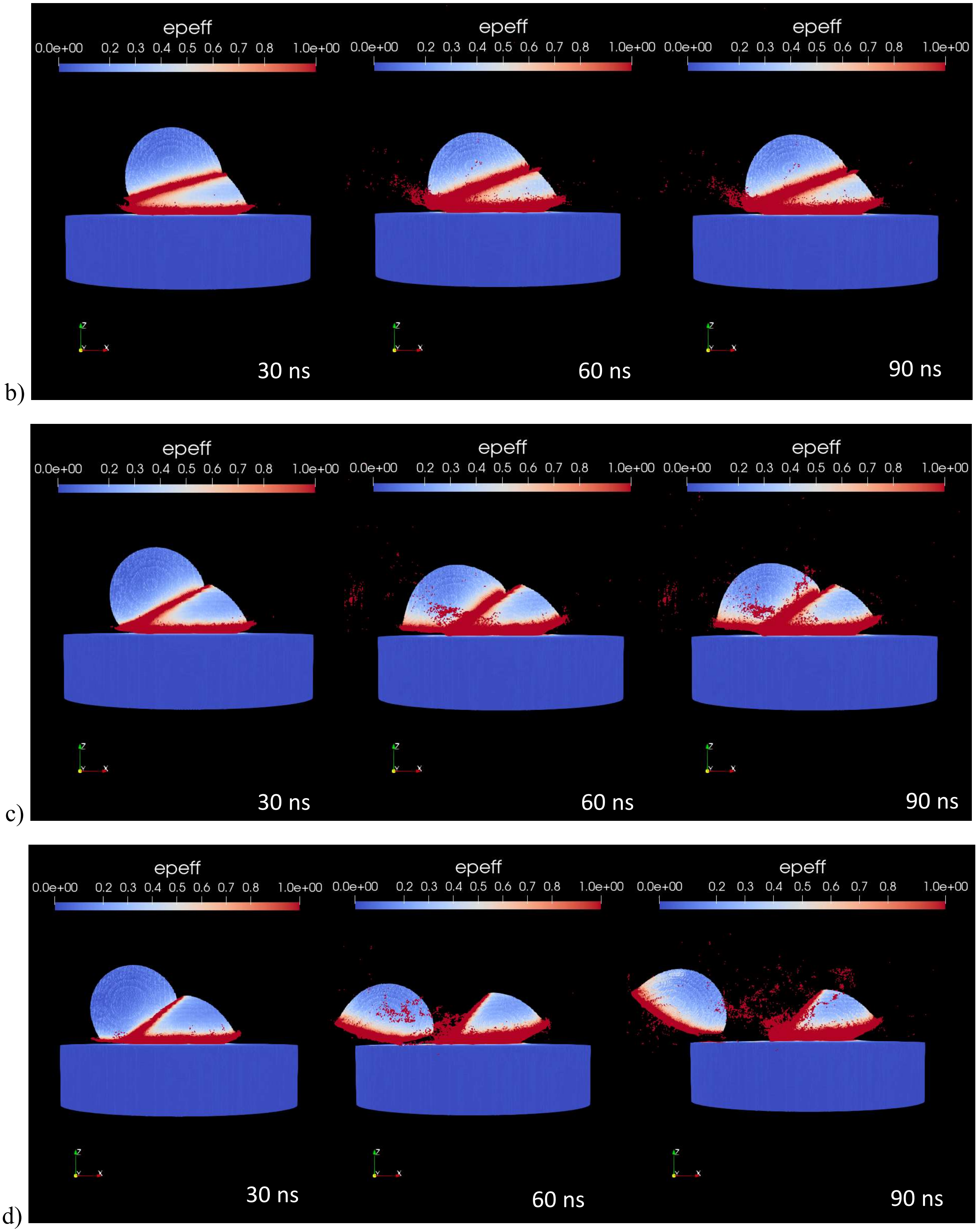

Figure 5.15: Contour plot of effective plastic strain from simulating multiparticle impacts at 30 ns increments, with an offset of a) 0-μm, b) 2.5-μm, c) 5-μm and d) 7.5-μm offset between the centres of two 14-μm diameter spherical Al powder particles.

In terms of the simulation of particle-particle interactions and overall bond quality between the bodies, Table 5.5 lists the predicted PBCP within the whole system associated with the different offset tests and overall restitution velocity with ejected particles filtered out. Note that some particle velocities may not have been filtered out completely due to the increased jetting from subsequent particle impacts, meaning the restitution velocities may be slightly different from the previous single-particle tolerance of ~0.6 m/s. In any case, bonded particle restitution velocities are still reasonably low and are not considered a problem in the more aligned impacts. Based on the bonding PBCP criterion from critical velocity predictions, a PBCP of at least 4.8-5.0% should be expected for particles to be considered bonded.

Table 5.5: Predicted overall PBCP values of two-particle impact tests to be used as an indirect measure of bond quality. The average restitution velocity filtered to only consider material points with velocities ≤ 60 m/s for each powder particle are also listed as further insight on bonding result.

	0-µm Offset	**2.5-µm Offset**	**5.0-µm Offset**	**7.5-µm Offset**
Overall PBCP (%)	5.73	5.47	4.71	3.91
Average Top Particle Z-dir. Velocity (m/s)	2.02	1.65	6.06	16.24
Average Bottom Particle Z-dir. Velocity (m/s)	1.24	0.92	0.94	-0.53

From Table 5.5, it is clear that subsequent particle impacts that are near-alignment actually serve to improve the adhesion/cohesion quality of the formed coating, resulting in PBCPs well over the 5.0% tolerance for a bonded particle. Physically, this can be attributed to the peening effect and increased contact pressure applied by the subsequent particle impacts which have been observed experimentally to enhance metallurgical bonding and mechanical interlocking effects [91]. Meanwhile as the impacts are at greater offsets, it can be seen that the PBCP of 4.71% and 3.91% reflects the reduced overall bond quality with a 5.0 and 7.5 µm offset, respectively. In fact, with the largest 7.5 µm offset, the top particle which impacts later has clearly rebounded fully based off the restitution velocity and the contours in Figure 5.15d. Note that all PBCP values presented are with relation to the overall system as the main purpose of this measure is to evaluate the bond quality in the overall coating/part. Specific PBCP for bonding between particles has not been explicitly investigated although it is likely to be different given that subsequent impacts occur against a heavily deformed particle rather than a pristine substrate. Quantifying a PBCP for each individual body may be looked into further as part of future work as it will also be particularly influenced by improvements to the overall MPM contact implementation.

5.2.3 Large-scale Particle Impacts

In adjusting the in-house MPM code for two-particle impacts, it has also been generalized to accommodate for impacts of any number of particles. To demonstrate the initial validity of the bonding model implemented in the MPM without excessive computational costs, Figure 5.16 shows the plots of effective plastic strain of ten 14-μm sized Al particles impacting on an Al substrate at their critical velocities, with a grid configuration of 1.0/0.35. Each particle is placed at randomized locations and heights to simulate different impact times, without initial overlap. Through this simulation, it can be seen that the present numerical model is able to accurately model impacts of large numbers of powder particles, which is relevant for simulation of coating buildups.

Previously, Zhou et al. [91] noted from their Lagrangian simulations that the interactions between material jets in multiparticle impacts are beneficial for bonding. In the current MPM study, although most particles which were impacted at their critical velocity bond successfully, observations of the particle-particle interactions reveal that the material ejected from bonded particles can inhibit bonding from subsequently impacted particles in its vicinity. In particular, the particle circled in yellow in Figure 5.16 can be seen to be rebounding as its successful bonding was compromised by the ejected material points of the previously bonded particles around it. In terms of the physical process, this may be related to the effects of spray speed, scan speed and other parameters which may affect parameters such as deposition efficiency and porosity in a cold spray coating or part.

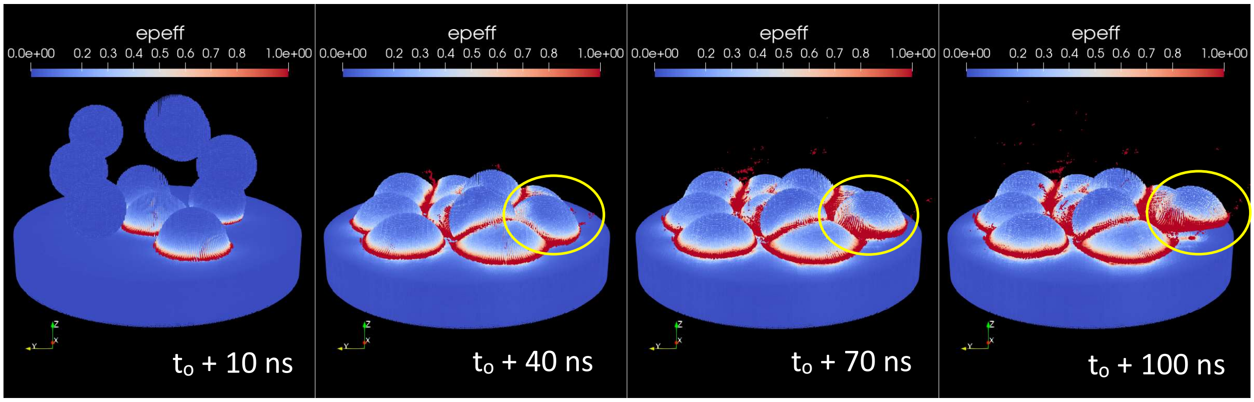

Figure 5.16: Effective plastic strain in impacts with ten 14-um Al particles on an Al substrate demonstrating the ability of the model to simulate particle-particle interactions and cohesion. The labeled particle can be seen to have debonded due to the ejected material points from the previously bonded particles around it.

However, it is important to note here again the influence of the unit normal vector calculated for multiparticle and multimaterial impacts. Firstly, as was mentioned in Chapter 3.5.4, the collinearity condition is preserved by explicitly setting the normals of the slave ("particle") body $\hat{n}_{iI}^{s}$ to the opposite of that of the master ("substrate") $\hat{n}_{iI}^{m}$. However, in multiparticle simulations, each body may both be considered the "particle" and "substrate" within a single time step which increases the complexity of normal vector calculations. For simplicity, the current multiparticle implementation randomly assigns each body a number however with the substrate always being the highest numbered body. It then always takes the normal vector of the higher numbered body as the contact normal. Thus, for a body i and body j that have come into contact, the normal vector $\hat{n}_{iI}^{\max(i,j)}$ is taken as the normal vector. Such an arbitrary normal vector selection does not lead to good accuracy in the MPM, where it has been shown that the interfacial energy density can vary significantly using traditional, grid-based normal vector definitions like the one used in this thesis [74]. Overall, results have been shown to be sensitive to the contact interface location and orientation relative to the computational grid as well.

Improvements to the MPM contact implementation will be required in the future in order to develop an accurate bonding simulation of multiparticle impacts. Nairn et al. [68] have recently developed a method using logistic regression solved by non-linear least squares which penalizes points as a function of their distance from a preferred separation line is able to address this issue well. Their inclusion of logistic regression and a separation criterion improved the overall accuracy of the contact algorithm in MPM, however it has yet to be validated up to the extreme strains seem in CS. This has not been implemented in the current work and the performance of the proposed bonding model is simply evaluated in a basic MPM implementation with the MVG normal vector definition in single particle simulations and arbitrary body mass gradients in multiparticle simulations. Further improvements to the normal vector definition will be necessary in the future ensure accuracy in large-scale simulations, likely also requiring a full recalibration of the bonding model.

5.3 Comparison with Experimental and Other Numerical Results

5.3.1 Bond Initiation Site Analysis

To examine where bonding initiates more explicitly, contour plots of $D_{bond}(\boldsymbol{x}_p)$ values in each material point for the 14 μm diameter particle using both strain and energy-based bonding models are shown in Figure 5.17. Only material points with a $D_{bond}(\boldsymbol{x}_p) > 0.7$ are shown in a top-down view of the contact interface for clear visualization of bonded particle distribution. For the sake of consistency, strain-based model tests are reconducted using a 0.7/0.175 grid configuration. With this configuration, there is a larger number of bonded material points which provides a more detailed visualization of the different bond initiation sites between models. Based on the time step scaling factor results, a scaling factor of 0.1 is also used.

The final calibrated model parameters are used for the energy-based bonding model while a critical strain and strain rate of 1.9 and 1350 μs^{-1} were selected for the strain-based model. Specific model parameter values are not important but are simply chosen such that a similar PBCP is predicted with both models. It should be noted the strain-based model does not incorporate an element or grid size measure within its formulation like the energy-based model, with using $DCell$. Consequently, its result is highly sensitive to discretization. Nevertheless, this does not affect the key feature under examination, which is the difference in distribution predicted by both models, for a similar number of bonded particles across the contact interface.

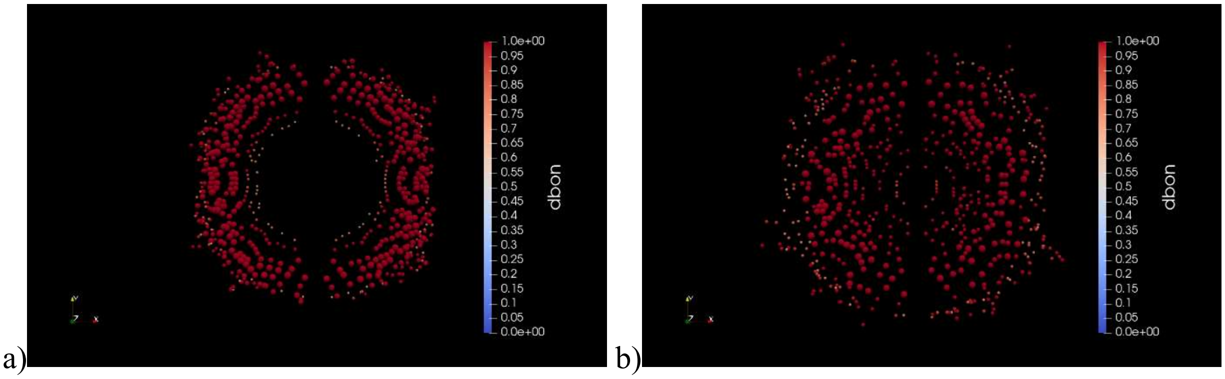

Figure 5.17: Plot of particle $D_{bond}(\boldsymbol{x}_p)$ values within a 14-µm diameter Al particle impacting on Al substrate at 30 ns post-impact using the a) strain-based and b) adhesion energy-based bonding models. Model parameters were chosen such that a similar total number of bonded particles was achieved. Only particles with $D_{bond}(\boldsymbol{x}_p) > 0.7$ are shown with particle sizes also being proportional to $D_{bond}(\boldsymbol{x}_p)$ magnitude above 1.

Due to the model parameters used, the number of material points with $D_{bond}(\boldsymbol{x}_p) > 1$ is approximately the same for both (~740) and constitutes a PBCP of approximately 5.3%. Although the global $D_{bond}(\boldsymbol{I}_g)$ value is limited to around a value of 1, individual particle values are observed to reach as high as 2.5. In Figure 5.17, all particles with $D_{bond}(\boldsymbol{x}_p) \geq 1$ are shown as an uniform red color however their magnitudes are further represented by the size of the spheres. Keeping this in mind, it can be observed that the distribution of these bonded particles has become more uniform throughout the contact interface. By switching to an energy-based model, many bonded particles have shifted towards the south pole of the particle rather than being concentrated near the perimeter of the contact surface where jetting occurs. The maximum particle $D_{bond}(\boldsymbol{x})$ values achieved are also noted to be lower with the energy-based model.

This result is in line with direct bond modeling results in an ALE framework performed by Rahmati and Jodoin [49] who concluded that bonding should initiate more towards the south pole of the particle and away from the jetting region. In their study, the effect of oxide layers was specifically considered through a surface expansion coefficient. With the current approach, although oxide layer effects have not been explicitly considered, the bond initiation site is still similar to studies where its effects have been directly studied. This demonstrates the benefits of the current adhesion energy-based model that uses a bonding activation criterion based on a threshold level of material jetting which is physically related to oxide layer breakage. The added stress component effect from using surface adhesion energy has appropriately reduced the effect of high shear strain but low stress material points in the jetting region on bonding.

5.3.2 Percent Bonded Area

Since results obtained with the finest tested grid size of 0.7 showed convergence in PBCP, the model parameters obtained a grid configuration of 0.7/0.175 and a moderate number of particles per grid is considered the final calibrated ones. With the assumption that each material point represents a similar material volume, the PBCP can be considered synonymous to percent bonded area. The percent bonded area for what constitutes a bonded CS particle can then be concluded to be ~5% for both the 14-μm and 30-μm diameter Al particles. Such a result is line with what has been determined theoretically by Sun et al. [60] who calculated the percent bonded area in Cu-Cu impacts to be ~5%. Schmidt et al. [90] also determined that bonded interface area can vary between 15% and 95% depending on how far above the critical velocity the impact occurs. Experimentally, such a low percent bonded area value is in fact reasonable as cross-sectional images of the particle-substrate interface has revealed that it is extremely imperfect prior to annealing and other post-processing techniques [92, 39, 93, 43].

Chapter 6 Conclusions and Future Work

6.1 Conclusions

In recent years, CS has emerged as a promising new technology for deposition of dense, high quality coatings that avoid many of the thermal-related issues inherent in traditional thermal spray techniques. However, due to the speed at which the impact process occurs, it has been difficult to identify through experimental work the precise bonding mechanisms. As an alternative, numerical modeling has been widely used however an accurate model is difficult given the large strains and strain rates in CS. The bonding phenomenon itself has typically only been identified through post-processing. The work presented in this thesis introduced a bonding model which directly includes the effects of the bonding phenomenon live within a simulation. This bonding model is implemented within a MPM framework which demonstrates significantly improved performance over traditional mesh-based FEMs for modeling the extreme conditions seen in CS. With the established relationship between material jetting, bonding and the critical velocity phenomenon, the model is formulated with the assumption that there exists a threshold level of material jetting which leads to proper bonding.

Initially, an attempt was made to identify this threshold level of jetting using the plastic strain experienced by the impacting powder particle. Although somewhat successful, several key issues were identified. Critically, significantly different amounts of plastic strain are predicted based on the level of system discretization. Such discretization sensitivity is highly detrimental to the overall robustness of any numerical model. Furthermore, the predicted sites of bond initiation do not align with what is expected from theory and assumptions made on the evolution law.

Alternatively, an energy-based bonding model is introduced where the threshold level of jetting is instead identified through the adhesion energy of the deforming powder particle. With the addition of regularization techniques from fracture modeling, the final adhesion energy-based model shows significant improvements, and a similar result is obtained irrespective of the precise system discretization. The site of bond initiation has also shifted to be more in line with theoretical expectations. The recommended grid configuration to be used in evaluating model performance is 0.7/0.175 as PBCP shows convergence at this level of discretization for different particle sizes. Final calibrated model parameters are $G_c = 1503.74 J/m^2$ and $\dot{G}_c = 2.271\, J/m^2 \mu s$ with a grid configuration of 0.7/0.175.

Using the energy-based bonding model, the critical velocity of arbitrarily sized Al particles impacting on same material substrates at ambient conditions has been able to be identified. Identification was based on the average particle restitution ratio as well as the PBCP, which is considered analogous to percent bonded area. PBCP further serves as a physically-based, indirect measure of bond strength or bond quality. The predicted PBCP resulting in a bonded particle of any size is found to be approximately 5% and is consistent with theoretical and experimental results from literature. Predicted critical velocities also follow the trends observed experimentally where the critical velocity of the particle decreases as particle size increases. Furthermore, the current model suggests a linear trend in critical velocity for Al particle sizes between 14-µm and 30-µm, for which the model has been calibrated to.

Performance of the proposed bonding model has also been evaluated briefly in terms of multiparticle impacts. As an initial step, the overall in-house code has been generalized to handle any number of particles but has only been shown with two and ten particle impacts. Initial results show that the overall bonding effects from multiparticle impacts such as material jetting are still able to be properly modeled using MPM, similar to in single-particle impacts. The current model also appears to be able to capture the particle-particle interactions modeling the coating build-up process. Further analysis shows that the current model is also able to successfully capture the peening effect from subsequent particle impacts which serve to improve bond quality.

6.2 Future Work

The MPM method has been shown to be much more suitable in modeling large deformation problems in comparison to mesh-based and other particle-based FEMs, however research into its applications in CS modeling has been limited. The present work constitutes an initial step in developing a direct bonding model within an MPM framework capable of providing accurate insight and predictions into material behavior and properties.

Currently, the present model is only able to directly answer the binary question of whether or not bonding has occurred within a material point. Although PBCP can potentially be used as a measure of bond quality it can at most only serve as an indirect measure. The current bonding model is entirely incapable of providing a quantitative prediction on bond strength in terms of an MPa measure. Further development towards a partial bonding model will be extremely beneficial particularly in providing an accurate prediction of bond strength. Using an energy-basis, a possible way forward could perhaps be geared towards using D_{bond} to determine the amount of plastic strain energy that is converted to adhesion energy over time. A similar process to Manap et al. [34] can then be performed to compare adhesion energy to rebound energy calculated from the recoverable (i.e. elastic) strain energy to determine bond quality. Alternatively, a force-based approach may be taken where D_{bond} instead defines the amount of contact pressure converted to bond strength. In any case, it will be valuable in the future to develop a model capable of directly outputting a bond strength or bond energy value to give a more direct measure of bond quality.

Aside from further model development towards bond strength prediction, it is also essential to validate the current model to different material types. Currently, only Al spherical particle impacts on Al substrates are considered. There exists a vast array of other materials and material combinations for which the current model must be validated. This may be extended to specifically include oxide layers within the simulation and investigate how different types and thicknesses of oxide layers affect bonding. The effect of different particle shapes, temperatures, impact angles, surface topologies and friction factors on critical velocity and bond quality may also be included as part of this investigation. Friction effects in particular may also be intimately linked with bond strength, as suggested by results from Wang et al. [54] from their study of oblique CS impacts.

Lastly, model performance in multiparticle and multimaterial impacts involving more than two particles should be tested in more detail. Specifically, this includes improvements to the overall MPM algorithm with consideration of different methods for determining the normal vectors used in contact/bonding calculations. In the MPM, determining a consistently accurate normal vector definition for various scenarios is an ongoing area of research. One such method has been proposed by Nairn et al. [68], which adds a separation distance criterion and logistic regression algorithm to contact calculations, although this has yet to be validated for extreme strains. In any case, it is critical in the future to include a method of identifying an accurate normal vector in order to produce a fully robust multiparticle MPM contact algorithm and bonding model. With proper implementation, overall coating properties like porosity and deposition efficiency may be able to be accurately predicted from large-scale simulations.

As an additional improvement to the overall MPM implementation, GIMP methods should be considered to reduce the inaccuracies from cell crossing noise. Similarly, adaptive remeshing of the computational grid, particularly around the material jetting regions can serve to address inaccuracies resulting from the numerical fracture. A recalibration of the model following the same procedure outlined in this thesis will be required after including these improvements to the overall numerical method. Ultimately, the goal should be to enable accurate simulations of a full coating buildup processes with a wide combination of materials along with comprehensive predictions of material properties for a given a set of process parameters.

References

[1] "History," Knowledge Podium & Business Expert Network.

[2] J. Villafuerte, "Plasma Transferred Wire Arc Process," Centerline (Windsor) Ltd., Windsor, Ontario, 2014.

[3] K. Yao, S. Chen, K. Guo, C. K. I. Tan, M. S. Mirshekarloo and F. E. H. Tay, "Lead-Free Piezoelectric Ceramic Coatings Fabricated by Thermal Spray Process," *IEEE Transactions on Ultrasonics Ferroelectrics and Frequency Control,* vol. 64, no. 11, pp. 1758-1765, 2017.

[4] A. Moridi, S. Hassani-Gangaraj, M. Guagliano and a. M. Dao, "Cold Spray Coating: Review of Material Systems and Future Perspectives," *Surface Engineering,* vol. 30, no. 6, pp. 369-395, 2014.

[5] S. Yin, C. Chen, X. Suo and R. Lupoi, "Cold-Sprayed Metal Coatings with Nanostructure," *Advances in Materials Science and Engineering,* vol. 2018, p. 19, 2018.

[6] J. Kharthikeyan, "The advantages and disadvantages of the cold spray process coating," in *The Cold Spray Materials Deposition Process*, Woodhead Publishing, 2007, pp. 62-71.

[7] M. F. Smith, "3 – Comparing cold spray with thermal spray coating technologies," in *The Cold Spray Materials Deposition Process*, 2007, pp. 43-61.

[8] M. Grujicic, C. Zhao, W. DeRosset and D. Helfritch, "Adiabatic shear instability based mechanism for particles/substrate bonding in the cold-gas dynamic-spray process," *Materials and Design,* vol. 25, pp. 681-688, 2005.

[9] M. Hassani-Gangaraj, D. Veysset, K. A. Nelson and C. A. Schuh, "In-situ observations of single micro-particle impact bonding," *Scripta Materialia,* vol. 145, pp. 9-13, 2018.

[10] H. Assadi, T. Schmidt, H. Richter, J.-O. Kliemann, K. Binder, F. Gartner, T. Klassen and H. Kreye, "On Parameter Selection in Cold Spray," *Journal of Thermal Spray Technology,* vol. 20, pp. 1161-1171, 2011.

[11] T. Schmidt, F. Gartner, H. Assadi and a. H. Kreye, "Development of a Generalized Parameter Window for Cold Spray Deposition," *Acta Materialia,* vol. 54, no. 3, pp. 729-742, 2006.

[12] M. Hassani-Gangaraj, D. Veysset, K. Nelson and a. C. Schuh, "Impact-Bonding with Aluminum, Silver, and Gold Microparticles: Toward Understanding the Role of Native Oxide," *Applied Surface Science,* vol. 476, pp. 528-532, 2019.

[13] C.-J. Li, H.-T. Wang, Q. Zhang, G.-J. Yang, W.-Y. Li and a. H. Liao, "Influence of Spray Materials and Their Surface Oxidation on the Critical Velocity in Cold Spraying," *Journal of Thermal Spray Technology,* vol. 19, no. 1, pp. 95-101, 2010.

[14] C.-J. Li and W.-Y. Li, "Deposition Characteristics of Titanium Coating in Cold Spraying," *Surface Coatings Technology,* vol. 167, no. 2, pp. 278-283, 2003.

[15] M. Hirmand and H. Jahed, "A numerical modelling framework for predictive simulations of impact-induced bonding in cold spray additive manufacturing," *Pending publication,* 2021.

[16] M. Hassani-Gangaraj, D. Veysset, V. K. Champagne, K. A. Nelson and C. A. Schuh, "Adiabatic shear instability is not necessary for adhesion in cold spray," *Acta Materialia,* vol. 158, pp. 430-439, 2018.

[17] M. Yu, W.-Y. Li, F. Wang and H. Liao, "Finite Element Simulation of Impacting Behavior of Particles in Cold Spraying by Eulerian Approach," *Journal of Thermal Spray Technology,* vol. 21, no. 3-4, pp. 745-752, 2011.

[18] R. Ghelichi, D. MacDonald, S. Bagherifard, H. Jahed, M. Guagliano and B. Jodoin, "Microstructure and fatigue behavior of cold spray coated Al5052," *Acta Materialia,* vol. 60, pp. 6555-6561, 2012.

[19] S. Dayani, S. Shaha, R. Ghelichi, J. Wang and H. Jahed, "The impact of AA7075 cold spray coating on the fatigue life of AZ31B cast alloy," *Surface & Coatings Technology,* vol. 337, pp. 150-158, 2018.

[20] R. Ghelichi, S. Bagherifard, D. MacDonald, M. Brochu, H. Jahed, B. Jodoin and M. Guagliano, "Fatigue strength of Al alloy cold sprayed with nanocrystalline powders," *International Journal of Fatigue,* vol. 65, pp. 51-57, 2014.

[21] B. Marzbanrad, H. Jahed and E. Toyserkani, "On the evolution of substrate's residual stress during cold spray process: A parameteric study," *Materials and Design,* vol. 138, pp. 90-102, 2018.

[22] B. Marzbanrad, E. Toyserkani and H. Jahed, "Customization of residual stress induced in cold spray printing," *Journal of Materials Processing Tech.,* vol. 289, p. 116928, 2021.

[23] M. Diab, X. Pang and H. Jahed, "The effect of pure aluminum cold spray coating on corrosion and corrosion fatigue of magnesium (3% Al-1% Zn) extrusion," *Surface & Coatings Technology,* vol. 309, pp. 423-435, 2017.

[24] W. Hou, Z. Shen, M. O. N. Huda, Y. Shen, H. Jahed and A. Gerlich, "Enhancing metallurgical and mechanical properties of friction stir butt welded joints of Al–Cu via cold sprayed Ni interlayer," *Materials Science & Engineering,* vol. 809, p. 140992, 2021.

[25] F. Khodabakhshi, B. Marzbanrad, L. Shah, H. Jahed and A. Gerlich, "Friction-stir processing of a cold sprayed AA7075 coating layer on the AZ31B substrate: Structural homogeneity, microstructures and hardness," *Surface & Coatings Technology,* vol. 331, pp. 116-128, 2017.

[26] S. Shaha and H. Jahed, "An in-situ study of the interface microstructure of solid-state additive deposition of AA7075 on AZ31B substrate," *Applied Surface Science,* vol. 508, p. 144974, 2020.

[27] J. Tang, G. Saha, P. Richter, J. Kondas, A. Colella and P. Matteazzi, "Effects of Post-spray Heat Treatment on Hardness and Wear Properties of Ti-WC High-Pressure Cold Spray Coatings," *Journal of Thermal Spray Technology,* vol. 27, pp. 1153-1164, 2018.

[28] H. Assadi, F. Gartner, T. Stoltenhoff and H. Kreye, "Bonding mechanism in cold gas spraying," *Acta Materialia,* vol. 51, pp. 4379-4394, 2003.

[29] T. Belytschko, W. K. Liu, B. Moran and K. I. Elkhodary, Nonlinear Finite Elements for Continua and Structures, West Sussex: John Wiley & Sons, Ltd, 2014.

[30] J. Xie, K. Ogawa, D. Nelias and Y. Ichikawa, "Simulation of the Cold Spray Particle Deposition Process," *Journal of Tribology,* vol. 137, no. 4, 2015.

[31] D. Benson, "A multi-material Eulerian formulation for the efficient solution of impact and penetration problems," *Computational Mechanics,* vol. 15, pp. 558-571, 1995.

[32] X. Zhang, Z. Chen and L. Yan, The Material Point Method: A Continuum-Based Particle Method for Extreme Loading Cases, Orlando: Academic Press Inc., 2017.

[33] W. Li, C. Zhang, C.-J. Li and H. Liao, "Modeling aspects of high velocity impact of particles in cold spraying by explicit finite element analysis," *Journal of Thermal Spray Technology,* vol. 18, no. 5-6, pp. 921-933, 2009.

[34] A. Manap, O. Nooririnah, H. Misran, T. Okabe and K. Ogawa, "Experimental and SPH study of cold spray impact between similar and dissimilar metals," *Surface Engineering,* vol. 30, no. 5, pp. 335-341, 2014.

[35] P. Profizi, A. Combescure and a. K. Ogawa, "Numerical analysis of single particle impact in the context of Cold Spray: a new adhesion model," in *IOP Conference Series: Earth and Environmental Science 32 012062*, 2016.

[36] R. Gingold and J. Monaghan, "Smoothed particle hydrodynamics: theory and application to non-spherical stars," *Monthly Notices of the Royal Astronomical Society,* vol. 181, no. 3, pp. 375-389, 1977.

[37] S. J. Raymond, B. Jones and J. R. Williams, "A strategy to couple the Material Point Method (MPM) and Smoothed Particle Hydrodynamics (SPH) computational techniques," *Computational Particle Mechanics,* vol. 5, no. 1, pp. 49-58, 2016.

[38] K. A. Fraser, L. I. Kiss, S.-G. Lyne and D. Drolet, "Optimization of Friction Stir Weld Joint Quality Using a Meshfree Fully-Coupled Thermo-Mechanics Approach," *Open Access Metallurgy Journal,* vol. 8, no. 2, pp. 101-125, 2018.

[39] W.-Y. Li, S. Yin and X.-F. Wang, "Numerical investigations of the effect of oblique impact on particle deformation in cold spraying by SPH method," *Applied Surface Science,* vol. 256, pp. 3725-3734, 2010.

[40] S. Yin, X.-F. Wang, B.-P. Xu and W.-Y. Li, "Examination on the Calculation Method for Modeling the Multi-Particle Impact Process in Cold Spraying," *Journal of Thermal Spray Technology,* vol. 19, pp. 1032-1041, 2010.

[41] D.-M. Chun and S.-H. Ahn, "Deposition mechanism of dry sprayed ceramic particles at room temperature using a nano-particle deposition system," *Acta Materialia,* vol. 59, pp. 2693-2703, 2011.

[42] A. Hemeda, C. Zhang, X. Hu, D. Fukuda, D. Cote, I. Nault, A. Nardi, V. Champagne, Y. Ma and J. Palko, "Particle-based simulation of cold spray: Influence of oxide layer on impact process," *Additive Manufacturing,* vol. 101517, 2020.

[43] S. Guetta, M. Berger, F. Borit, V. Guipont, M. Jeandin, M. Boustie, Y. Ichikawa, K. Sakaguchi and K. Ogawa, "Influence of particle velocity on adhesion of cold-sprayed splats," *Journal of Thermal Spray Technology,* vol. 18, no. 3, pp. 331-342, 2009.

[44] G. Bae, Y. Xiong, S. Kumar, K. Kang and C. Lee, "General aspects of interface bonding," *Acta Materialia,* vol. 56, pp. 4858-4868, 2008.

[45] S. Rahmati and A. Ghaei, "The use of particle/substrate material models in simulation of cold-gas dynamic-spray process," *Journal of Thermal Spray Technology,* vol. 23, pp. 530-540, 2014.

[46] G. Johnson and W. Cook, "Fracture Characteristics of Three Metals Subjected to Various Strains, Strain rates, Temperatures and Pressures," *Engineering Fracture Mechanics,* vol. 21, no. 1, pp. 31-48, 1985.

[47] B. Banerjee, "An evaluation of plastic flow stress models for the simulation of high-temperature and high-strain-rate deformation of metals," Department of Mechanical Engineering, University of Utah, Salt Lake City, 2019.

[48] D. Preston, D. Tonks and a. D. Wallace, "Model of Plastic Deformation for Extreme Loading Conditions," *Journal of Applied Physics,* vol. 93, no. 1, pp. 211-220, 2002.

[49] S. Rahmati and B. Jodoin, "Physically Based Finite Element Modeling Method to Predict Metallic Bonding in Cold Spray," *Journal of Thermal Spray Technology,* vol. 29, pp. 611-619, 2020.

[50] M. Razavipour and B. Jodoin, "Material Model for Predicting Dynamic Response of Copper and Nickel at Very High Strain Rates Under Cold Spray Conditions," *Journal of Thermal Spray Technology,* vol. 30, pp. 324-343, 2021.

[51] M. Meyers, Dynamic Behavior of Materials, New York: John WIley & Sons, 1994.

[52] D. J. Steinberg, S. Cochran and M. Guinan, "A constitutive model for metals applicable at high-strain rate," *Journal of Applied Physics,* vol. 51, no. 3, pp. 1498-1504, 1980.

[53] G. Li, X. Wang and W. Li, "Effect of different incidence angles on bonding performance in cold spraying," *Transactions of Nonferrous Metals Society of China,* vol. 17, pp. 116-121, 2007.

[54] X. Wang, F. Feng, M. Klecka, M. Mordasky, J. Garofano, T. El-Wardany, A. Nardi and V. Champagne, "Characterization and modeling of the bonding process in cold spray additive manufacturing," *Additive Manufacturing,* vol. 8, pp. 149-162, 2015.

[55] Y. Y. Lin, C. Y. Hui and A. Jagota, "The role of viscoelastic adhesive contacts in the sintering of polymeric particles," *Journal of Colloid and Interface Science,* vol. 237, pp. 267-282, 2001.

[56] A. Manap, T. Okabe and K. Ogawa, "Computer simulation of cold sprayed deposition using smoothed particle hydrodynamics," *Procedia Engineering,* vol. 10, pp. 1145-1150, 2011.

[57] A. Manap and K. Ogawa, "Numerical analysis of interfacial bonding of aluminum powder particle and aluminum substrate by cold spray technique using the SPH method," in *Proc. JSME/ASME 2011 Int. Conf. on 'Materials and processing'*, Corvallis, OR, USA, 2011.

[58] A. Manap, K. Ogawa and T. Okabe, "Numerical analysis of interfacial bonding of Al–Si particle and mild steel substrate by cold spray technique using the SPH method," *Journal of Solid Mechanics and Materials Engineering,* vol. 6, pp. 241-250, 2012.

[59] K. Raoufi and J. Weiss, "The role of fiber reinforcement in mitigating shrinkage cracks in concrete," in *Fibrous and Composite Materials for Civil Engineering Applications*, Woodhead Publishing Series in Textiles, 2011, pp. 168-188.

[60] Y. Sun, D. Veysset, K. A. Nelson and C. A. Schuh, "The transition from rebound to bonding in high-velocity metallic microparticle impacts: jetting-associated power-law divergence," *Journal of Applied Mechanics,* vol. 87, no. 9, p. 091002, 2020.

[61] L. Vergani, M. Guagliano, A. Manap, T. Okabe and K. Ogawa, "Computer simulation of cold sprayed deposition using smoothed particle hydrodynamics," *Procedia Engineering,* vol. 10, pp. 1145-1150, 2011.

[62] B. Yildirim, H. Fukanuma, T. Ando, A. Gouldstone and S. Müftü, "Numerical Investigation Into Cold Spray Bonding Processes," *Journal of Tribology,* vol. 137, p. 011102, 2014.

[63] Y. V. Kurochkin, Y. N. Demin and S. I. Soldatenkov, "Demonstration of the Method of Cold Gas Dynamic Spraying of Coatings," *Chemical and Petroleum Engineering,* vol. 38, no. 3, pp. 245-248, 2002.

[64] J. Wu, H. Fang, S. Yoon, H. Kim and C. Lee, "The rebound phenomenon in kinetic spraying deposition," *Scripta Materialia,* vol. 54, pp. 665-669, 2006.

[65] M. K. Shorshorov and Y. A. Kharlamov, Physical and chemical principles of detonation gas spray coating, Moscow, Russia: Nauka Publishing, 1978.

[66] S. Bardenhagen and E. Kober, "The generalized interpolation material point method," *Computer Modeling in Engineering & Sciences,* vol. 5, no. 6, pp. 477-495, 2004.

[67] S. G. Bardenhagen, "Energy conservation error in the material point method for solid mechanics," *Journal of Computational Physics,* vol. 180, pp. 383-403, 2002.

[68] J. A. Nairn, C. C. Hammerquist and G. Smith, "New material point method contact algorithms for improved accuracy, large-deformation problems, and proper null-space filtering," *Computer Methods in Applied Mechancis and Engineering,* vol. 362, p. 122859, 2020.

[69] S. Sinaie, T. D. Ngo, V. P. Nguyen and T. Rabczuk, "Validation of the material point method for the simulation of thin-walled tubes under lateral compression," *Thin-Walled Structures,* vol. 130, no. 32, pp. 32-46, 2018.

[70] Z. Ma, X. Zhang and P. Huang, "An object-oriented MPM framework for simulation of large deformation and contact of numerous grains," *Computer Modeling in Engineering & Sciences,* vol. 55, no. 1, pp. 61-87, 2010.

[71] Y. Cormier, P. Dupuis, B. Jodoin and A. Ghaei, "Finite Element Analysis and Failure Mode Characterization of Pyramidal Fin Arrays Produced by Masked Cold Gas Dynamic Spray," *Journal of Thermal Spray Technology,* vol. 24, pp. 1549-1565, 2015.

[72] A. Nastic and B. Jodoin, "Evaluation of Heat Transfer Transport Coefficient for Cold Spray Through Computational Fluid Dynamics and Particle In-Flight Temperature Measurement Using a High-Speed IR Camera," *Journal of Thermal Spray Technology,* vol. 27, pp. 1491-1517, 2018.

[73] G. Ravichandran, A. J. Rosakis, J. Hodowany and P. Rosakis, "On the conversion of plastic work into heat during high-strain-rate deformation," in *12th APS Topical Conference on Shock Compression of Condensed Matter. American Physical Society*, 2001.

[74] J. Nairn, "Modeling Imperfect Interfaces in the Material Point Method using Multimaterial Methods," *Computed Modeling in Engineering & Sciences,* vol. 92, pp. 271-299, 2013.

[75] J. Nairn, "Surface Normals," Oregon State University, 26 September 2013. [Online]. Available: http://osupdocs.forestry.oregonstate.edu/index.php/Surface_Normals. [Accessed 23 March 2021].

[76] V. Lemiale, A. Hurmane and J. A. Nairn, "Material point method simulation of equal channel angular pressing involving large plastic strain and contact," *Computer Modeling in Engineering and Science,* vol. 70, no. 1, pp. 41-66, 2010.

[77] M. Ross, "Modeling Methods for Silent Boundaries in Infinite Media," Aerospace Engineering Sciences - University of Colorado, Boulder, 2004.

[78] J. Lysmer and R. L. Kuhlemeyer, "Finite Dynamic Model for Infinite Media," *Journal of the Engineering Mechanics Division,* vol. 95, no. 4, pp. 859-878, 1969.

[79] J. Peng, K. Lee and G. Ingersoll, "An Introduction to Logistic Regression Analysis and Reporting," *The Journal of Educational Research,* vol. 96, no. 1, pp. 3-14, 2002.

[80] A. Pant, "Towards Data Science," 22 Jan 2019. [Online]. Available: https://towardsdatascience.com/introduction-to-logistic-regression-66248243c148. [Accessed 6 Jan 2021].

[81] *MATLAB Optimization Toolbox,* Natick, Massachusetts, United States: The MathWorks, Inc., 2020.

[82] P. King, S. Zahiri and M. Jahedi, "Microstructural Refinement within a Cold-Sprayed Copper Particle," *Metallurgical and Materials Transactions,* vol. 40, no. 9, pp. 2115-2123, 2009.

[83] K. Kim, M. Watanabe, K. Mitsuishi, K. Iakoubovskii and S. Kuroda, "Impact Bonding and Rebounding between Kinetically Sprayed Titanium Particle and Steel Substrate Revealed by High-Resolution Electron Microscopy," *Journal of Physics D: Applied Physics,* vol. 42, no. 6, p. 65304, 2009.

[84] M. Vidaller, A. List, F. Gaertner, T. Klassen, S. Dosta and J. Guilemany, "Single Impact Bonding of Cold Sprayed Ti6Al-4V Powders on Different Substrates," *Journal of Thermal Spray Technology,* vol. 24, no. 4, pp. 644-658, 2015.

[85] W. Li, C. Zhang, H. Wang, X. Guo, H. Liao and C. Li, "Significant influences of metal reactivity and oxide films at particle surfaces on coating microstructure in cold spraying," *Applied Surface Science,* vol. 253, pp. 3557-3562, 2007.

[86] S. Yin, X. Wang, W. Li, H. Liao and H. Jie, "Deformation behavior of the oxide film on the surface of cold sprayed powder particle," *Applied Surface Science,* vol. 259, pp. 294-300, 2012.

[87] S. Krscanski and J. Brnic, "Prediction of Fatigue Crack Growth in Metallic Specimens under Constant Amplitude Loading Using Virtual Crack Closure and Forman Model," *Metals,* vol. 10, no. 7, p. 977, 2020.

[88] W. A. M. Brekelmans and J. H. P. d. Vree, "Reduction of mesh sensitivity in continuum damage mechanics," *Acta Mechanica,* vol. 110, pp. 49-56, 1995.

[89] V. P. Panoskaltsis and S. Bahuguna, "Finite element analysis of rate dependence and failure of concrete," in *European Conference on Computational Mechanics*, Munich, 1999.

[90] T. Schmidt, H. Assadi, F. Gartner, H. Richter and T. Stoltenhoff, "From Particle Acceleration to Impact and Bonding in Cold Spraying," *Journal of Thermal Spray Technology,* vol. 18, no. 5-6, pp. 794-808, 2009.

[91] X.-L. Zhou, X.-K. Wu, G. H.-H., J.-G. Wang and J.-S. Zhang, "Deposition behavior of multi-particle impact in cold spraying process," *Internation Journal of Minerals, Metallurgy and Materials,* vol. 17, no. 5, pp. 635-640, 2010.

[92] P. King, C. Busch, T. Kittel-Sherri, M. Jahedi and S. Gulizia, "Interface Melding in Cold Spray Titanium Particle Impact," *Surface Coatings Technology,* vol. 239, pp. 191-199, 2014.

[93] D. Goldbaum, R. R. Chromik, S. Yue, E. Irissou and J. G. Legoux, "Mechanical Property Mapping of Cold Sprayed Ti Splats and Coatings," *Journal of Thermal Spray Technology,* vol. 20, no. 3, pp. 486-496, 2011.

Appendix A – Stress Update

Using the strain and vorticity increments, it is possible to update the stress tensor of each material point at time step *n* based on the Jaumann rate of Cauchy stress. The stress tensor at the next time step can be calculated using the rotated stress ($\boldsymbol{\sigma}^{R^n}$) and Jaumann rate ($\boldsymbol{\sigma}^{\nabla n+1/2}$) tensors.

$$\boldsymbol{\sigma}^{n+1} = \boldsymbol{\sigma}^{R^n} + \boldsymbol{\sigma}^{\nabla n+1/2}\Delta t^{n+1/2} \qquad (A1.1)$$

For an isotropic elastic model, the Jaumann rate can be decomposed into its deviatoric and hydrostatic components, however the deviatoric component is most important in J_2 flow theory as it is used to calculate the effective stress. The Jaumann rate of the deviatoric stress tensor is given by

$$s^{\nabla} = 2G\dot{\boldsymbol{\varepsilon}}' \qquad (A1.2)$$

where G is the shear modulus and $\dot{\boldsymbol{\varepsilon}}'$ is the rate of deviatoric strain. Combining the above equations yields the equation for the trial elastic state in a radial return algorithm:

$$\begin{aligned}\boldsymbol{s}^{*(n+1)} &= \boldsymbol{s}^{R^n} + 2G\dot{\boldsymbol{\varepsilon}}'^{n+1}\Delta t^{n+1} \\ &= \boldsymbol{s}^{R^n} + 2G\Delta\boldsymbol{\varepsilon}'^{n+1} \qquad (A1.3)\end{aligned}$$

With this basic equation (A1.3) for the deviatoric stress at a trial elastic state, the following steps can be taken:

1. Calculate the rotated stresses at time step *n* based on the vorticity tensor.

$$\boldsymbol{\sigma}^{R^n} = \boldsymbol{\sigma}^n + \left[\boldsymbol{\sigma}^n \cdot \left(\boldsymbol{\Omega}^{n+1/2}\right)^T + \boldsymbol{\Omega}^{n+1/2} \cdot \boldsymbol{\sigma}^n\right]\Delta t^{n+1/2} \qquad (A2)$$

2. Separate the rotated stress tensor into hydrostatic and deviatoric components.

$$\sigma_h^n = \frac{\sigma_{11}^{R^n} + \sigma_{22}^{R^n} + \sigma_{33}^{R^n}}{3} \qquad (A3.1)$$

$$\boldsymbol{s}^{R^n} = \boldsymbol{\sigma}^{R^n} - \sigma_h^n\boldsymbol{I} \qquad (A3.2)$$

   where $\boldsymbol{I}$ is the 3x3 identity matrix.

3. Calculate the elastic trial deviatoric stress state $\boldsymbol{s}^{*(n+1)}$ using (A1.3). Note that the deviatoric strain increment is calculated from the total strain increment by

$$\Delta\boldsymbol{\varepsilon}'^{n+1} = \Delta\boldsymbol{\varepsilon}^{n+1} - \Delta\varepsilon_{kk}\boldsymbol{I} \qquad (A4.1)$$

   where

$$\Delta\varepsilon_{kk} = \frac{1}{3}(\Delta\varepsilon_{11} + \Delta\varepsilon_{22} + \Delta\varepsilon_{33}) \qquad (A4.2)$$

4. Calculate the trial von Mises stress using $\boldsymbol{s}^{*(n+1)}$ as per J_2 flow theory.

$$\bar{\sigma}^{*(n+1)} = \left[\frac{3}{2}\boldsymbol{s}_{ij}^{*(n+1)}\boldsymbol{s}_{ij}^{*(n+1)}\right]^{1/2} \qquad (A5)$$

5. If $\bar{\sigma}^{*(n+1)} < \sigma_y^n$ then the trial stress is the true stress state, $\Delta\bar{\varepsilon}^p = 0$ and skip to step 8. Otherwise, continue on to step 6.
6. If $\bar{\sigma}^{*(n+1)} > \sigma_y^n$, a radial return algorithm based on J_2 flow theory is used to determine the effective plastic strain increment ($\Delta\bar{\varepsilon}^p$) assuming linear isotropic hardening.

   $$\Delta\bar{\varepsilon}^{p(n+1)} = \frac{\bar{\sigma}^{*(n+1)} - \sigma_y^n}{3G + E^p} \tag{A6}$$

   where $E^p = \frac{d\sigma_y}{d\varepsilon^p}$ and the equation for σ_y differs based on what material model is used.

   For the PTW model, $E^p = \frac{2\mu\theta \exp\left(-\beta - \frac{\theta\varepsilon^p}{\alpha\psi}\right)}{1 - \psi\,\mathrm{ex}\ \left(-\beta - \frac{\theta\varepsilon^p}{\alpha\psi}\right)}$.

   The updated total and increment in plastic strain is then used to update the flow stress of the material based on the strength model. In simple linear isotropic hardening, $\sigma_y^{n+1} = \sigma_y^n + E^p\Delta\bar{\varepsilon}^{p(n+1)}$, however for the PTW model, flow stress is updated using the updated total and increment effective plastic strains by the following:

   $$\sigma_y^{n+1} = 2\mu\left(\tau_s + \alpha \ln\left(1 - \psi \exp\left(-\beta - \frac{\theta\varepsilon^p}{\alpha\psi}\right)\right)\right) \tag{A7}$$

   Definitions of PTW model parameters can be found in Chapter 2.4.2.

7. The corrected stress state can be found by multiplying the trial stress state by a scaling factor similar to in simple linear isotropic hardening and is given by

   $$scaling\ factor = m = \frac{\sigma_y^{n+1}}{\bar{\sigma}^{*(n+1)}} \tag{A8.1}$$

   $$\boldsymbol{s}^{n+1} = m\boldsymbol{s}^{*(n+1)} \tag{A8.2}$$

   $$\bar{\sigma}^{n+1} = m\bar{\sigma}^{*(n+1)} \tag{A8.3}$$

8. The Mie-Grüneisen equation of state is then finally used to update pressure and in effect the hydrostatic stresses. A more detailed description of this process can be found in Section 3.5.2 but the following provides a brief description:
   a. First, a trial internal energy and specific energy are calculated.

      $$e^{*n+1} = e^n + V^{n+1/2}\boldsymbol{\sigma}_d^{n+1/2} : \Delta\boldsymbol{\varepsilon}^{n+1/2} - \frac{1}{2}\Delta V p^n \tag{A9.1}$$

      $$E^{*n+1} = \frac{e^{*n+1}}{V_0} \tag{A9.2}$$

   b. Using these trial values, the pressure and hydrostatic stress at the next time step can be calculated as follows:

      $$p^{n+1} = \frac{A^{n+1} + B^{n+1}E^{*n+1}}{1 + \frac{1}{2}B^{n+1}\left(\frac{\Delta V}{V_0}\right)} = -\sigma_h^{n+1} \tag{A10}$$

c. Finally, the actual internal energy can be updated from the trial value for use in the next time step with:

$$e^{n+1} = e^{*n+1} - \frac{1}{2}\Delta V p^{n+1} \tag{A11}$$

9. Hydrostatic and deviatoric components of stress have now been found for the following $(n+1)th$ time step, meaning the full stress tensor has now been successfully updated.

Appendix B – Bonding Boundaries with All Grid Configurations

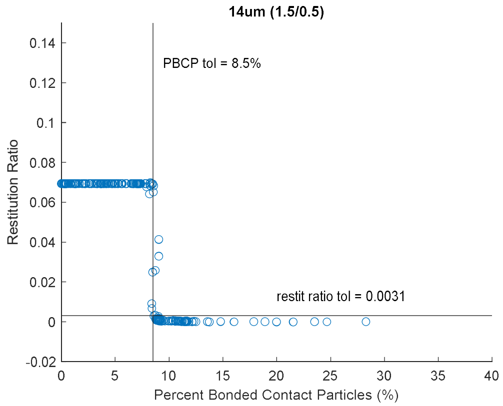

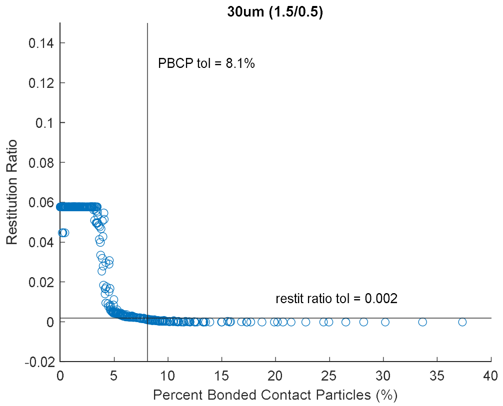

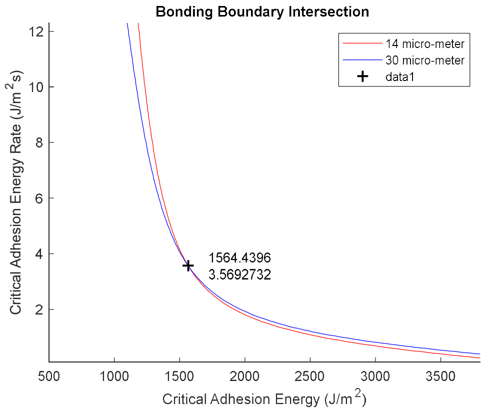

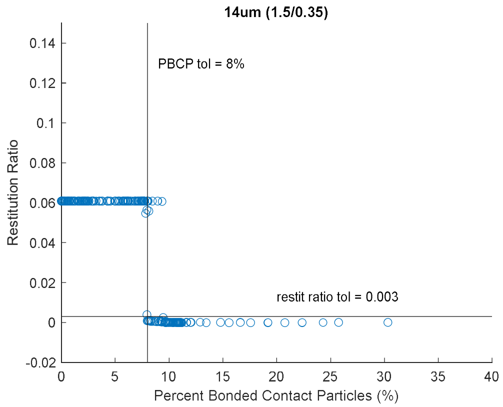

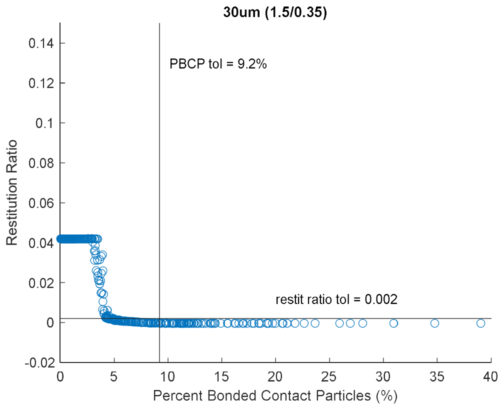

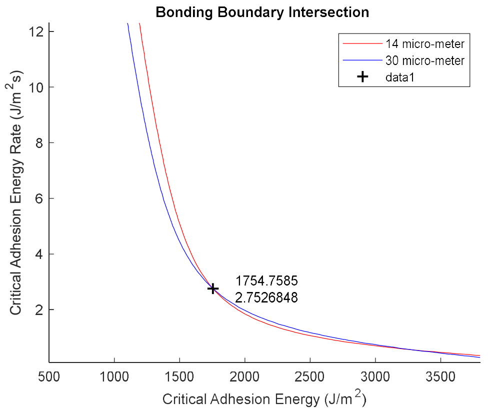

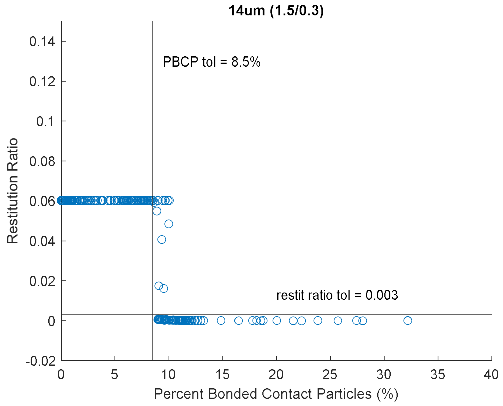

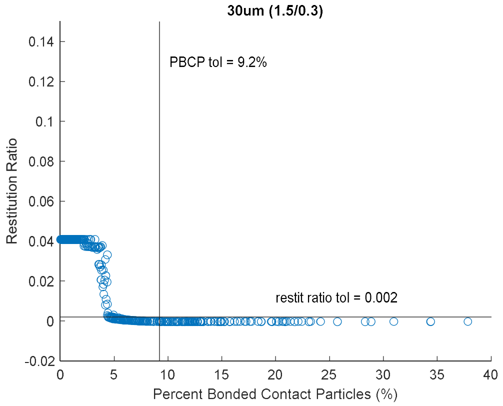

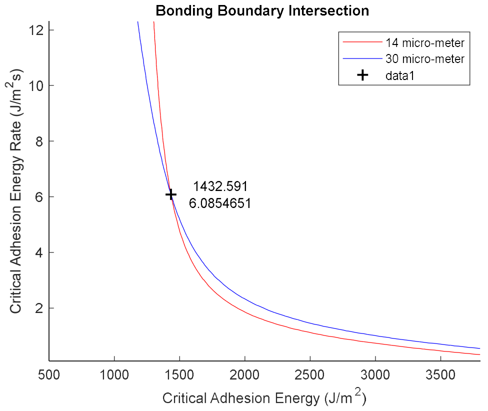

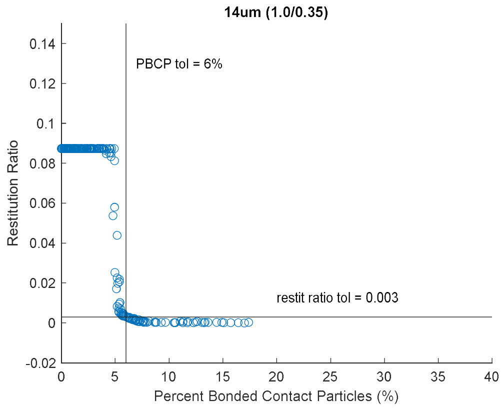
14um (1.0/0.35)
PBCP tol = 6%
restit ratio tol = 0.003
Restitution Ratio
Percent Bonded Contact Particles (%)
0.14
0.12
0.1
0.08
0.06
0.04
0.02
0
-0.02
0
5
10
15
20
25
30
35
40

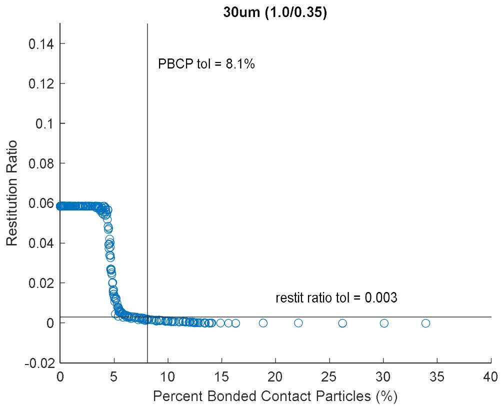
30um (1.0/0.35)
PBCP tol = 8.1%
restit ratio tol = 0.003
Restitution Ratio
Percent Bonded Contact Particles (%)
0.14
0.12
0.1
0.08
0.06
0.04
0.02
0
-0.02
0
5
10
15
20
25
30
35
40

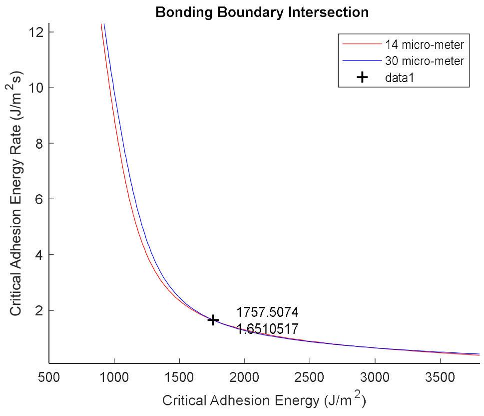
Bonding Boundary Intersection
14 micro-meter
30 micro-meter
data1
1757.5074
1.6510517
Critical Adhesion Energy Rate (J/m^{2}s)
Critical Adhesion Energy (J/m^2)
12
10
8
6
4
2
500
1000
1500
2000
2500
3000
3500

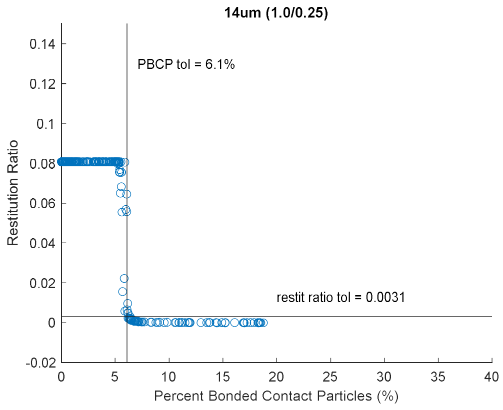
14um (1.0/0.25)
PBCP tol = 6.1%
restit ratio tol = 0.0031
Restitution Ratio
Percent Bonded Contact Particles (%)
0.14
0.12
0.1
0.08
0.06
0.04
0.02
0
-0.02
0
5
10
15
20
25
30
35
40

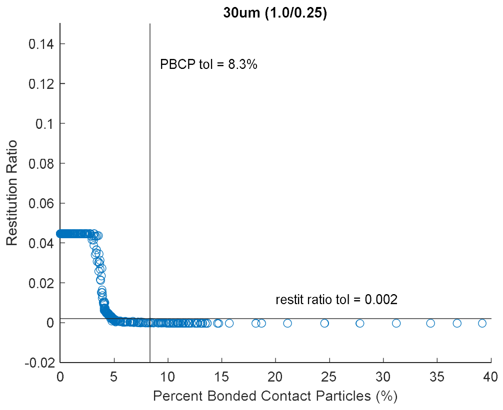
30um (1.0/0.25)
PBCP tol = 8.3%
restit ratio tol = 0.002
Restitution Ratio
Percent Bonded Contact Particles (%)
0.14
0.12
0.1
0.08
0.06
0.04
0.02
0
-0.02
0
5
10
15
20
25
30
35
40

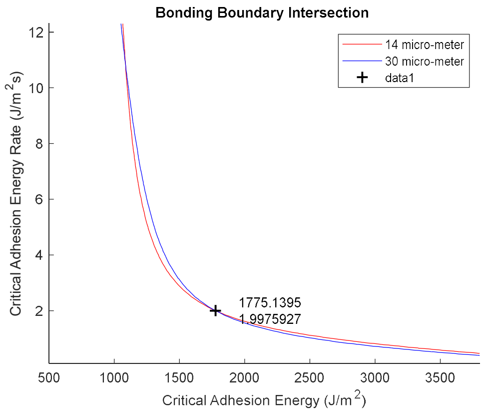
Bonding Boundary Intersection
14 micro-meter
30 micro-meter
data1
1775.1395
1.9975927
Critical Adhesion Energy Rate (J/m^{2}s)
Critical Adhesion Energy (J/m^2)
12
10
8
6
4
2
500
1000
1500
2000
2500
3000
3500

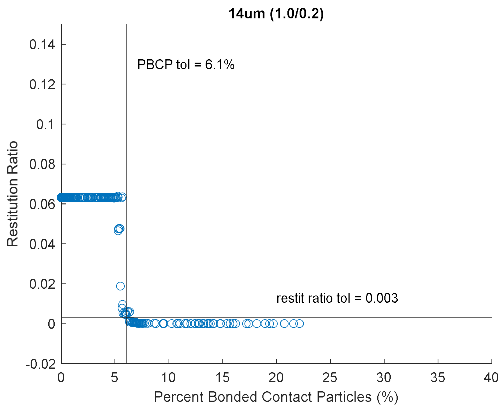
14um (1.0/0.2)
PBCP tol = 6.1%
restit ratio tol = 0.003
Restitution Ratio
Percent Bonded Contact Particles (%)
0.14
0.12
0.1
0.08
0.06
0.04
0.02
0
-0.02
0
5
10
15
20
25
30
35
40

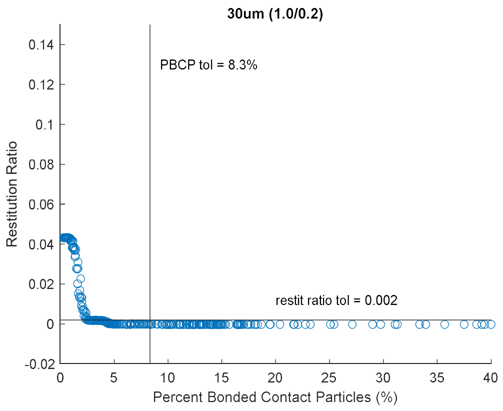
30um (1.0/0.2)
PBCP tol = 8.3%
restit ratio tol = 0.002
Restitution Ratio
Percent Bonded Contact Particles (%)
0.14
0.12
0.1
0.08
0.06
0.04
0.02
0
-0.02
0
5
10
15
20
25
30
35
40

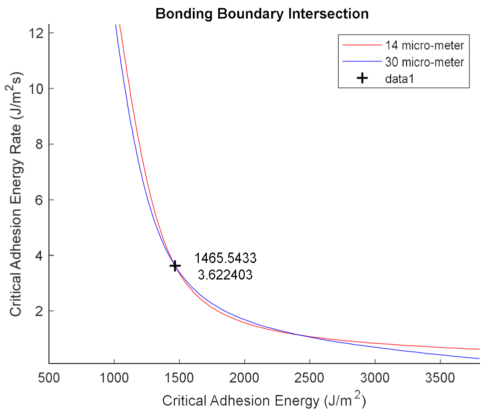
Bonding Boundary Intersection
14 micro-meter
30 micro-meter
data1
1465.5433
3.622403
Critical Adhesion Energy Rate (J/m^{2}s)
Critical Adhesion Energy (J/m^2)
12
10
8
6
4
2
500
1000
1500
2000
2500
3000
3500

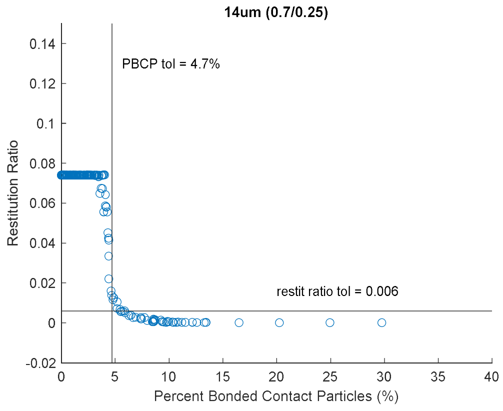
14um (0.7/0.25)
PBCP tol = 4.7%
restit ratio tol = 0.006
Restitution Ratio
Percent Bonded Contact Particles (%)
0.14
0.12
0.1
0.08
0.06
0.04
0.02
0
-0.02
0
5
10
15
20
25
30
35
40

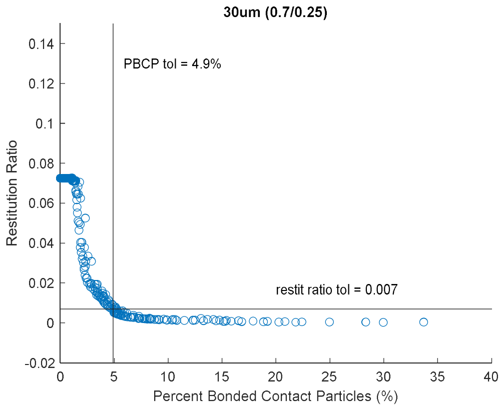
30um (0.7/0.25)
PBCP tol = 4.9%
restit ratio tol = 0.007
Restitution Ratio
Percent Bonded Contact Particles (%)
0.14
0.12
0.1
0.08
0.06
0.04
0.02
0
-0.02
0
5
10
15
20
25
30
35
40

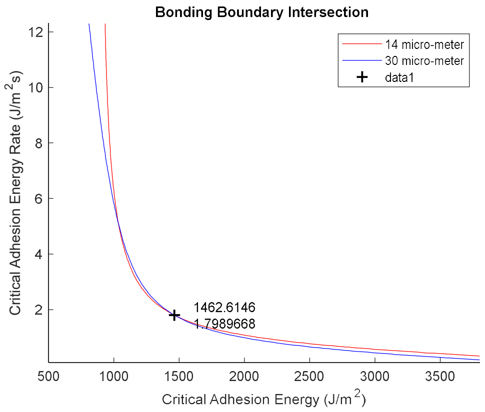
Bonding Boundary Intersection
14 micro-meter
30 micro-meter
data1
1462.6146
1.7989668
Critical Adhesion Energy Rate (J/m^{2}s)
Critical Adhesion Energy (J/m^2)
12
10
8
6
4
2
500
1000
1500
2000
2500
3000
3500

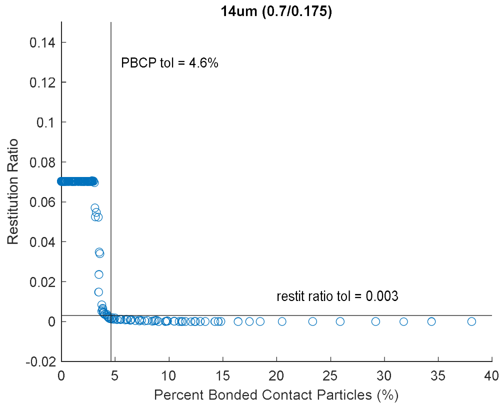
14um (0.7/0.175)
PBCP tol = 4.6%
restit ratio tol = 0.003
Restitution Ratio
Percent Bonded Contact Particles (%)
0.14
0.12
0.1
0.08
0.06
0.04
0.02
0
-0.02
0
5
10
15
20
25
30
35
40

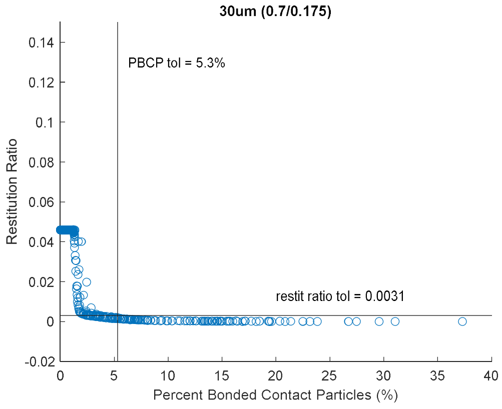
30um (0.7/0.175)
PBCP tol = 5.3%
restit ratio tol = 0.0031
Restitution Ratio
Percent Bonded Contact Particles (%)
0.14
0.12
0.1
0.08
0.06
0.04
0.02
0
-0.02
0
5
10
15
20
25
30
35
40

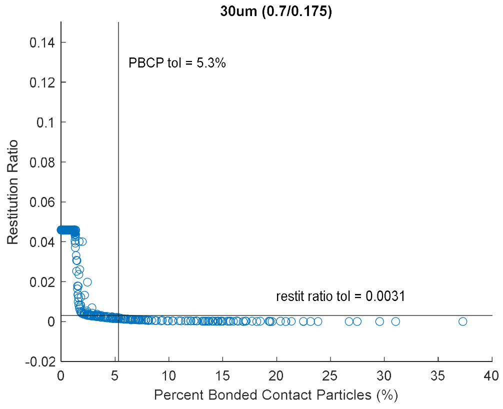
30um (0.7/0.175)
PBCP tol = 5.3%
restit ratio tol = 0.0031
Restitution Ratio
Percent Bonded Contact Particles (%)
0.14
0.12
0.1
0.08
0.06
0.04
0.02
0
-0.02
0
5
10
15
20
25
30
35
40

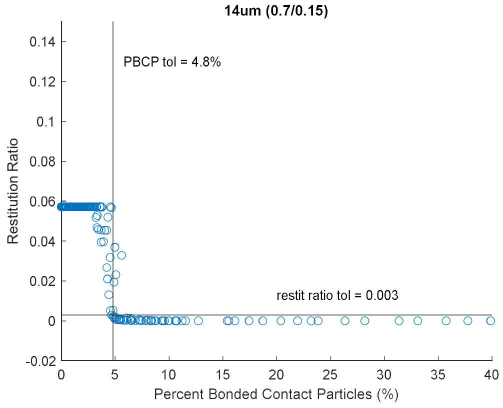
14um (0.7/0.15)
PBCP tol = 4.8%
restit ratio tol = 0.003
Restitution Ratio
Percent Bonded Contact Particles (%)
0.14
0.12
0.1
0.08
0.06
0.04
0.02
0
-0.02
0
5
10
15
20
25
30
35
40

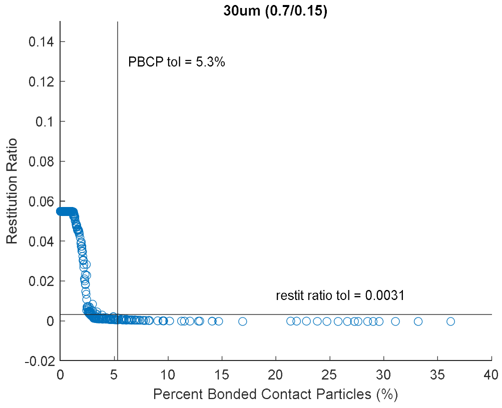
30um (0.7/0.15)
PBCP tol = 5.3%
restit ratio tol = 0.0031
Restitution Ratio
Percent Bonded Contact Particles (%)
0.14
0.12
0.1
0.08
0.06
0.04
0.02
0
-0.02
0
5
10
15
20
25
30
35
40

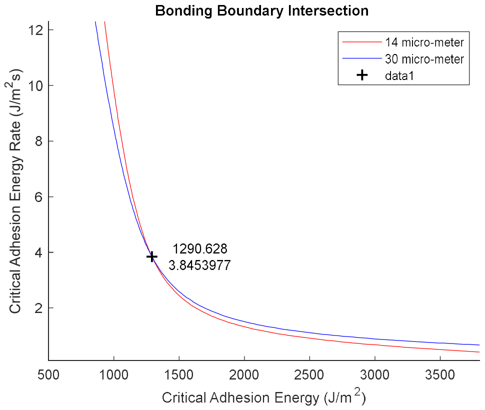
Bonding Boundary Intersection
14 micro-meter
30 micro-meter
data1
1290.628
3.8453977
Critical Adhesion Energy Rate (J/m^{2}s)
Critical Adhesion Energy (J/m^2)
12
10
8
6
4
2
500
1000
1500
2000
2500
3000
3500